DISSERTATION

DEVELOPMENT OF A HIGH ENERGY TI:SAPPHIRE LASER FOR THE EXCITATION OF EXTREME ULTRAVIOLET LASERS

Submitted by

Dale Herman Martz

Electrical and Computer Engineering Department

In partial fulfillment of the requirements

For the Degree of Doctor of Philosophy

Colorado State University

Fort Collins, Colorado

Spring 2011

Doctoral Committee:

Department Head: Anthony A. Maciejewski

Advisor: Jorge J. Rocca

Siu Au Lee
Mario C. Marconi
Carmen S. Menoni

ABSTRACT OF DISSERTAION

DEVELOPMENT OF A HIGH ENERGY TI:SAPPHIRE LASER FOR THE EXCITATION OF EXTREME ULTRAVIOLET LASERS

This dissertation describes the design, construction and characterization of a high energy chirped-pulse amplification Titanium-Sapphire laser system for the excitation of Extreme Ultraviolet (EUV) lasers. Compact EUV lasers have made possible nano-scale imaging, dense plasma diagnostics and photo-chemistry and photo-physics studies. They also have the potential to make possible a variety of new studies of surfaces and materials and enable the development of unique metrology and processing tools for industry. The components developed to realize high energy operation of the Titanium-Sapphire laser include the development of a Nd:Glass zig-zag slab pump laser and novel 800 nm multi-layer dielectric diffraction gratings for picosecond compression

The Titanium-Sapphire laser was used to pump several table-top EUV lasers. Increased average power operation of a 13.9 nm nickel-like silver laser generating 20 μW was demonstrated. This is the highest average power obtained from a compact EUV laser to date. Injection seeding of the 13.9 nm EUV amplifier produced laser beams with greatly improved beam characteristics which includes a large reduction in beam

divergence and a near Gaussian far-field profile. The laser was also used to pump a gain-saturated table-top laser at 10.9 nm in nickel-like tellurium.

ACKNOWLEDGEMENTS

I would like to thank Professor Jorge Rocca for the opportunity to work with him at Colorado State University's Engineering Research Center for Extreme Ultraviolet Science and Technology, and for all of his much appreciated support. I would also like to thank my committee members Professor Siu Au Lee, Professor Mario Marconi and Professor Carmen Menoni for their participation and reading of this dissertation. I would also acknowledge everyone who has helped me during my time at the lab – Brad Luther, Yong Wang, David Alessi, Brendan Reagan, Federico Furch, Mike Grisham, Fernando Brizuela, Mike Purvis, Mark Berrill, Jorge Filevich, Mark Woolston, Paul Platte, Jonathan Grava, Erik Krous, David Kemp, Scott Domingue, Scott Heinbuch and Dinesh Patel.

Furthermore, I would like to thank my family, friends and Matilda Wheaton for all of their love and support. Without any of these people this would not be possible.

This work was supported by the Engineering Research Centers Program of the National Science Foundation under Award EEC-0310717

Table of Contents

CHAPTER 3

CHAPTER 1

INTRODUCTION

1.1 Extreme Ultraviolet Light Sources

It has been widely recognized that the unique properties of extreme ultraviolet (EUV) radiation has the potential to make possible a variety of new studies of surfaces and materials, and enable the development of unique metrology and processing tools for industry which have not been possible before [1, 2]. This has been accomplished utilizing the relatively high photon energy (25 eV to several hundred eV) and short wavelength (50 nm to 2 nm) of this radiation (Figure 1.1).

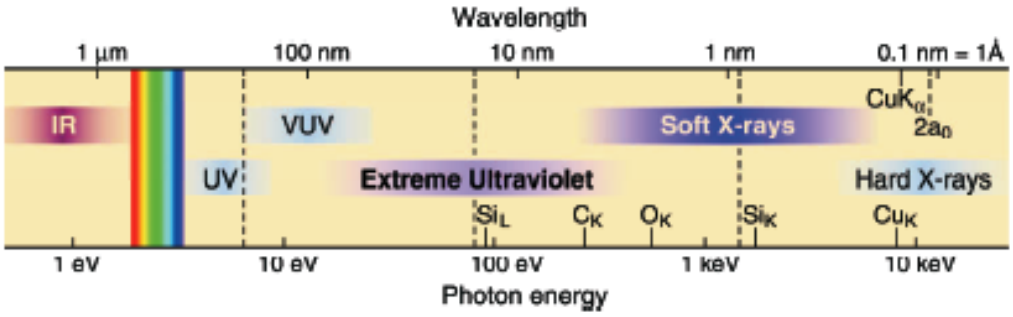

Figure 1.1 - The electromagnetic spectrum in terms of both wavelength (nm) and photon energy (eV) [1].

Moreover the use of coherent EUV radiation can allow for advanced nano-scale metrology and printing techniques such as interferometry and interference lithography. However, use of coherent EUV radiation in numerous areas of science and technology remains relatively unexploited due to the limited access to high power light sources [3-7].

Large multi-user facilities have been constructed to generate radiation at EUV wavelengths. These include third generation synchrotrons [8] and free electron lasers (FELs) [9]. Synchrotrons generate radiation by accelerating electrons to relativistic speeds (energies of GeV) in a storage ring. The change of trajectory of the electrons travelling at these speeds, by bending magnets or undulators, allows for emission of EUV and soft x-ray radiation to be achieved. Although the radiation from synchrotrons is incoherent, filtering can be used to achieve high spatial coherence with the consequence of lower photon flux. Similarly FELs accelerate electrons to relativistic speeds which are then sent through a sequence of alternating magnetic fields (wigglers) spaced such that photons emitted by the electrons are in phase and add coherently. Both of these sources are highly tunable and provide high photon flux; however their size and high cost limit accessibility.

Alternative approaches to sources that can provide EUV radiation, which can be more accessible at a lower cost, are essential for the advancement of applications that can utilize this technology. This has already been demonstrated in numerous disciplines such as surface science [10-13], dense plasma diagnostics [14-18], chemical studies [19-23], nano-scale imaging [24-29] and nano-patterning [30-33]. Therefore there is significant interest for the development of table-top [3, 4, 6] and desk-top [7] size sources that fit in a university or industrial laboratory which can be used for these and other applications. Two common methods for compact EUV generation are high harmonic generation (HHG) and generation from plasma lasers. HHG is a nonlinear process where EUV radiation can be generated by exciting atoms/molecules with an intense optical field [3, 34]. The interaction between the atoms/molecules and the optical field can generate

radiation with frequencies that are integer multiples of the driving frequency. This process can be enhanced significantly if plasma conditions are such that the EUV radiation emitted will add coherently along the interaction length (phase matched) similar to the FEL mentioned above. This source can provide ultrafast EUV pulses that are tunable, however the energy per pulse and average power is typically very low. Average power may be improved by increasing the repetition rate, which is mostly dependent on the driving laser's limitations.

EUV generation from plasma lasers is another common method [6, 35, 36] and is the chosen scheme for experiments conducted at Colorado State University (CSU). EUV plasma lasers are highly monochromatic and normally have a much higher energy per-pulse when compared to the other sources mentioned above. Typically they can be run at several hertz dependent on the method of excitation that is chosen and the wavelength is fixed specific to the material that is used.

1.1.1 Excitation Schemes for EUV Lasers

There are a number of schemes that have been proposed and implemented to obtain lasing in the EUV and soft x-ray regime. Just as in a visible or UV laser, a population inversion in a selected material needs to be achieved. It was realized very early that scaling laser emission to shorter wavelengths posed many challenges due to the larger pump power deposition density necessary to generate large population inversions that are required to achieve sufficient gain in the EUV. Highly ionized atoms have electronic structures suited to create the larger energy transitions needed for EUV emission, therefore the ideal gain medium was seen as plasma [37]. Different population

inversion mechanisms have been proposed to produce the necessary gain for EUV emission. These include photoionization, collisional recombination and electron impact excitation. Using the photoionization method groups have demonstrated amplification in the vacuum ultraviolet region of the electromagnetic spectrum [38-41], but this scheme has not been scaled to the EUV range. Collisional recombination has been successful in demonstrating EUV amplification, although saturation with this scheme has not been observed [42-44]. Electron impact excitation has shown much progress in the development of practical EUV lasers for applications, with saturated operation achieved in many different laboratories at many different wavelengths. This method is well known and is the same mechanism that allows operation of the argon ion [45] and other gas discharge lasers in the visible and ultraviolet regions of the electromagnetic spectrum.

The first EUV collisional electron impact excitation laser was proposed in 1972 by Molchanov [46], but the first physical lasing action was not demonstrated until 1984 by Matthews et al. at Lawrence Livermore National Laboratory (LLNL) [35]. The group at LLNL used a Nd:Glass fusion-class laser system to create highly ionized plasmas from thin foils of selenium heated by a single laser pulse delivered in the form of two counter-propagating pump beams. To create the gain medium the laser beams were focused into 20 μm x 1.12 cm lines creating a plasma column with a large density of Ne-like ions (24 electrons removed). Collisional electron impact excitation generated population inversions in the Ne-like ions that resulted in amplification at 20.63 nm and 20.96 nm [35]. The pump laser used for this demonstration generated kilojoule pulses and could not be fired more than several times per day. However the results encouraged further studies to reduce the required pump energy.

Different EUV laser wavelengths can be generated with highly ionized atoms of different materials. Two common isoelectronic sequences used for amplification are those comprising the Ne-like and Ni-like ionic states (Figure 1.2) which can be created with high abundance over a broad range of plasma temperatures and densities.

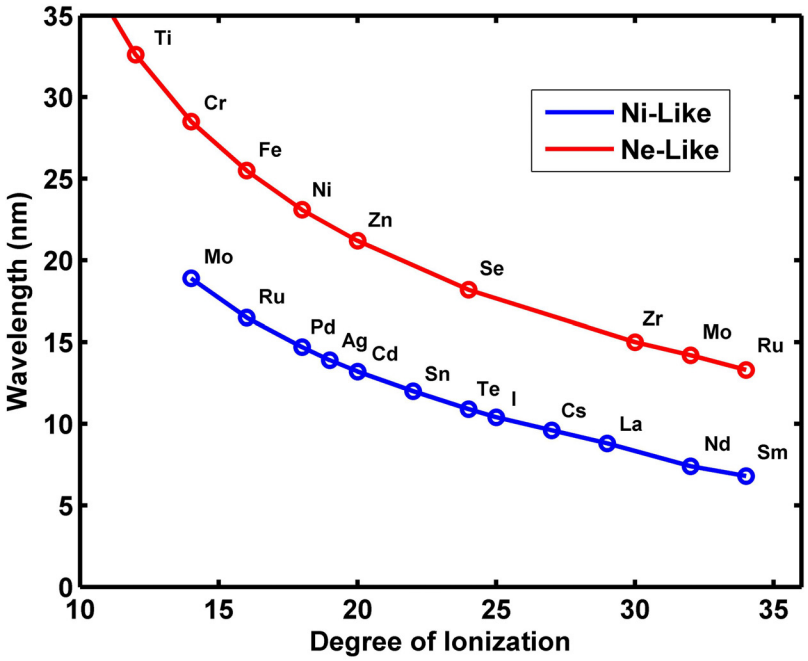

Figure 1.2 - Laser wavelengths emitted by different Ne-like and Ni-like ions versus degree of ionization.

For the efficient generation of short wavelengths Ni-like ions scale faster with respect to the degree of ionization required when compared to the Ne-like series. Therefore the Ni-like scheme is most commonly used to generate short wavelength EUV lasers. The first Ni-like laser was demonstrated in 1987 by Mac-Gowen et al. with Ni-like Eu lasing at 6.583 nm and 7.100 nm [36]. This was accomplished focusing two counter-propagating multi-kJ pulses onto a EuF_2 foil with a peak intensity of 7 x 10^{13} W/cm^2 creating a plasma column consisting of Ni-like ions for amplification. A simplified energy level diagram for Ni-like ions is shown in Figure 1.3.

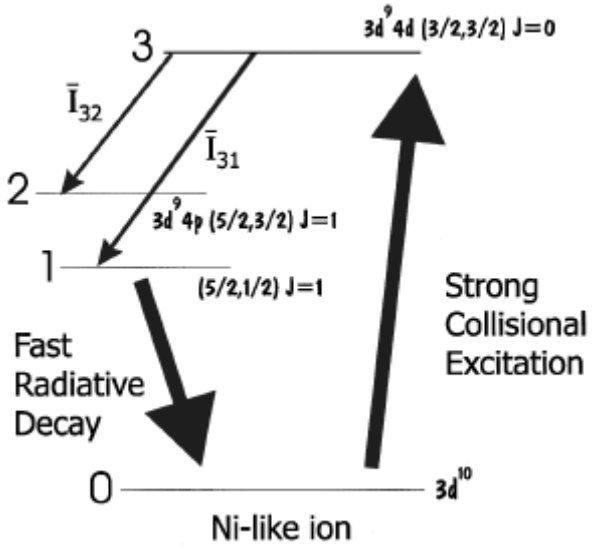

Figure 1.3 –Ni-like energy level structure showing the ground state (0), the laser lower levels (1,2) and the laser upper level (3) [47]

A population inversion is achieved between the 4d and 4p energy levels, resulting in high gain for the J = 0 – 1 transition. This is possible due to the 4p laser lower levels having a fast radiative decay to the Ni-like ground state along with a strong collisional excitation to the laser upper level.

Advancements with respect to the single incident pump pulse scheme have been made in the 1990's by adding a second heating pre-pulse which greatly improved efficiency and laser emission by creating a pre-formed plasma that has time to expand before the driving laser pulse arrives [48-50]. The efficiency improvement can be attributed to the more efficient energy deposition of the main heating pulse farther away from the target surface which increases the area in the plasma where gain occurs. Also the energy is deposited in a region with a lower density gradient reducing refraction of the amplified beam [48]. However it was still difficult to reach saturated operation in many elements without large amounts (> 100 J) of energy in the drive pulse which in turn limited the size and average power of these lasers.

1.1.2 Transient Collisional Excitation of Plasma Lasers

An additional reduction in pump energy was made by shortening the length of the second heating pulse to picosecond duration which will create a larger, transient, population inversion [51, 52]. This is possible because of a larger collisional excitation cross-section of the laser upper level with respect to the laser lower level [53]. For a short time, before collisions re-distribute the populations among the levels, a population inversion an order of magnitude larger than those achieved in a quasi-steady state can be achieved. Although shortening the drive pulse duration creates a high gain, it is only present for picoseconds. Because this is on the order of the time it takes for a photon to travel through the amplifier it imposes a limit to the length of the amplifier that can be used. An obvious solution to this problem is traveling wave excitation (TWE) where the drive pulse is some how delayed with respect to the position along the amplifier. This method was soon demonstrated to increase laser amplification allowing for saturated operation of more Ne-like and Ni-like EUV lasers down to 13.9 nm with reduced driving energy (~10 J) [54-56].

Efficiency was still limited when using normal incidence multi-pulse TWE because only a small percentage of the short pulse energy was deposited in the region optimal for amplification [57]. More recently it has been demonstrated that if a uniform plasma can be created on the surface of the target by a normal incident pump pulse and then rapidly heated by a grazing incidence pump (GRIP) beam (Figure 1.4), a larger percentage of the short pulse energy can be deposited in the optimal amplification region

away from the target surface. This creates a larger population inversion resulting in higher gain [5, 6, 58-61].

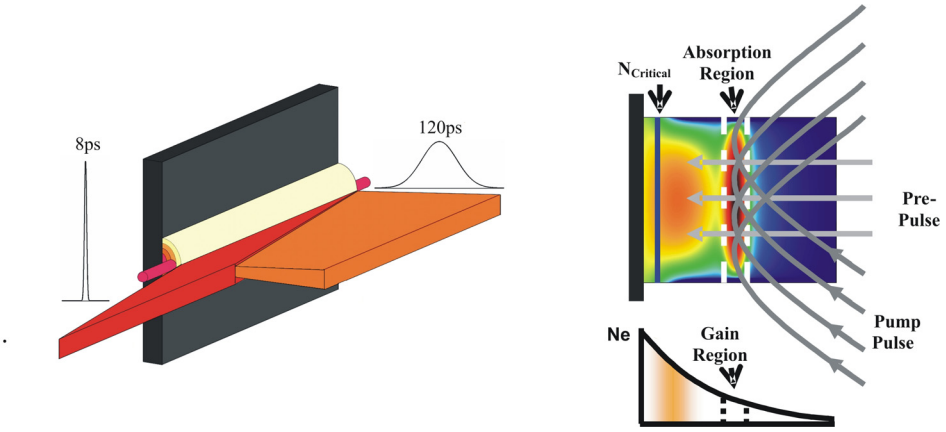

Figure 1.4 - Left: 3D Diagram of the pump beams incident on a slab target. Normal incident pre-pulse heats and ablates the target, the grazing incident pump pulse rapidly heats the plasma generating gain. The EUV laser beam is emitted axially, Right: Simulation of plasma expansion which shows the gain region created by the pump beams [61].

This is accomplished by utilizing refraction of the pump beam in the plasma. Changing the angle of incidence of the GRIP beam, one can tune the maximum electron density at which the energy is deposited. The relation is given in equation 1:

$$\theta = \left(\frac{n_e}{n_c} \right)^{\frac{1}{2}} \tag{1}$$

where θ is the angle incidence with respect to the target surface, n_e is the maximum electron density where energy will be deposited [58, 59] and n_c is the critical electron density for the pump pulse wavelength given by:

$$n_c = \frac{\varepsilon_o m \omega^2}{e^2} \tag{2}$$

where ε_o is the permittivity of free space, m is the mass of an electron, ω is the frequency of the pump laser radiation and e is the charge of an electron. This

scheme is also inherently TWE further increasing energy extraction efficiency although there is still a small mismatch Δt_m shown in Figure 1.5.

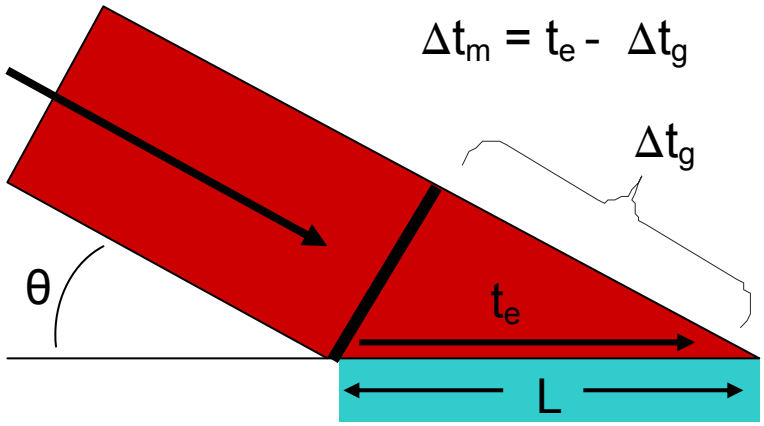

Figure 1.5 Traveling wave excitation from grazing incidence pumping.

Here t_e is the time it takes a EUV photon to travel the length of the amplifier, L is the length of the target, $\Delta t_g = (L/c)\cos(\theta)$ is the time it takes for the pump pulse to be deposited along the target length L and θ is the angle of incidence with respect to the target surface. As long as Δt_m is sufficiently small compared with the gain lifetime no further TWE compensation is needed. Prior to this work this method had been successful to increase the efficiency of generating EUV lasers, allowing saturated operation down to 13.2 nm with less than 2 J of total pump energy [6, 60-62]. Pulse energies up to 2 uJ had been obtained in Ni-like Ag with this pumping configuration at a repetition rate of 5 Hz, realizing a table-top source. Shown in Figure 1.6 are different saturated EUV lasers demonstrated at Colorado State University, including those (Ag & Te) enabled by this work [6, 60-64].

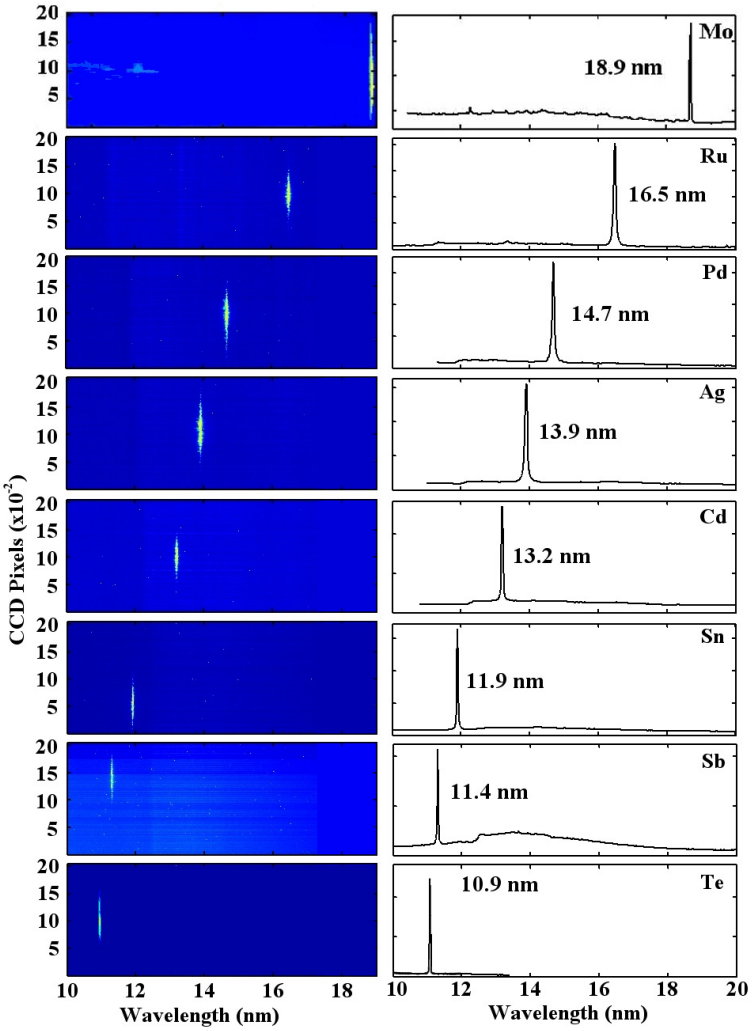

Figure 1.6 - Saturated EUV lasers generated at Colorado State University using the GRIP scheme.

The beam characteristics of the amplified spontaneous emission (ASE) EUV lasers can be further improved by seeding the plasma amplifier [65, 66]. This method has been demonstrated by directing matched femtosecond HHG EUV pulses in frequency, time and space into the plasma amplifier [67]. With this scheme the seed pulse is amplified into saturation. Injection seeding was shown to reduce the beam divergence by an order of magnitude as well as generate picosecond EUV pulses that are shown to be

fully phase (temporal and spatial) coherent. A schematic of the setup used to seed EUV amplifiers created by irradiation of solid targets is shown in Figure 1.7

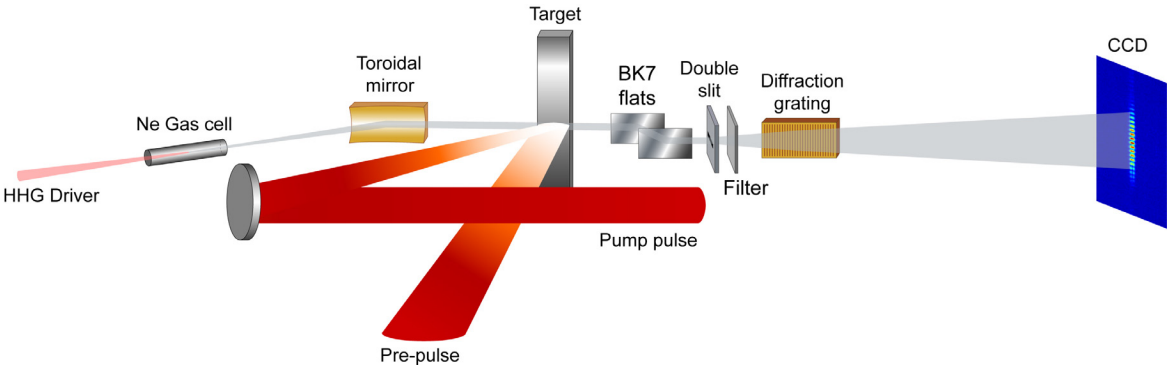

Figure 1.7 – Experimental setup for the seeded EUV laser [67].

Injection seeding has been demonstrated at Colorado State University for a number of different wavelengths including Ne-like Ti at 32.6 nm [66], Ni-like Ag at 13.9 nm (Chapter 7) and Ni-like Cd at 13.2 nm [68].

Success of the optically pumped electron impact excitation EUV laser scheme motivates the scaling of the systems to higher output energies, higher repetition rates and shorter wavelengths for use with applications. To achieve this, advances in the table-top pump laser system to increase the overall energy are needed. A discussion of terawatt laser systems necessary to pump EUV lasers is given below.

1.2 Evolution of Terawatt Laser Systems

Since the invention of the Ruby laser in 1960 [69] there has been a significant effort to increase the intensity of light to study various aspects of our physical world. In 1962 the first significant step for the increase in peak intensity of a laser pulse by many orders of magnitude was accomplished by McClung and Hellwarth [70]. They successfully “optically switched”/”dumped” a laser cavity changing the loss from high to

low (changing the Q of the laser cavity) at the time when there was peak gain in the amplifying medium (ruby in this case). This has become known as cavity dumping or q-switching and is now commonly used to create nanosecond pulses with millijoule level energy out of an oscillator. Another method demonstrated in 1963 called mode-locking allowed for further reduction in the pulse width [71]. This method "phase locked" the oscillating modes in a cavity increasing the intensity of the overall temporal profile. Hargrove et al. synchronized the modes in a He-Ne laser cavity with an acusto-optic modulator. The mode-locking method was eventually able to produce femtosecond pulses with nanojoules of energy [72]. Over the next two decades scientists and engineers worked on many different methods and developed materials to improve the technology available with the goal of increasing the peak intensity of laser pulses for the purposes of studying laser-matter interactions with increased optical fields. Combining mode-locked oscillators with the chirped pulse amplification scheme discussed later in this chapter, large peak pulse powers of up to 1 petawatt have been generated with a single laser pulse [73].

In the 1980s it was recognized that generating short pulses with a large amount of energy and reaching an irradiance of 10^{18} W/cm^2 were both important milestones to reach for the generation of highly ionized and relativistic plasmas, the emission of hard x-rays, the generation of coherent extreme ultraviolet and soft x-ray laser radiation, studying the environments for the advancement of particle accelerators and to move forward on the path towards inertial confinement fusion [4, 74, 75]. The first terawatt laser was demonstrated in 1989 and was an excimer laser system producing 390 fs pulses with 1.5 J energy (~ 4 TW) at a wavelength of 248 nm [76]. However, the excimer scheme had

limitations for further scaling. This is due to the limited extraction efficiency of short pulses through the gain medium due to a low saturation fluence of milijoules per cm^2 [77]. Solid state materials like Nd:Glass have high saturation fluences of joules per cm^2 but can only amplify up to a certain intensity before non-linear effects start to occur destroying the laser beam's wavefront.

To overcome his limitation in 1985 Strickland and Mourou demonstrated a new technique for amplification of ultrashort pulses named chirped pulse amplification (CPA) [78]. This method involves taking an ultrashort pulse and stretching it in time, amplifying and then compressing it back to the original pulsewidth using diffraction gratings. Figure 1.8 shows a diagram illustrating this concept.

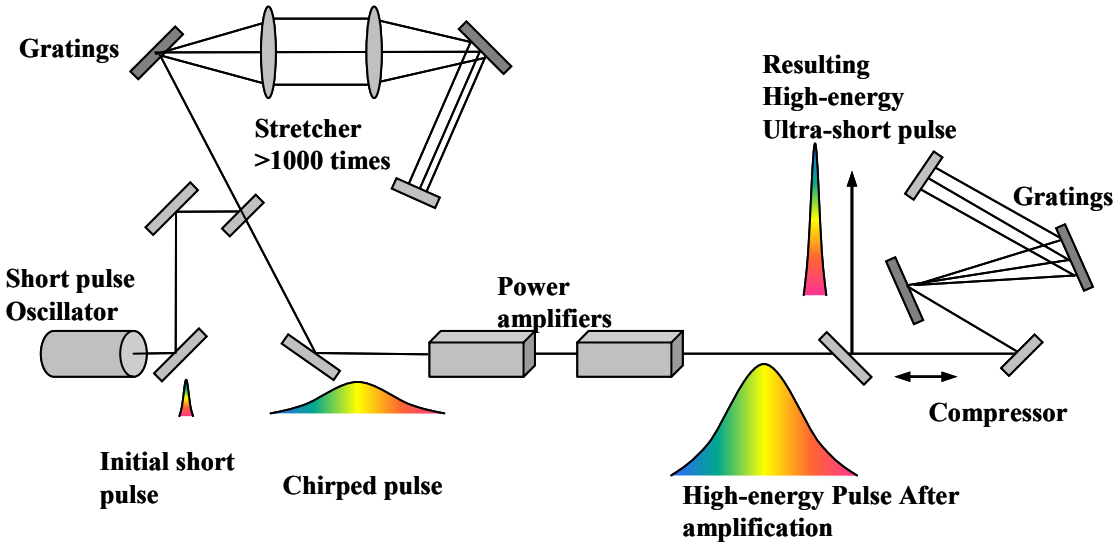

Figure 1.8 - Illustration of a classic CPA laser system.

This allows for reaching saturation fluence on the order of joules per cm^2 (in appropriate materials) while avoiding non-linear effects due to the high intensity of a short pulse. Combined with a method of stretching a pulse using diffraction gratings that matches the compression, dispersion can now be very well compensated (Martinez 1987, [79]) bringing the amplified pulse width down to the transform limit [77, 80]. Later in the same

year that the TW excimer system was demonstrated (1989), a group in France demonstrated the first terawatt laser using the CPA technique with Nd doped materials (i.e. Nd:YLF and Nd:Glass) generating 1.6 J pulses in 0.6 ps [81]. Shortly after this feat an irradiance of 10^{18} W/cm^2 was demonstrated using this laser [82]. This was significant because the scalability of this technology to higher energies was seen as relatively straight forward. Further scaling was demonstrated just about one year later when two groups generated 8.9 J 820 fs pulses and 24 J 1.2 ps pulses, increasing the peak intensity by an order of magnitude [83, 84]. These systems were said to be limited only by the efficiency, damage threshold and size of the diffraction gratings being used at that time.

In addition to increasing the energy in the laser pulse scientists and engineers also reduced the pulse width to further increase the intensity of the laser pulse as well as allow for studying faster dynamics. However the pulse width was limited to about 1 picosecond due to the bandwidth of the glass amplifiers. Because high energy laser pulses suffer significant gain bandwidth narrowing with amplification, it was understood that amplifiers with large bandwidths were required to reach very short pulse widths. Earlier in the 1980s another significant milestone was achieved when a laser was demonstrate using Titanium-Sapphire [85, 86]. This material was expected to have a high potential for creating ultrashort pulses because of the broad bandwidth stimulated emission cross-section (~ 235 nm FWHM) [86] along with other favorable properties such as good thermal conductivity, high damage threshold and a saturation fluence of 1-2 J/cm^2 [87]. Eventually a Ti:Sapphire oscillator was mode-locked using the passive Kerr lens method [72] and just two months later the first terawatt Ti:Sapphire laser was demonstrated by Sullivan et al. [88]. This laser generated 60 fs pulses with 0.23 J energy at 10 Hz

repetition rate. Shown in Figure 1.9 is an example of the measured bandwidth from a typical laser pulse generated by the CSU Ti:Sapphire oscillator. This bandwidth of 37 nm FWHM can support ~ 25 fs transform limited laser pulses.

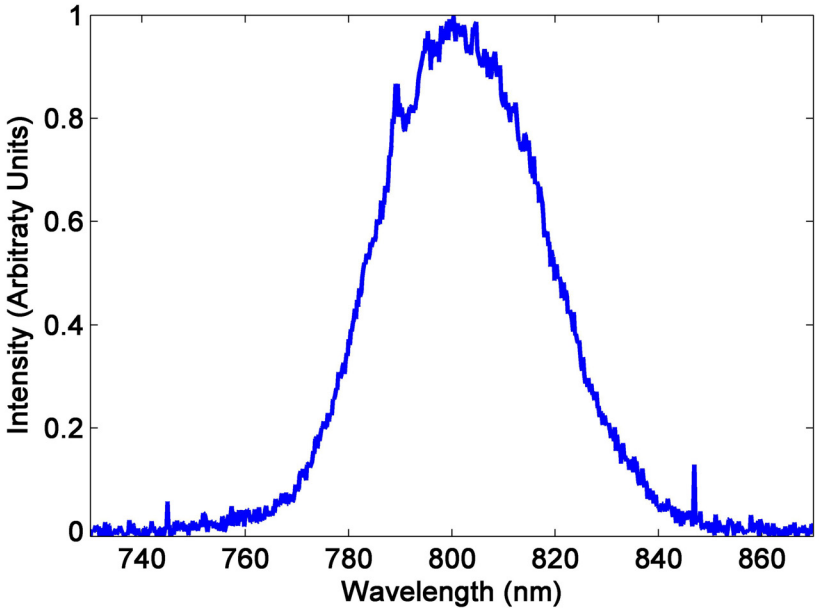

Figure 1.9 – Measured bandwidth of laser pulses from the CSU Ti:Sapphire oscillator

This advancement significantly reduced the size and complexity of terawatt laser systems and laid the groundwork towards a more compact approach to the petawatt regime. Both Ti:Sapphire and Nd doped materials have been used to generate petawatt laser pulses and are currently the most commonly for this application [73, 89].

In this dissertation both Nd:YLF/Nd:Glass and Ti:Sapphire laser technologies are discussed. Since the upper level lifetime of Ti:Sapphire is only ~3 μs the gain medium needs to be excited by a fast pumping method (faster than flashlamps). Also, Titanium-Sapphire has a strong absorption in the green region of the electromagnetic spectrum. Therefore frequency doubled nanosecond pulses generated by Q-switched Nd:YAG or Nd:YLF lasers are optimal for the pumping of Ti:Sapphire amplifiers. We use this

method to generate 800 nm high energy picosecond laser pulses for the generation of EUV radiation from laser-created plasmas. Although the pumping scheme that is used for the generation of these plasma laser amplifiers requires only ~10^{13} W/cm^2 [5, 6], multi-joule energies are necessary to create a large enough gain medium to observe significant amplification. The pump laser system built for this purpose is described herein.

1.3 Ti:Sapphire Laser System Design

The pump laser system used for EUV laser experiments conducted at Colorado State University consists of a titanium-sapphire oscillator and an amplifier chain which produces pulses centered at a wavelength of ~ 800 nm. The system achieves high energy with multiple stages of amplification using the CPA technique [78]. Ultrashort pulses are generated by a mode-locked Ti:Sapphire oscillator. These pulses are subsequently stretched by a Martinez stretcher [79] and are then amplified by three stages of amplification. They are then recompressed by a grating compressor [90] and are ejected from the system. Before compression a fraction of the beam is split and directed to the target chamber creating a longer pre-pulse for EUV laser generation. Figure 1.10 shows a schematic diagram illustrating the different stages of the CPA laser system. Between each stage of amplification there is an imaging telescope used to expand the beam to match the stage's pump laser mode. At the focus of these telescopes are spatial filters (SF) placed to remove any high frequency structure from the beam's intensity profile. Isolation between each amplifier is provided by a Pockels Cell (PC) polarizing beam splitter (PBS) waveplate (WP) combination. The PBS pairs are crossed to avoid transmission unless the PC rotates the polarization of the laser pulse.

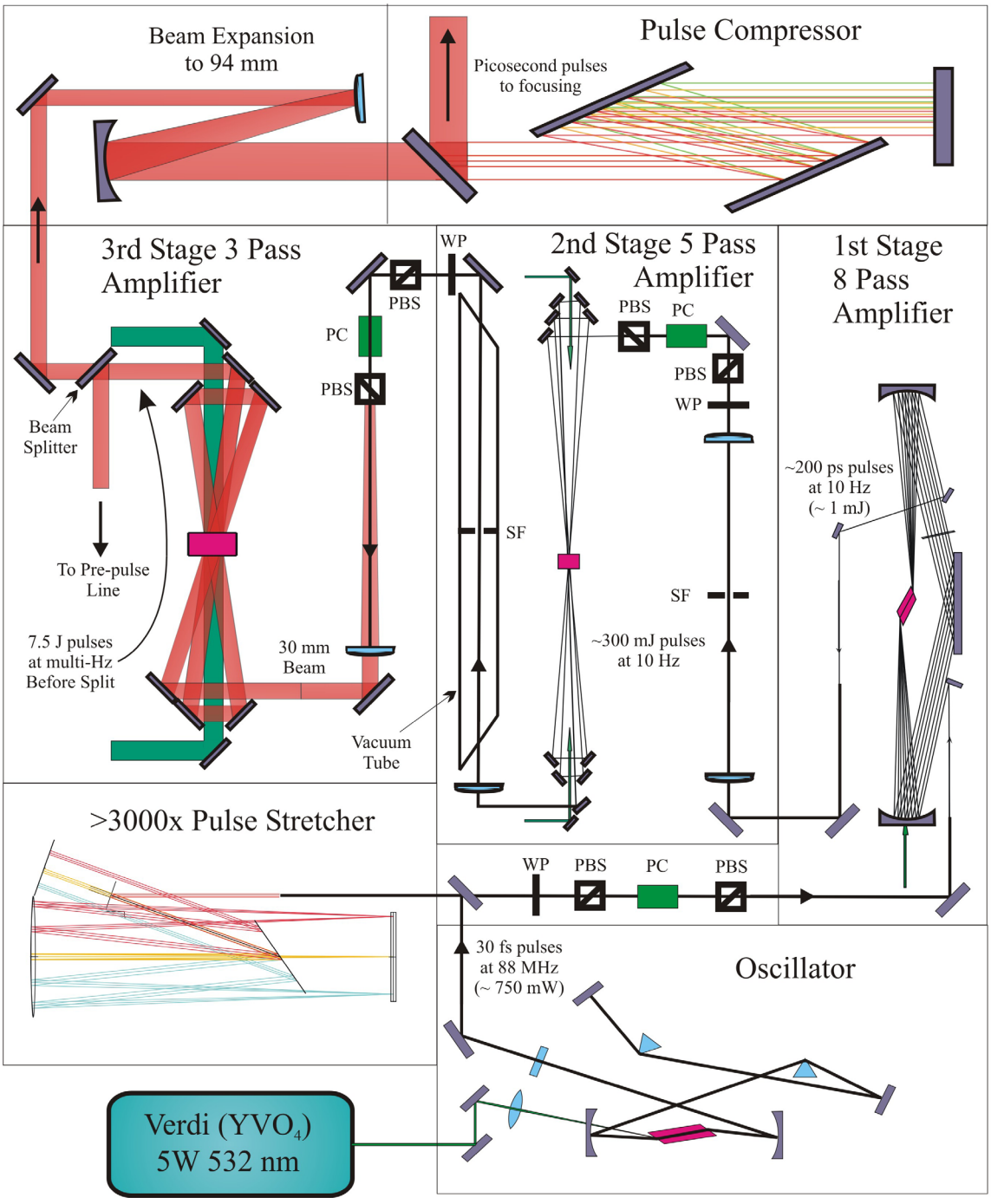

Figure 1.10 – Schematic diagram of Ti:Sapphire CPA EUV driving laser system.

This is necessary to reduce amplified spontaneous emission feedback between the high gain amplifiers which can reduce energy extraction. If a sufficiently small window is

created with the Pockels cell the isolation combination along with the spatial filters can also reject any stray back reflections that may arise in the system. This can reduce the possibility of high intensity focuses that can damage components. Each part of the system is discussed in more detail below.

1.3.1 Oscillator

The seed pulse is generated by a Ti:Sapphire mode-locked oscillator. There are several methods that can be used to induce mode-locking in a laser oscillator which may be passive or active. The commercially available oscillator used at CSU uses a passive method known as Kerr lens mode-locking [72]. This method uses non-linear self-focusing to allow or reject oscillating modes in the cavity. The radiation inside the cavity has a Gaussian intensity spatial distribution transverse to the direction of propagation. When the laser intensity is sufficient the Ti:sapphire crystal acts as a lens due to the self-focusing Kerr effect. The cavity can be setup accounting for this effective lens allowing only modes that are influenced by it to survive. To achieve this, suppose some modes incidentally are phase locked and interfere constructively forming a pulse that has higher intensity than the modes with random phases. These pulses are focused and thereby collimated in the cavity, surviving and seeing gain with low loss. All other modes that are not affected are thus not collimated and are rejected by suffering high losses. This allows for the high intensity modes in phase to “win out” and reach relatively high energy. Eventually only modes oscillating in phase creating the mode-locked pulses survive.

The oscillator used in our laboratory was built by KM Labs [91] and produces ~ 750 mW of ~ 30 fs pulses at 88 MHz. A typical pump power of 4.7 W from a continuous wave Nd:YVO_4 532 nm laser (Coherent-Verdi [91]) is used. Dispersion compensation is necessary to obtain short pulses due to self phase modulation and group velocity dispersion occurring in the Ti:Sapphire crystal. This is accomplished with a prism pair (P1 & P2) inserted in the cavity [92, 93] shown in Figure 1.11. Steering mirrors are used (M) to direct the beam and create a cavity for oscillation. The two concave mirrors (CM) are used to focus the beam onto the Ti:Sapphire rod creating conditions for mode-locked operation with the thermal lens that develops in the amplifier. A 17% output coupler (OC) is used to eject pulses from the cavity to the pulse stretcher.

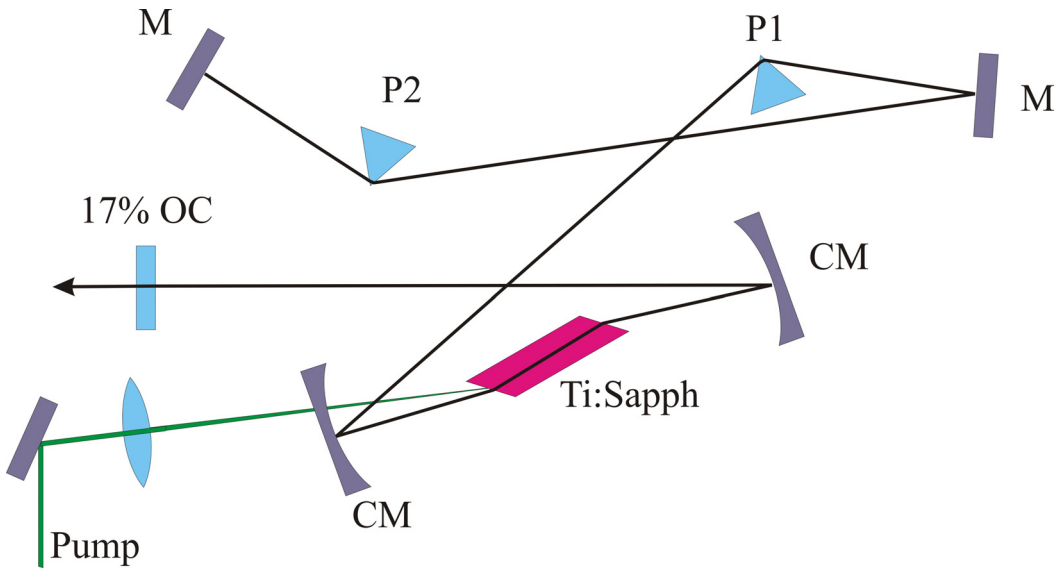

Figure 1.11 – Schematic Diagram of the Ti:Sapphire Oscillator

1.3.2 Stretcher/Compressor Pair

Our CPA laser system takes pulses from the oscillator and stretches them in time through a positive dispersion delay stage. The pulses are amplified and then compressed back to shorter pulsewidths in a negative dispersion delay stage. The stretcher and compressor consist of multilayer-dielectric (MLD) diffraction gratings. The design is setup to stretch 30 fs pulses to ~ 300 ps.

Gratings are commonly used to create an optical delay line by applying angular dispersion onto the phase front of the beam [90]. Exploiting this effect it is possible to create a linear path difference between the longer and shorter wavelengths that make up an ultrafast optical pulse thus lengthening or shortening the temporal width. When the stretcher (positive GVD grating pair) was invented it was setup in two configurations by Martinez et al. [79]. The scheme uses an imaging system inserted in a grating delay line to achieve an effective negative optical path. This trick switches the sign of the dispersion. The first scheme was implemented using two lenses, two gratings and an injection and sendback mirror (Figure 1.12).

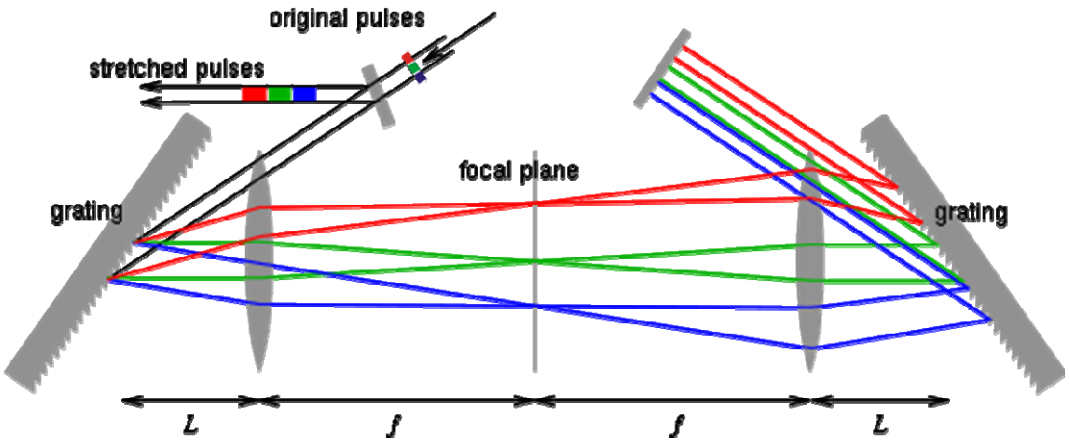

Figure 1.12 – Schematic diagram of a positive GVD grating pair delay line [94].

If the distance given by L is smaller than f (L < f) the stage will add positive group delay dispersion to the pulse given by:

$$\frac{\partial^2 \phi}{\partial \omega^2} = -\frac{2(L-f)N^2\lambda^3}{\pi c^2 \cos^3\theta} \tag{3}$$

where L is the distance of the grating from the lens and λ is the center wavelength, N is the groove density (l/mm), c is the speed of light and θ is the diffracted angle. If L > f the stage will put negative dispersion on the pulse negating the need for the telescope. The change in pulse width after stretch is given geometrically by:

$$\Delta\tau = \frac{L_g\left(\frac{\lambda}{d}\right)\Delta\lambda}{cd\left(1-\left(\frac{\lambda}{d}-\sin\gamma\right)^2\right)} \tag{4}$$

where L_g is the grating separation (in this case it is equal to 2(L-f)), Δλ is the bandwidth of the laser pulse, d is the groove spacing and γ is the angle of incidence on the first grating with respect to normal The design of the positive delay grating pair can be further improved by first using concave mirrors instead of lenses. This will remove any dispersion that would be acquired by the beam passing through the lens material. Also, if a flat normal incidence mirror is placed at the focal plane of the focusing mirror, the setup can be folded back upon itself. This technique reduces the number of optics and space that is required. Figure 1.13 illustrates this setup.

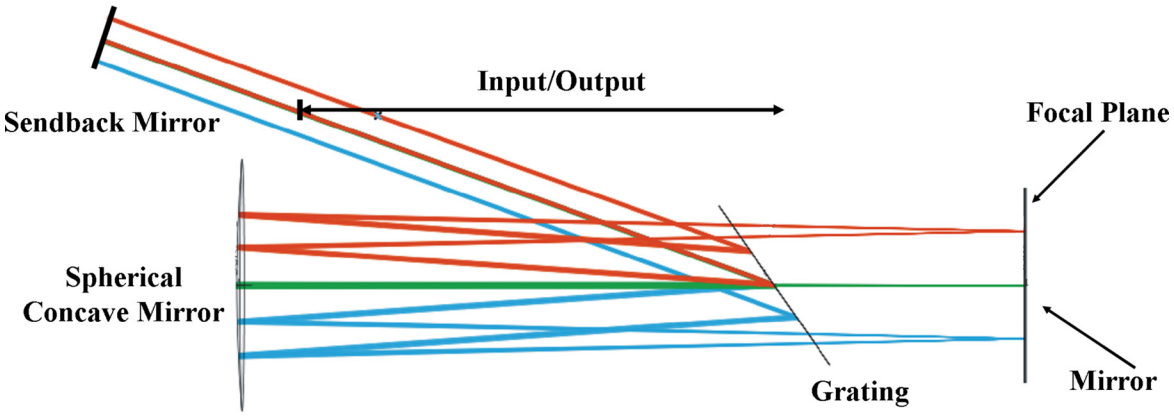

Figure 1.13 – Schematic diagram of a folded positive GVD grating delay line.

Figure 1.14 shows a raycad simulation of the stretcher used in our system. It is setup using a 1740 l/mm multi-layer dielectric (MLD) grating with a Littrow angle of 44.1 degrees. The input angle to the grating is 55 degrees from the normal. The simulation shows the placement of the grating as well as the flat mirror at the focus (152 mm wide). The send back mirror is 101 mm long.

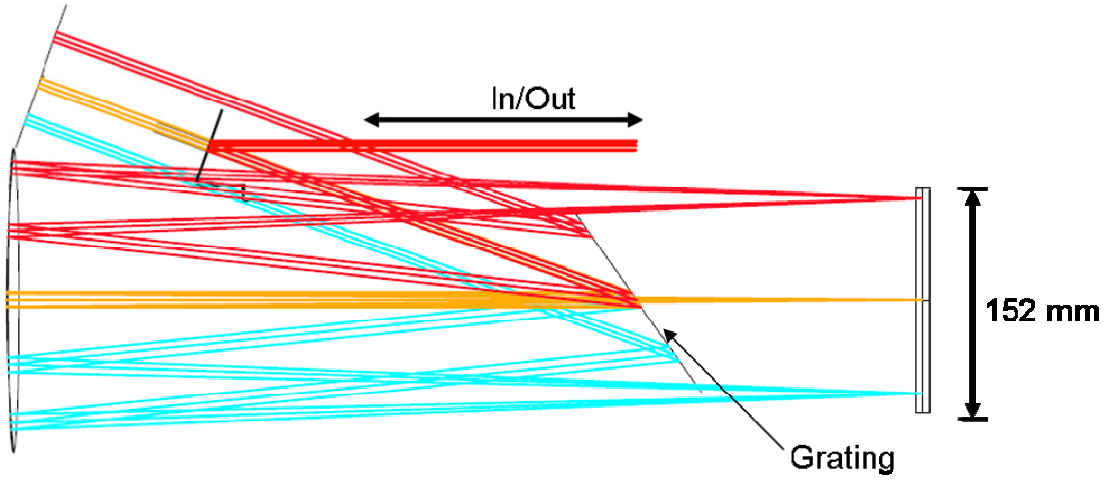

Figure 1.14 – Raycad simulation of the folded positive GVD grating pair delay line.

The spherical focusing mirror is 203 mm in diameter and has a focal length of 609.6 mm. The separation of the center of the spherical mirror and the center of the grating is ~ 419 mm. The raycad simulation shows a bandwidth acceptance of 100 nm centered at 800 nm. With these parameters the calculated stretch is ~ 300 ps. A photograph of the MLD stretcher is presented in Figure 1.15.

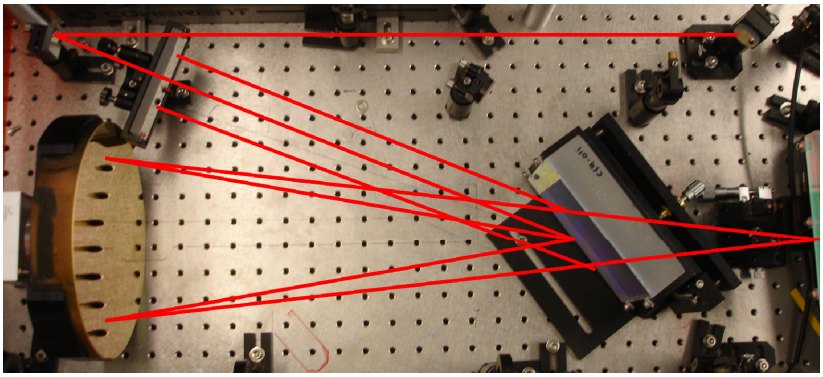

Figure 1.15 - Photograph of the MLD stretcher with lines superimposed to guide the eye.

The grating compressor was first demonstrated by Treacy et al. in 1969 [90]. Our compressor is setup using two parallel gratings (Figure 1.16) separated by a distance L_g.

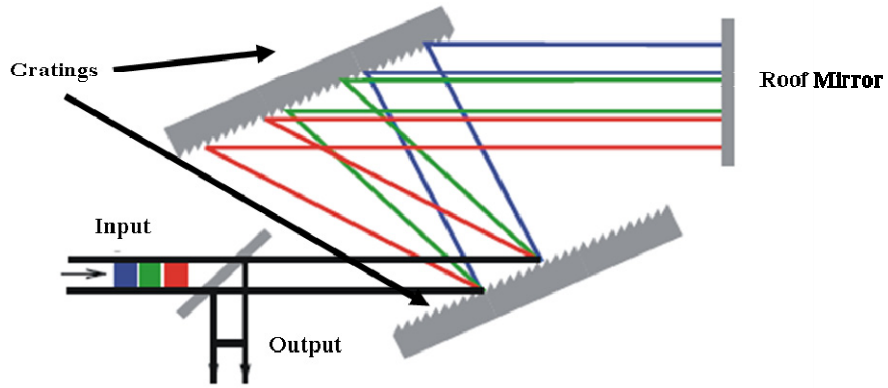

Figure 1.16 – Schematic diagram of a grating compressor [94].

This configuration adds negative dispersion to the pulse given by equation 3 replacing "2(L-f)" with L_g. The compressor used in our system consists of four 9" x 4.5" 1740 l/mm MLD gratings developed for this system (two are shown in Figure 1.18). MLD gratings have the potential for increased diffraction efficiency, damage threshold and high average power operation when compared with gold gratings. These aspects are extremely important for the compressor stage of CPA laser systems allowing for higher energy and higher average power operation. This has been demonstrated with 1 μm gratings [95] and has now been extended to picosecond 800 nm laser systems and is part of the work presented in this dissertation. These novel MLD gratings are discussed in detail in Chapter 4. Figure 1.17 shows a raycad simulation of the compressor. It verifies a beam size acceptance of 9.4 cm with a bandwidth acceptance of 65 nm. The perpendicular grating separation is ~ 323 mm.

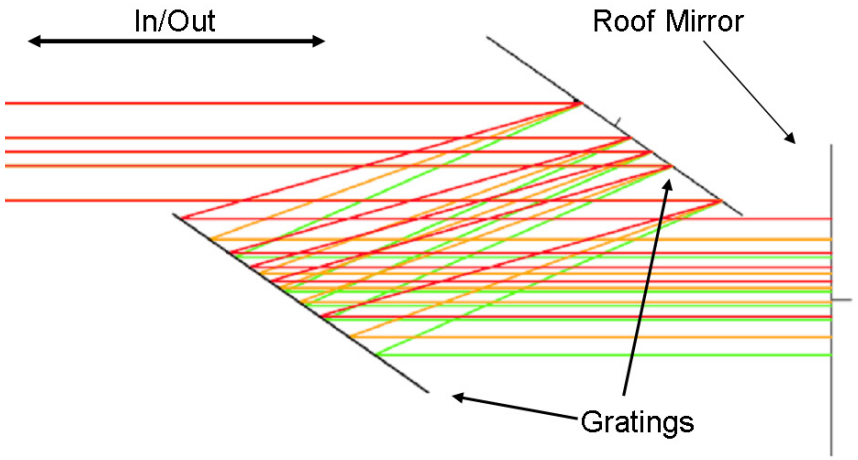

Figure 1.17 – Raycad simulation of compressor.

The compressor also employs a pair of 4" x 6" input 45 degree MLD mirrors and a roof mirror that consists of two 6" x 6" 45 degree MLD mirrors mounted in a custom

mount designed in house (Figure 1.18). It is known that substrates coated with a dielectric stack can deform due to stress in the films. Therefore one must take great care during material deposition to minimize the deformation of the substrates. The stress induced in the material can vary depending on the deposition method used. Furthermore the substrate material can also affect the overall deformation that is produced after the thin film is deposited. Due to the large size of these mirrors there are stringent reflected wavefront requirements to maintain the high quality phase front on the beam.

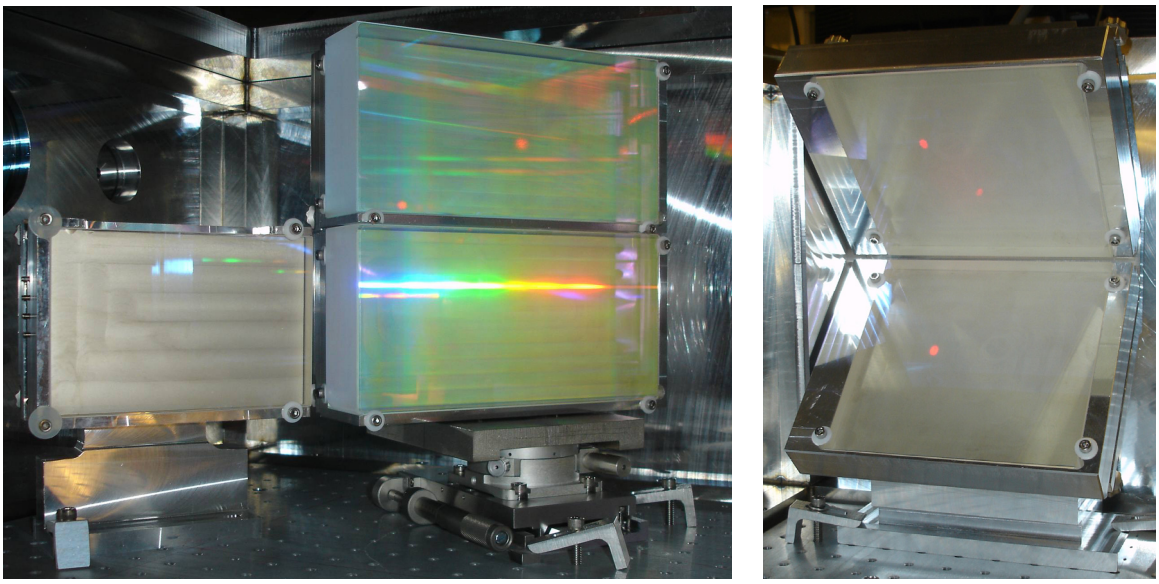

Figure 1.18 – Photographs of MLD grating pulse compressor, Left: Two 9" x 4.5" MLD diffraction gratings along with a 4" x 6" 45 degree mirror and Right: Roof mirror containing two 6" x 6" 45 degree mirrors.

This is necessary to produce a sufficiently small line focus width after pulse compression. The fused silica substrate's wavefront variation specification before the MLD quarter wave stack is deposited is to have a variation better than lambda(λ)/10 @ 633 nm. After coating the substrates used in the compressor did not change by more than 20% (better

than λ /8). Wavefront reflection was verified before and after coating using a normal incidence Zygo interferometer.

1.3.3 Amplification Stages

The first stage of amplification is a multi-pass configuration [96]. The pulse train produced by the oscilliator is directed from the stretcher through a PC/PBS pair. This changes the repetition rate from 88 MHz to 10 Hz. The beam is then focused onto a Brewster angle Ti:Sapphire crystal using two 0.5 m focal length mirrors and a flat mirror (Figure 1.19) where it is amplified in eight passes. As discussed before, the pumping of Ti:Sapphire amplifiers require relatively short pumping sources (i.e. ns laser pulses versus flashlamps) due to the short radiative lifetime of ~ 3 μs. This stage is pumped at 10 Hz by a frequency doubled Q-switched Nd:YAG laser. This laser is a commercially available Qunta-Ray produced by Spectra Physics that generates ~ 800 mJ 10 ns pulses. A fraction of this energy (~ 13 mJ) is focused into the crystal with a spot size of ~800 μm.

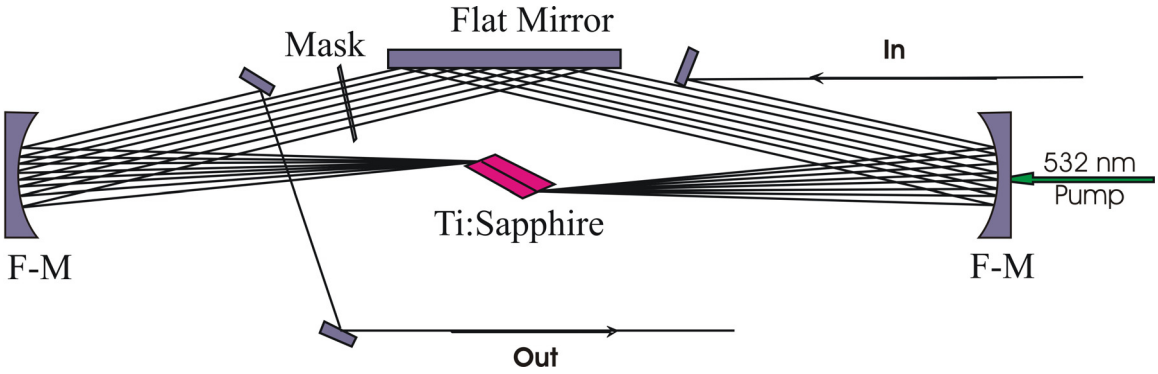

Figure 1.19 – Schematic diagram of the 1st stage Ti:Sapphire amplifier

The crystal is mounted to a copper finger that is water cooled maintaining the temperature to any desired value. A good thermal contact created using indium foil

maximizes cooling efficiency. There is a mask inserted into the cavity which has eight apertures spaced 1 mm apart to control the beam size and reduce ASE between passes. After eight passes the 800 nm laser pulses are amplified by a factor of 10^6 raising the energy from ~1 nJ to ~1 mJ.

After the first stage amplifier the beam passes through a spatial filter and a PC/PBS pair. This provides isolation between the 1st and 2nd stage amplifiers as well as maintains good beam quality. It also allows for the minimization of pre-pulses that arise in the first stage amplifier, although depending on the quality of the polarization rotation and polarizer performance the control is limited to a contrast ratio of ~ 10^8. If there is a need for a cleaner temporal profile, other methods should be implemented.

The second stage of amplification consists of a five pass bowtie amplifier. The beam size in this amplifier is 6 mm with the faces of the crystal cut at normal incidence. This configuration requires the faces to have an anti-reflective coating that minimizes the back reflection of both the 800 nm beam as well as the 532 nm pump beam. A SiO_2/HfO_2 multilayer stack is used to minimize the reflections of both wavelengths. The remaining energy for the frequency doubled Nd:YAG pump laser is directed into this amplifier (50% to either side). Figure 1.20 shows a schematic diagram of this amplifier which operates at 10 Hz and is cooled in the same fashion as the 1st stage crystal. The pulse energy is amplified by a factor of ~ 3 x 10^2 raising the energy from ~ 1 mJ to ~ 300 mJ.

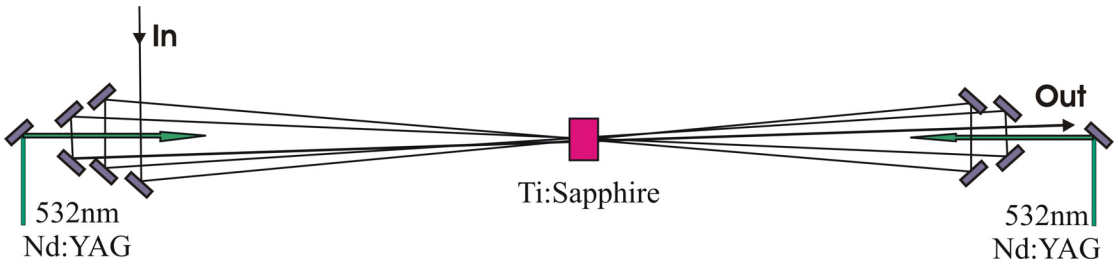

Figure 1.20 – Schematic Diagram of the 2nd stage amplifier.

After the 2nd stage amplifier the beam is again directed through a spatial filter and PC/PBS combination. The beam is then sent into the third stage of amplification. This stage consists of a three pass bowtie amplifier pumped by 20 J λ = 527 nm ~ 15 ns laser pulses (shown in Figure 1.21). The beam size in this amplifier is 30 mm.

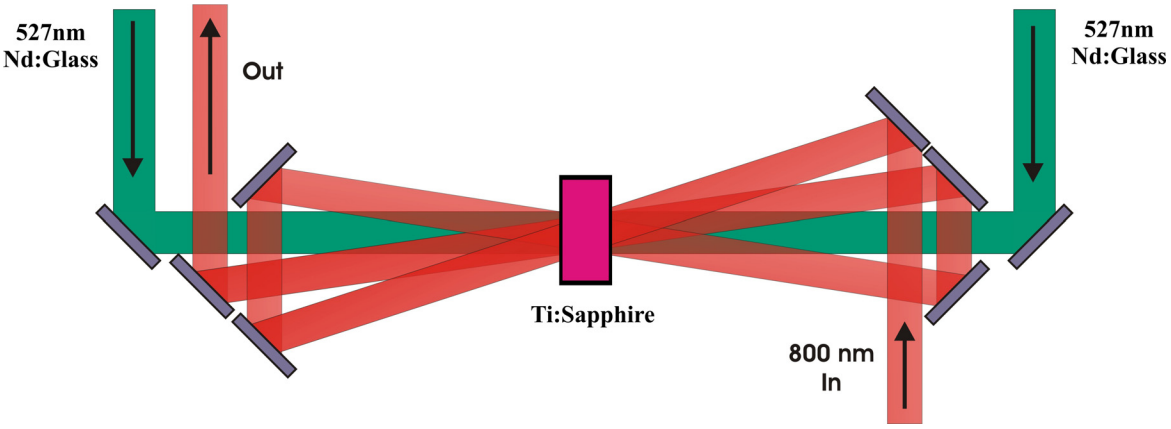

Figure 1.20 - Schematic Diagram of the 3rd stage amplifier

A 60 mm diameter, 30 mm thick Ti-doped sapphire crystal is used. The crystal was grown by Crystal Systems [91] and has 95% absorption from a single pass for 532 nm radiation. The crystal is temperature controlled by flowing coolant around the circumference of the curved surface. This method was chosen, instead of contacting the crystal to a heat sink, to allow for the substitution of water with a high index fluid. This can reduce transverse ASE feedback in the amplifying medium and prevent parasitic lasing due to reflections at the interface [97] when the pumping is increased. Similar to the second stage amplifier the faces are coated with an AR multi-layer stack to minimize both 527 nm and 800 nm back reflections. The pump beams for this amplifier are delivered by a two arm high energy Nd:Glass frequency doubled Zig-Zag slab laser developed in house. The slab laser system is discussed in chapters 2, 3 and 5.

This Ti:Sapphire laser system, including the third stage amplifier, has been successfully operated at repetition rates up to 2.5 Hz generating 7.5 J pulses. Figure 1.21 shows operation at 1 Hz repetition rate with a shot-to-shot standard deviation of less than 1% as well as an example of the resulting beam profile.

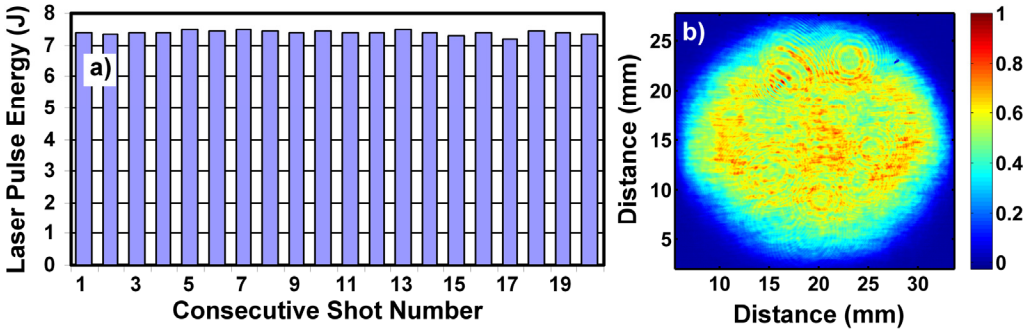

Figure 1.21 - (a) Shot to shot variation of amplified λ = 800 nm Ti:Sapph laser pulse energy measured at 1Hz rep. rate. The average laser pulse energy is 7.4 J and the standard deviation σ = 1%. (b) Typical intensity profile of the amplified λ = 800 nm beam.

The uniform beam profile along with good shot to shot stability allows for the use of this system as a EUV laser driver.

1.4 Foreword

The next two chapters discuss the fundamentals and implementation of the Nd:Glass Zig-Zag slab amplifier utilized in the third stage 20 J pump laser. Chapter four discusses the design and fabrication of novel multi-layer dielectric diffraction gratings for compression of high energy 800 nm laser pulses. Chapters five and six summarize EUV laser results obtained using the pump laser described in this dissertation. Chapter five describes the demonstration of a 20 μW average power λ = 13.9 nm Ni-like Ag laser. Chapter six summarizes recent results from the application of the CPA Ti-Sapphire pump laser for EUV laser science. This includes the study of beam characteristics generated by

the seeded operation of the Ni-like Ag laser and the extension of saturated table-top EUV laser operation to shorter wavelengths utilizing Ni-like tellurium operating at λ = 10.9 nm.

1.5 References

1. D. T. Attwood, *Soft X-Rays and Extreme Ultraviolet Radiation* (Cambridge University, Cambridge, England, 1999).
2. S. Suckewer and C. H. Skinner, "Soft x-ray lasers and their applications," Science **247**, 1553-1557 (1990).
3. Z. Chang, A. Rundquist, H. Wang, M. M. Murnane, and H. C. Kapteyn, "Generation of Coherent Soft X Rays at 2.7 nm Using High Harmonics," Physical Review Letters **79**, 2967 (1997).
4. J. J. Rocca, "Table-top soft x-ray lasers," Review of Scientific Instruments **70**, 3799 (1999).
5. R. Keenan, J. Dunn, P. K. Patel, D. F. Price, R. F. Smith, and V. N. Shlyaptsev, "High-Repetition-Rate Grazing-Incidence Pumped X-Ray Laser Operating at 18.9 nm," Physical Review Letters **94**, 103901 (2005).
6. B. M. Luther, Y. Wang, M. A. Larotonda, D. Alessi, M. Berrill, M. C. Marconi, J. J. Rocca, and V. N. Shlyaptsev, "Saturated high-repetition-rate 18.9-nm tabletop laser in nickellike molybdenum," Optics Letters **30**, 165-167 (2005).
7. S. Heinbuch, M. Grisham, D. Martz, and J. J. Rocca, "Demonstration of a desk-top size high repetition rate soft x-ray laser," Opt. Express **13**, 4050-4055 (2005).
8. J. H. Underwood, E. M. Gullikson, M. Koike, P. J. Batson, P. E. Denham, K. D. Franck, R. E. Tackaberry, and W. F. Steele, "Calibration and standards beamline 6.3.2 at the Advanced Light Source" (1996), retrieved.
9. W. Ackermann_et_al, "Operation of a free-electron laser from the extreme ultraviolet to the water window," Nat Photon **1**, 336-342 (2007).

10. L. Miaja-Avila, C. Lei, M. Aeschlimann, J. L. Gland, M. M. Murnane, H. C. Kapteyn, and G. Saathoff, "Laser-Assisted Photoelectric Effect from Surfaces," Physical Review Letters **97**, 113604 (2006).

11. G. Saathoff, L. Miaja-Avila, M. Aeschlimann, M. M. Murnane, and H. C. Kapteyn, "Laser-assisted photoemission from surfaces," Physical Review A **77**, 022903 (2008).

12. L. Miaja-Avila, J. Yin, S. Backus, G. Saathoff, M. Aeschlimann, M. M. Murnane, and H. C. Kapteyn, "Ultrafast studies of electronic processes at surfaces using the laser-assisted photoelectric effect with long-wavelength dressing light," Physical Review A **79**, 030901 (2009).

13. M. E. Siemens, Q. Li, M. M. Murnane, H. C. Kapteyn, R. Yang, E. H. Anderson, and K. A. Nelson, "High-frequency surface acoustic wave propagation in nanostructures characterized by coherent extreme ultraviolet beams," Applied Physics Letters **94**, 093103-093103 (2009).

14. J. J. Rocca, E. C. Hammarsten, E. Jankowska, J. Filevich, M. C. Marconi, S. Moon, and V. N. Shlyaptsev, "Application of extremely compact capillary discharge soft x-ray lasers to dense plasma diagnostics," Physics of Plasmas **10**, 2031-2038 (2003).

15. J. Filevich, J. J. Rocca, M. C. Marconi, R. F. Smith, J. Dunn, R. Keenan, J. R. Hunter, S. J. Moon, J. Nilsen, A. Ng, and V. N. Shlyaptsev, "Picosecond-Resolution Soft-X-Ray Laser Plasma Interferometry," Appl. Opt. **43**, 3938-3946 (2004).

16. J. Filevich, J. J. Rocca, M. C. Marconi, S. J. Moon, J. Nilsen, J. H. Scofield, J. Dunn, R. F. Smith, R. Keenan, J. R. Hunter, and V. N. Shlyaptsev, "Observation of a Multiply Ionized Plasma with Index of Refraction Greater than One," Physical Review Letters **94**, 035005 (2005).

17. J. Filevich, J. Grava, M. Purvis, M. C. Marconi, J. J. Rocca, J. Nilsen, J. Dunn, and W. R. Johnson, "Prediction and observation of tin and silver plasmas with index of refraction greater than one in the soft x-ray range," Physical Review E **74**, 016404 (2006).

18. J. Grava, M. A. Purvis, J. Filevich, M. C. Marconi, J. J. Rocca, J. Dunn, S. J. Moon, and V. N. Shlyaptsev, "Dynamics of a dense laboratory plasma jet investigated using soft x-ray laser interferometry," Physical Review E **78**, 016403 (2008).

19. F. Dong, S. Heinbuch, S. G. He, Y. Xie, J. J. Rocca, and E. R. Bernstein, "Formation and distribution of neutral vanadium, niobium, and tantalum oxide clusters: Single photon ionization at 26.5 eV," The Journal of Chemical Physics **125**, 164318-164318 (2006).

20. F. Dong, S. Heinbuch, J. J. Rocca, and E. R. Bernstein, "Dynamics and fragmentation of van der Waals clusters: (H2O)n, (CH3OH)n, and (NH3)n upon ionization by a 26.5 eV soft x-ray laser," The Journal of Chemical Physics **124**, 224319-224317 (2006).

21. S. Heinbuch, F. Dong, J. J. Rocca, and E. R. Bernstein, "Single photon ionization of hydrogen bonded clusters with a soft x-ray laser: (HCOOH)x and

(HCOOH)y(H2O)z," The Journal of Chemical Physics **126**, 244301-244311 (2007).

22. Y. Xie, F. Dong, S. Heinbuch, J. J. Rocca, and E. R. Bernstein, "Investigation of the reactions of small neutral iron oxide clusters with methanol," The Journal of Chemical Physics **130**, 114306-114311 (2009).

23. S. Heinbuch, F. Dong, J. J. Rocca, and E. R. Bernstein, "Experimental and theoretical studies of reactions of neutral vanadium and tantalum oxide clusters with NO and NH3," The Journal of Chemical Physics **133**, 174314-174311 (2010).

24. Berglund, Rymell, Peuker, Wilhein, and Hertz, "Compact water-window transmission X-ray microscopy," Journal of Microscopy **197**, 268-273 (2000).

25. F. Brizuela, G. Vaschenko, C. Brewer, M. Grisham, C. Menoni, M. Marconi, J. Rocca, W. Chao, J. Liddle, E. Anderson, D. Attwood, A. Vinogradov, I. Artioukov, Y. Pershyn, and V. Kondratenko, "Reflection mode imaging with nanoscale resolution using a compact extreme ultraviolet laser," Opt. Express **13**, 3983-3988 (2005).

26. G. Vaschenko, C. Brewer, F. Brizuela, Y. Wang, M. A. Larotonda, B. M. Luther, M. C. Marconi, J. J. Rocca, C. S. Menoni, E. H. Anderson, W. Chao, B. D. Harteneck, J. A. Liddle, Y. Liu, and D. T. Attwood, "Sub-38 nm resolution tabletop microscopy with 13 nm wavelength laser light," Opt. Lett. **31**, 1214-1216 (2006).

27. C. A. Brewer, F. Brizuela, P. Wachulak, D. H. Martz, W. Chao, E. H. Anderson, D. T. Attwood, A. V. Vinogradov, I. A. Artyukov, A. G. Ponomareko, V. V.

Kondratenko, M. C. Marconi, J. J. Rocca, and C. S. Menoni, "Single-shot extreme ultraviolet laser imaging of nanostructures with wavelength resolution," Opt. Lett. **33**, 518-520 (2008).

28. F. Brizuela, Y. Wang, C. A. Brewer, F. Pedaci, W. Chao, E. H. Anderson, Y. Liu, K. A. Goldberg, P. Naulleau, P. Wachulak, M. C. Marconi, D. T. Attwood, J. J. Rocca, and C. S. Menoni, "Microscopy of extreme ultraviolet lithography masks with 13.2 nm tabletop laser illumination," Opt. Lett. **34**, 271-273 (2009).

29. F. Brizuela, Y. Wang, C. A. Brewer, F. Pedaci, W. Chao, E. H. Anderson, Y. Liu, K. A. Goldberg, P. P. Naulleau, P. W. Wachulak, M. C. Marconi, D. T. Attwood, J. J. Rocca, and C. S. Menoni, "Inspection 13.2-nm table-top full-field microscope," in *Alternative Lithographic Technologies*, (Proc. SPIE, 2009), 72713F.

30. H. H. Solak, "Nanolithography with coherent extreme ultraviolet light " J. Phys. D: Appl. Phys. **39**, R171-R188 (2006).

31. P. W. Wachulak, M. C. Marconi, R. A. Bartels, C. S. Menoni, and J. J. Rocca, "Volume extreme ultraviolet nano-holographic imaging with numerical optical sectioning," Opt. Express **15**, 10622-10628 (2007).

32. P. Wachulak, M. Capeluto, C. Menoni, J. Rocca, and M. Marconi, "Nanopatterning in a compact setup using table top extreme ultraviolet lasers," Opto-Electronics Review **16**, 444-450 (2008).

33. P. W. Wachulak, M. C. Marconi, R. A. Bartels, C. S. Menoni, and J. J. Rocca, "Soft x-ray laser holography with wavelength resolution," J. Opt. Soc. Am. B **25**, 1811-1814 (2008).

34. R. A. Bartels, A. Paul, H. Green, H. C. Kapteyn, M. M. Murnane, S. Backus, I. P. Christov, Y. Liu, D. Attwood, and C. Jacobsen, "Generation of Spatially Coherent Light at Extreme Ultraviolet Wavelengths," Science **297**, 376-378 (2002).

35. D. L. Matthews, P. L. Hagelstein, M. D. Rosen, M. J. Eckart, N. M. Ceglio, A. U. Hazi, H. Medecki, B. J. MacGowan, J. E. Trebes, B. L. Whitten, E. M. Campbell, C. W. Hatcher, A. M. Hawryluk, R. L. Kauffman, L. D. Pleasance, G. Rambach, J. H. Scofield, G. Stone, and T. A. Weaver, "Demonstration of a Soft X-Ray Amplifier," Physical Review Letters **54**, 110 (1985).

36. B. J. MacGowan, S. Maxon, P. L. Hagelstein, C. J. Keane, R. A. London, D. L. Matthews, M. D. Rosen, J. H. Scofield, and D. A. Whelan, "Demonstration of soft x-ray amplification in nickel-like ions," Physical Review Letters **59**, 2157 (1987).

37. R. C. Elton, *X-ray lasers* (Academic Press Inc., San Diego, CA (USA), 1990).

38. W. T. Silfvast, J. J. Macklin, and O. R. W. Ii, "High-gain inner-shell photoionization laser in Cd vapor pumped by soft-x-ray radiation from a laser-produced plasma source," Opt. Lett. **8**, 551-553 (1983).

39. H. C. Kapteyn, R. W. Lee, and R. W. Falcone, "Observation of a Short-Wavelength Laser Pumped by Auger Decay," Physical Review Letters **57**, 2939 (1986).

40. W. T. Silfvast and O. R. Wood Ii, "Photoionization lasers pumped by broadband soft-x-ray flux from laser-produced plasmas," J. Opt. Soc. Am. B **4**, 609-618 (1987).

41. H. C. Kapteyn and R. W. Falcone, "Auger-pumped short-wavelength lasers in xenon and krypton," Physical Review A **37**, 2033 (1988).

42. S. Suckewer, C. H. Skinner, H. Milchberg, C. Keane, and D. Voorhees, "Amplification of stimulated soft x-ray emission in a confined plasma column," Physical Review Letters **55**, 1753 (1985).

43. Y. Nagata, K. Midorikawa, S. Kubodera, M. Obara, H. Tashiro, and K. Toyoda, "Soft-x-ray amplification of the Lyman- alpha transition by optical-field-induced ionization," Physical Review Letters **71**, 3774 (1993).

44. D. V. Korobkin, C. H. Nam, S. Suckewer, and A. Goltsov, "Demonstration of Soft X-Ray Lasing to Ground State in Li III," Physical Review Letters **77**, 5206 (1996).

45. W. B. Bridges, "Laser Oscillation In Singly Ionized Argon In The Visible Spectrum," Applied Physics Letters **4**, 128-130 (1964).

46. A. G. Molchanov, "Lasers In the Vacuum Ultraviolet and In the X-Ray Regions of the Spectrum," Sov. Phys. Usp. **15**, 124 (1972).

47. R. Smith, G. J. Tallents, J. Zhang, G. Eker, S. McCabe, G. J. Pert, and E. Wolfrum, "Saturation behavior of two x-ray lasing transitions in Ni-like Dy," Physical Review A **59**, R47 (1999).

48. J. Nilsen, B. J. MacGowan, L. B. Da Silva, and J. C. Moreno, "Prepulse technique for producing low-Z Ne-like x-ray lasers," Physical Review A **48**, 4682 (1993).

49. Y. Li, G. Pretzler, and E. E. Fill, "Ne-like ion lasers in the extreme ultraviolet region," Physical Review A **52**, R3433 (1995).

50. J. Nilsen and J. C. Moreno, "Nearly Monochromatic Lasing at 182 A in Neonlike Selenium," Physical Review Letters **74**, 3376 (1995).

51. P. V. Nickles, V. N. Shlyaptsev, M. Kalachnikov, M. Schnürer, I. Will, and W. Sandner, "Short Pulse X-Ray Laser at 32.6 nm Based on Transient Gain in Ne-like Titanium," Physical Review Letters **78**, 2748 (1997).

52. J. Dunn, A. L. Osterheld, R. Shepherd, W. E. White, V. N. Shlyaptsev, and R. E. Stewart, "Demonstration of X-Ray Amplification in Transient Gain Nickel-like Palladium Scheme," Physical Review Letters **80**, 2825 (1998).

53. Y. V. Afanas'ev and V. N. Shlyaptsev, "Formation of a population inversion of transitions in Ne-like ions in steady-state and transient plasmas " Soviet Journal of Quantum Electronics **19**, 1606 (1989).

54. M. P. Kalachnikov, P. V. Nickles, Schn, uuml, M. rer, W. Sandner, V. N. Shlyaptsev, C. Danson, D. Neely, E. Wolfrum, J. Zhang, A. Behjat, A. Demir, G. J. Tallents, P. J. Warwick, and C. L. S. Lewis, "Saturated operation of a transient collisional x-ray laser," Physical Review A **57**, 4778 (1998).

55. P. J. Warwick, C. L. S. Lewis, M. P. Kalachnikov, P. V. Nickles, M. Schnürer, A. Behjat, A. Demir, G. J. Tallents, D. Neely, E. Wolfrum, J. Zhang, and G. J. Pert, "Observation of high transient gain in the germanium x-ray laser at 19.6 nm," J. Opt. Soc. Am. B **15**, 1808-1814 (1998).

56. J. Dunn, Y. Li, A. L. Osterheld, J. Nilsen, J. R. Hunter, and V. N. Shlyaptsev, "Gain Saturation Regime for Laser-Driven Tabletop, Transient Ni-Like Ion X-Ray Lasers," Physical Review Letters **84**, 4834–4837 (2000).

57. V. N. Shlyaptsev, J. Dunn, S. Moon, R. Smith, R. Keenan, J. Nilsen, K. B. Fournier, J. Kuba, A. L. Osterheld, J. J. G. Rocca, B. M. Luther, Y. Wang, and M.

C. Marconi, "Numerical studies of transient and capillary x-ray lasers and their applications," in *Soft X-Ray Lasers and Applications V*, (SPIE, 2003), 221-228.

58. V. L. Ginzburg, "Propagation of Electromagnetic Waves in Plasma," Addison–Wesley, Reading (1964).

59. R. Keenan, J. Dunn, V. N. Shlyaptsev, R. F. Smith, P. K. Patel, and D. F. Price, "Efficient pumping schemes for high average brightness collisional x-ray lasers," in *Soft X-Ray Lasers and Applications V*, (SPIE, 2003), 213-220.

60. D. Alessi, B. Luther, Y. Wang, M. Larotonda, M. Berrill, and J. Rocca, "High repetition rate operation of saturated tabletop soft x-ray lasers in transitions of neon-like ions near 30 nm," Opt. Express **13**, 2093-2098 (2005).

61. Y. Wang, M. A. Larotonda, B. M. Luther, D. Alessi, M. Berrill, V. N. Shlyaptsev, and J. J. Rocca, "Demonstration of saturated high repetition rate tabletop soft x-ray lasers at wavelength down to 13.9 nm," Physical Review A **72**, 053807 (2005).

62. J. J. Rocca, Y. Wang, M. A. Larotonda, B. M. Luther, M. Berrill, and D. Alessi, "Saturated 13.2 nm high repetition rate laser in Nickel-like Cd," Optics Letters **30**, 2581-2583 (2005).

63. D. Alessi, D. H. Martz, Y. Wang, M. Berrill, B. M. Luther, and J. J. Rocca, "Gain-saturated 10.9 nm tabletop laser operating at 1 Hz repetition rate," Optics Letters **35**, 414-416 (2010).

64. D. H. Martz, D. Alessi, B. M. Luther, Y. Wang, D. Kemp, M. Berrill, and J. J. Rocca, "High-energy 13.9 nm table-top soft-x-ray laser at 2.5 Hz repetition rate excited by a slab-pumped Ti:sapphire laser," Opt. Lett. **35**, 1632-1634 (2010).

65. P. Zeitoun, G. Faivre, S. Sebban, T. Mocek, A. Hallou, M. Fajardo, D. Aubert, P. Balcou, F. Burgy, D. Douillet, S. Kazamias, G. de Lacheze-Murel, T. Lefrou, S. le Pape, P. Mercere, H. Merdji, A. S. Morlens, J. P. Rousseau, and C. Valentin, "A high-intensity highly coherent soft X-ray femtosecond laser seeded by a high harmonic beam," Nature **431**, 426-429 (2004).

66. Y. Wang, E. Granados, M. A. Larotonda, M. Berrill, B. M. Luther, D. Patel, C. S. Menoni, and J. J. Rocca, "High-Brightness Injection-Seeded Soft-X-Ray-Laser Amplifier Using a Solid Target," Physical Review Letters **97**, 123901 (2006).

67. Y. Wang, E. Granados, F. Pedaci, D. Alessi, B. Luther, M. Berrill, and J. J. Rocca, "Phase-coherent, injection-seeded, table-top soft-X-ray lasers at 18.9 nm and 13.9 nm," Nature Photonics **2**, 94-98 (2008).

68. F. Pedaci, Y. Wang, M. Berrill, B. Luther, E. Granados, and J. J. Rocca, "Highly coherent injection-seeded 13.2 nm tabletop soft x-ray laser," Opt. Lett. **33**, 491-493 (2008).

69. T. H. Maiman, "Stimulated Optical Radiation in Ruby," Nature **187**, 493-494 (1960).

70. F. J. McClung and R. W. Hellwarth, "Giant Optical Pulsations from Ruby," Journal of Applied Physics **33**, 828-829 (1962).

71. L. E. Hargrove, R. L. Fork, and M. A. Pollack, "Locking of HeNe Laser Modes Induced by Synchronous Intracavity Modulation," Applied Physics Letters **5**, 4-5 (1964).

72. D. E. Spence, P. N. Kean, and W. Sibbett, "60-fsec pulse generation from a self-mode-locked Ti:sapphire laser," Opt. Lett. **16**, 42-44 (1991).

73. M. D. Perry, D. Pennington, B. C. Stuart, G. Tietbohl, J. A. Britten, C. Brown, S. Herman, B. Golick, M. Kartz, J. Miller, H. T. Powell, M. Vergino, and V. Yanovsky, "Petawatt laser pulses," Optics Letters **24**, 160-162 (1999).

74. C. K. Rhodes, "Multiphoton Ionization of Atoms," Science **229**, 1345-1351 (1985).

75. "High-Energy Density Physics with Subpicosecond Laser Pulses," OSA Technical Digest Series (Optical Society of America, Washington, D.C.) **17**(1989).

76. A. Endoh, M. Watanabe, N. Sarukura, and S. Watanabe, "Multiterawatt subpicosecond KrF laser," Opt. Lett. **14**, 353-355 (1989).

77. P. Maine, D. Strickland, P. Bado, M. Pessot, and G. Mourou, "Generation of ultrahigh peak power pulses by chirped pulse amplification," Quantum Electronics, IEEE Journal of **24**, 398-403 (1988).

78. D. Strickland and G. Mourou, "Compression of amplified chirped optical pulses," Optics Communications **55**, 219-221 (1985).

79. O. Martinez, "3000 times grating compressor with positive group velocity dispersion: Application to fiber compensation in 1.3-1.6 μm region," Quantum Electronics, IEEE Journal of **23**, 59-64 (1987).

80. O. Martinez, "Design of high-power ultrashort pulse amplifiers by expansion and recompression," Quantum Electronics, IEEE Journal of **23**, 1385-1387 (1987).

81. M. Ferray, L. A. Lompre, O. Gobert, A. L'Huillier, G. Mainfray, C. Manus, A. Sanchez, and A. S. Gomes, "Multiterawatt picosecond Nd-glass laser system at 1053 nm," Optics Communications **75**, 278-282 (1990).

82. D. Normand, M. Ferray, L. A. Lompré, O. Gobert, A. L?Huillier, and G. Mainfray, "Focused laser intensity measurement at 1018 W/cm2 and 1053 nm," Opt. Lett. **15**, 1400-1402 (1990).

83. F. G. Patterson, R. Gonzales, and M. D. Perry, "Compact 10-TW, 800-fs Nd:glass laser," Opt. Lett. **16**, 1107-1109 (1991).

84. C. Sauteret, D. Husson, G. Thiell, S. Seznec, S. Gary, A. Migus, and G. Mourou, "Generation of 20-TW pulses of picosecond duration using chirped-pulse amplification in a Nd:glass power chain," Opt. Lett. **16**, 238-240 (1991).

85. P. F. Moulton, MIT Lincoln Laboratory Report No. 1982:3 (1982).

86. P. F. Moulton, "Spectroscopic and laser characteristics of Ti:Al2O3," J. Opt. Soc. Am. B **3**, 125-133 (1986).

87. S. Backus, C. G. Durfee Iii, M. M. Murnane, and H. C. Kapteyn, "High power ultrafast lasers," Review of Scientific Instruments **69**, 1207-1223 (1998).

88. A. Sullivan, H. Hamster, H. C. Kapteyn, S. Gordon, W. White, H. Nathel, R. J. Blair, and R. W. Falcone, "Multiterawatt, 100-fs laser," Opt. Lett. **16**, 1406-1408 (1991).

89. W. G. Erhard, D. Todd, M. Mikael, D. Skyler, G. Dan, H. Watson, R. H. Greg, E. Alvin, A. C. John, J. Igor, E. Chris, and M. William, "Design of the Texas Petawatt Laser," in *Conference on Lasers and Electro-Optics/Quantum Electronics and Laser Science and Photonic Applications Systems Technologies*, Technical Digest (CD) (Optical Society of America, 2005), JFB2.

90. E. B. Treacy, "Optical Pulse Compression With Diffraction Gratings," IEEE Journal of Quantum Electronics **5**, 454 (1969).

91. (Crystal Systems, 2010), retrieved http://www.crystalsystems.com/.

92. R. L. Fork, C. H. B. Cruz, P. C. Becker, and C. V. Shank, "Compression of optical pulses to six femtoseconds by using cubic phase compensation," Opt. Lett. **12**, 483-485 (1987).

93. J. L. A. Chilla and O. E. Martinez, "Spatial-temporal analysis of the self-mode-locked Ti: sapphire laser," J. Opt. Soc. Am. B **10**, 638-643 (1993).

94. H.-K. Nienhuys, "Stretcher and Compressor Diagrams."

95. M. D. Perry, R. D. Boyd, J. A. Britten, D. Decker, B. W. Shore, C. Shannon, and E. Shults, "High-efficiency multilayer dielectric diffraction gratings," Optics Letters **20**, 940 (1995).

96. S. Backus, J. Peatross, C. P. Huang, M. M. Murnane, and H. C. Kapteyn, "Ti:sapphire amplifier producing millijoule-level, 21-fs pulses at 1 kHz," Opt. Lett. **20**, 2000-2002 (1995).

97. F. G. Patterson, J. Bonlie, D. Price, and B. White, "Suppression of parasitic lasing in large-aperture Ti:sapphire laser amplifiers," Opt. Lett. **24**, 963-965 (1999).

CHAPTER 2

FUNDAMENTALS OF SLAB LASERS

2.1 Advantages of the Zig-Zag Slab Geometry

The advantages of using a slab geometry versus the more common rod configuration are related to the possibility of generating good quality optical beams at higher average powers. The operation of laser mediums at high average power involves optically pumping the medium at an increased repetition rate, which increases thermal gradients in the gain material. As is discussed below, once the rod diameter becomes large, the thermal gradients that develop between the center of the rod and the outer surface begin to severely distort the phase-front of the beam and it is then desirable to explore alternate geometries that reduce this problem such as the rectangular slab.

As a result of non-radiative transitions in the gain material there is inherent heating of the laser medium when optically pumped therefore cooling with either a liquid or gas must be provided. Due to the poor thermal conductivity of glass, large thermal gradients develop between the cooled outer surface and the axial region of the laser medium. This in turn causes the inner area to feel compression creating tension on the outer surface.

2.1.1 The Rod Geometry

There have been numerous studies on the thermal properties of the rod geometry and its disadvantages when operating under conditions that thermally load the laser host medium to the point where it exhibits severe optical distortions [1-4]. When high-energy operation is required, the rod's area has to be sufficiently large which consequently increases the overall temperature difference between the center and the outer surface. These temperature gradients cause thermal focusing, stress induced biaxial focusing, and stress induced birefringence [1-4].

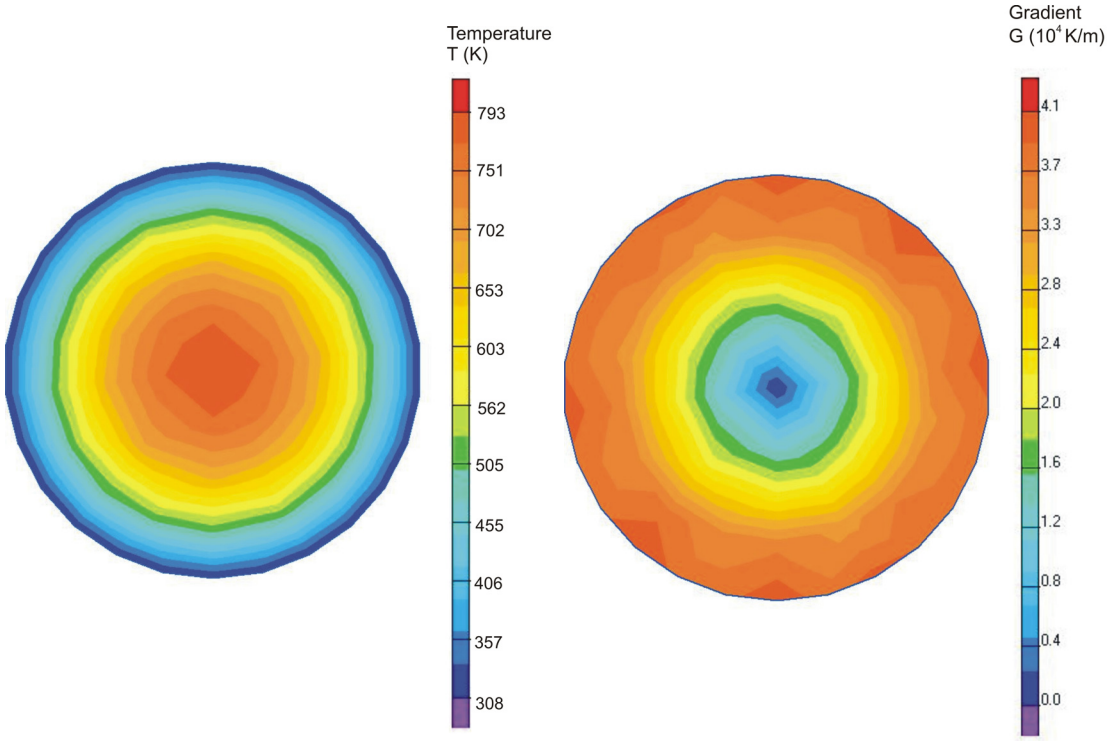

Figure 2.1 – Computed temperature distribution and temperature gradient for 1250 W input power for a 14 cm^2 Nd:Glass Rod 40 cm long

An example of a thermally loaded rod amplifier is presented in Figure 2.1. The host material is loaded with 1250 W and the cooled outer surface is kept at 308 K. Thermally induced effects can severely degrade the optical quality of the phase-front of the laser

beam which eventually limits the laser output power [5]. For the rod geometry, the radial change in index has been shown to be:

$$n(r) = n_o + \Delta n(r)_\tau + \Delta n(r)_\in \quad (1)$$

The variations in the index of refraction of the material can be represented separately by temperature ($\Delta n(r)_\tau$) and stress ($\Delta n(r)_\in$) induced changes [3]. Because of the amorphous properties of glass, the $\Delta n(r)_\in$'s contribution will be neglected for this simple analysis. Focusing on the temperature effects, it has been shown [3] that the change in index caused by heating can be expressed as:

$$\Delta n(r)_\tau = c * r^2 / r_o{}^2 \quad (2)$$

where r_o is the radius of the rod and

$$c = -(\eta P_{in} / 4K\pi L)(\delta n / \delta T) \quad (3)$$

where η is the percentage of average power absorbed (assuming it is constant), K is the thermal conductivity, T is the temperature and L is the length of the rod [3]. As the area of the rod increases the temperature difference in the medium increases, which adds more distortion to the phase-front of the beam since there is a greater difference in optical path length. This difference in optical path length arises because the beam travels down the medium axially, thus causing the inner ray to experience a hotter part of the material that effectively causes a longer path length than the cooler outside area. Along with the stress induced aberrations, the thermally induced phase-front distortions will drop the efficiency of the amplifier and limit the output power [1]. Also, depolarization can occur because of the thermally stressed host medium due to the location of the diverse thermal areas [6]. This is not acceptable if the beam is passively controlled by the rotation of polarization

between passes, or optically switched by a Pockel's cell. Besides phase-front distortion and stress induced birefringence, the most severe optical effect that happens in the rod geometry is thermal lensing because of the risk of burning the gain medium.

As the repetition rate is increased, the index gradients become large such that focusing effects start to be more important. From the index gradient relation above, it can be seen that as heating is increased the index gradient also increases towards the outside which causes the focus to become tighter until it is inside the medium which can burn and destroy the amplifier [3]. The thermal lens generated by the temperature profile in Figure 2.1 can be approximated with a parabolic fit. Given the index of refraction profile (Figure 2.2), Hecht gives an expression to find the focal length [7]:

$$n(r) = n_{\max} - (\sqrt{r^2 + f^2} - f)/d \qquad (4)$$

where $n_{\max}$ is the maximum index of refraction (1.538), d is the length of the rod (40 cm), r is the radius of the rod and f is the effective focal length.

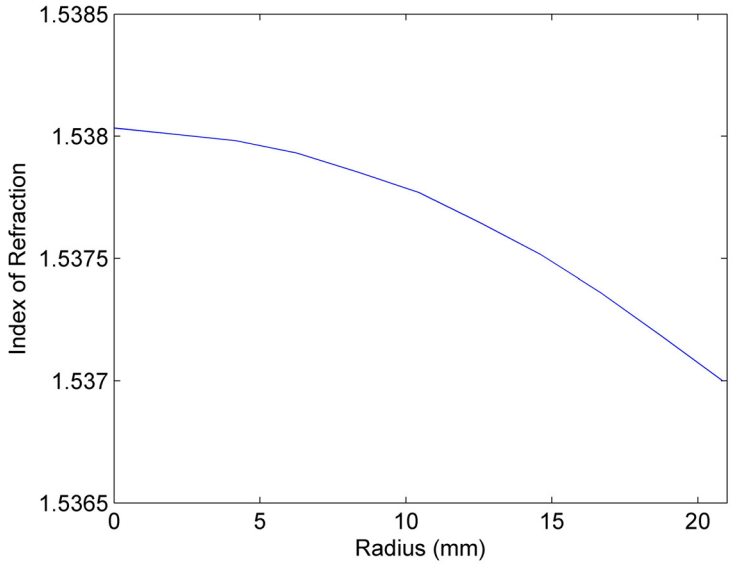

Figure 2.2 – Index of refraction along the radius of a laser rod as a result of the thermal loading given in Figure 2.1

The resulting focal point can be found at 52 cm from the end of the rod (92 cm from the beginning of the rod). Because this expression is an approximation assuming the focal length is much longer than the rod, ray tracing was employed using another parabolic fit given by Siegman [8]. Shown is Figure 2.3 is the resulting focal distance of 45 cm from the end of the rod (85 cm total). This result agrees with the approximation above and confirms the lensing is severe. To avoid this phenomenon, it is desired to ensure the beam traversing through the medium will not see uniform thermal gradients as to keep the effective path lengths equal to avoid focusing effects, and that the beam will traverse along a path that will see many different areas with varying stresses as to average the phase-front distortions as evenly as possible.

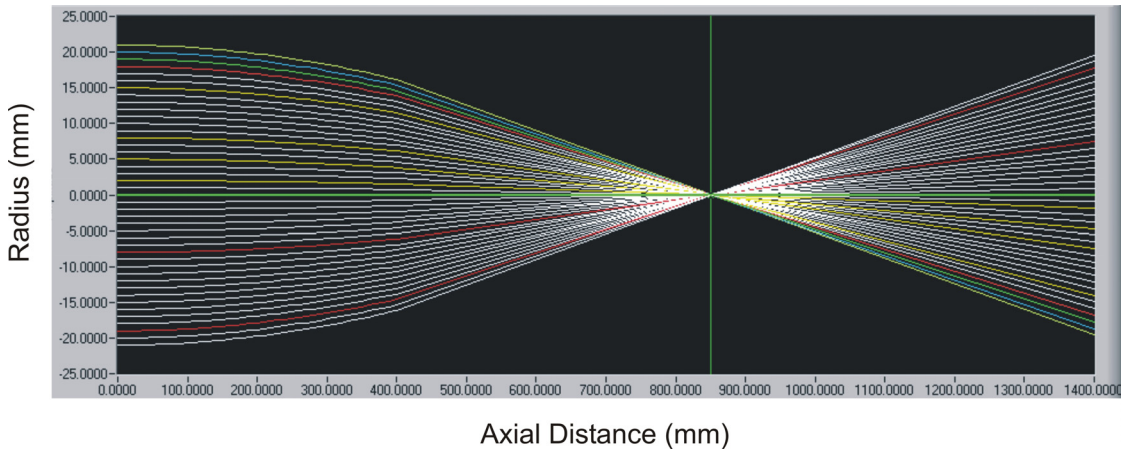

Figure 2.3 – Thermal lensing ray tracing through 400 mm of a Nd:Glass rod with the 1250 W of thermal loading, showing a focus at 850 mm (450 mm after the end of the rod)

2.1.2 The Slab Geometry

In 1969, Martin and Chernoch, while working for General Electric, proposed using a slab geometry to eliminate stress induced biaxial focusing and birefringence, which they patented in 1972 [6]. Shown in Figure 2.4 is the calculated temperature

distribution (equations 5-8) in thermally loaded slab under the same pumping conditions as Figure 2.1, cooling to a constant temperature on the pump faces to 308 ^{o}K or 35 ^{o}C.

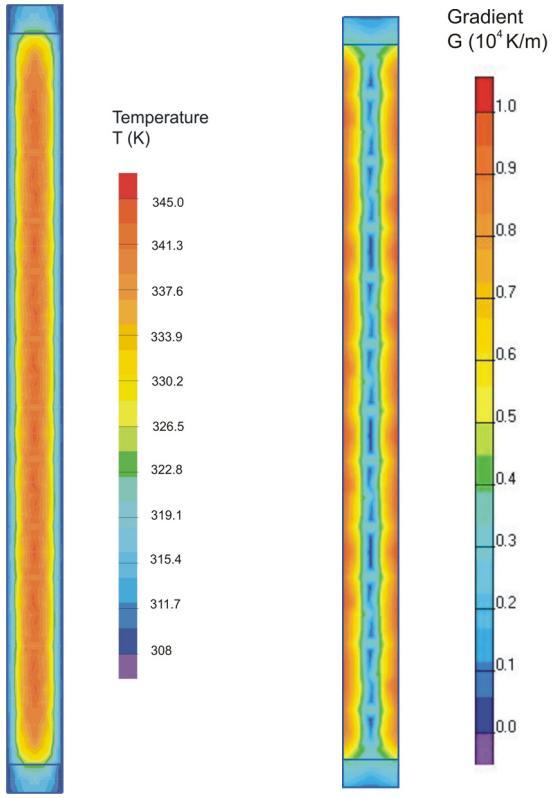

Figure 2.4 – Computed temperature distribution and temperature gradient for 1250 W input power for a 14 cm^2 Nd:Glass slab 40 cm long.

As seen from comparison of Figures 2.1 and 2.4, pumping a slab geometry with the same cross-sectional area under the same conditions, the overall temperature change dropped from 485 ^{o}C in the rod (past the glass' transformation temperature) to close to 38 ^{o}C in the slab. If the beam passes through the center of the slab (Figure 2.5), because of the relatively thin geometry, it sees a smaller overall difference in temperature than in the rod geometry.

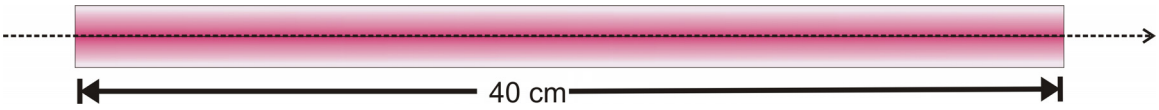

Figure 2.5 – Propagation straight through the Nd:Glass slab

This prevents large differences in effective optical path length thereby keeping the phase-front stable and allowing for harder pumping of the material. But just as the index gradients in the rod can cause spherical focusing, the gradients in the slab can cause cylindrical focusing. To understand the focusing effects that occur as the beam propagates straight through a slab geometry (Figure 2.5) it is necessary to again look at the expression that describes the change in index of refraction. We will consider both an index change due to temperature variation in the medium as well as modification from stress in the material caused by the temperature gradient. Using Jones matrices to keep track of both polarization modification and phase-front distortion it can be shown that the index of refraction will now be a tensor sub-matrix [9, 10]. For the case of an infinite slab geometry (Figure 2.6) with the beam traversing along the z-axis and cooling is done on the x-z planes (pump faces) it can be seen from Figure 2.4 the temperature variation becomes a 1D problem in the y direction. The analysis describing both temperature and stress variation given in [5] is shown below.

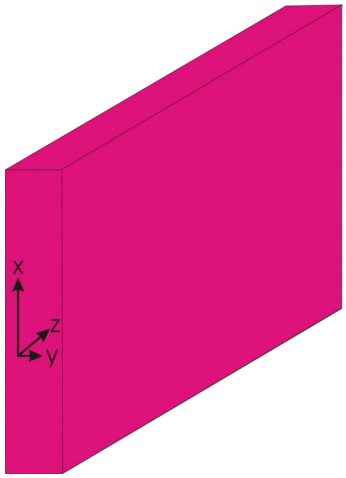

Figure 2.6 – Schematic of the slab geometry with front face axis x, y and direction of propagation z.

The thermal boundary conditions are given by:

$$\frac{\partial^2 T}{\partial y^2} = -\frac{Q}{k} \tag{5}$$

and

$$\left.\frac{\partial T}{\partial y}\right|_{y=\pm\frac{t}{2}} = \frac{\lambda}{k}\left(T_c - T\left(y = \pm\frac{t}{2}\right)\right) \tag{6}$$

where Q is the thermal loading of the material (W/cm^3), k is the thermal conductivity ($W/(cm*K)$), λ is the surface heat transfer coefficient ($W/(cm^2*K)$), T_c is the coolant temperature (K) and t is the center thickness of the slab (cm). The solution to these equations is given by:

$$T(y) = T_a + T'(y) \tag{7}$$

where

$$T'(y) = \frac{Qt^2}{8k}\left(\frac{1}{3} - \left(\frac{y}{t}\right)^2\right) \tag{8}$$

T_a is the average temperature of the material and T'(y) describes how it varies along the y direction which is ultimately our only concern for determining the changes in index due to temperature and stress. In an isotropic medium the stress tensor contribution to the index of refraction will have two independent stress optic coefficients $\beta_\perp$ and $\beta_\parallel$. $\beta_\perp$ is the stress optic contribution in the direction perpendicular to the axis of polarization and $\beta_\parallel$ is the contribution in the direction parallel to axis of polarization. These coefficients are material dependent and describe how the index of refraction changes when stress is applied in those directions.

To determine the amount of stress that is induced in the material by a temperature gradient, a stress strain analysis needs to be performed for a given geometry. Due to

thermal expansion of the material with changes in temperature the compression, expansion and shear forces should be taken into account. Establishing a set of boundary equations to balance the forces and maintain Hooke's law can result in the solution for the stress tensors, describing stress distributed throughout the material in three dimensions. A detailed analysis is performed in [5] showing a vector differential equation with the function U that would govern the stress distribution in the material:

$$\nabla^2 U + \frac{1}{1-2\upsilon}\nabla(\nabla \bullet U) = \frac{2(1+\upsilon)}{1-2\upsilon}\alpha\nabla T \tag{9}$$

where υ is Poisson's ratio, α is the thermal expansion coefficient and T is the temperature distribution. Of course the correct boundary conditions should be selected to find a unique solution. However, this system becomes very difficult and must be solved numerically. Therefore the authors invoke a plane strain approximation to reduce the problem to two dimensions. This assumes that there is no strain in the z direction which is a valid assumption if one is analyzing a position one or two slab thicknesses away from the x-y faces and the slab is uniformly pumped along the z direction. Observably the approximation does not take into account edge effects which have been shown to add significant distortion to the beam if it is not properly mitigated as discussed in Chapter 3 [11]. An example of a typical cross-sectional stress distribution for a slab geometry is presented in Figure 2.7. Just as in the rod geometry, the internal area of the slab experiences compression and the area close to the surfaces will suffer tension. Once the governing vector differential equation has been simplified to two dimensions using the approximation discussed above, along with the proper boundary equations, a solution can be found using a common 2D method known as the Airy Stress Potential ϕ [12].

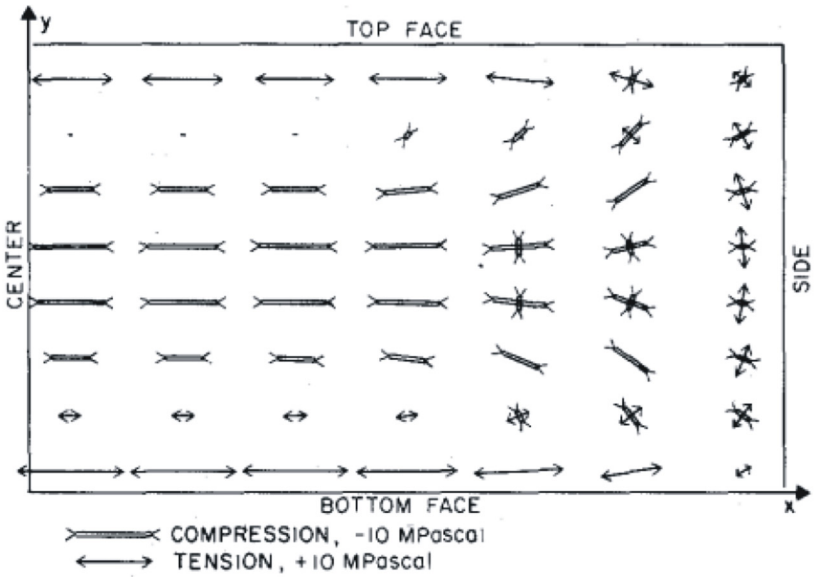

Figure 2.7 - Stress distribution for a thermally loaded slab in the x-y plane. The length of a cross-bar indicates the magnitude of the stress, and the orientation of the cross indicates the orientation of the axes of the stress tensor [11].

This method changes the problem from two coupled partial differential equations to a single fourth-order partial differential equation by relating the stress components as:

$$\sigma_{xx} = \frac{\partial^2 \phi}{\partial y^2} \tag{10}$$

$$\sigma_{yy} = \frac{\partial^2 \phi}{\partial x^2} \tag{11}$$

$$\sigma_{xy} = \frac{\partial^2 \phi}{\partial x \partial y} \tag{12}$$

giving:

$$\left(\frac{\partial^4}{\partial x^4} + 2\frac{\partial^4}{\partial x^2 \partial y^2} + \frac{\partial^4}{\partial y^4} \right) \phi(x,y) = -\frac{E\alpha}{1-\upsilon} \left(\frac{\partial^2}{\partial x^2} + \frac{\partial^2}{\partial x^2} \right) T(x,y) \tag{13}$$

where E is Young's modulus (Pa). For a slab geometry, assuming there is no temperature change in the x direction, a solution to ϕ may be found and the stress tensor solutions are then given by [5]:

$$\sigma_{xx} = \frac{E\alpha}{(1-\nu)} T'(y) = \frac{Q}{2M_s}\left(y^2 - \frac{t^2}{12}\right) \tag{14}$$

$$\sigma_{yy} = 0 \tag{15}$$

$$\sigma_{zz} = \sigma_{xx} \tag{16}$$

where M_s is the material constant defined as:

$$M_s = \frac{(1-\upsilon)k}{\alpha E} \tag{17}$$

Finally, now that we have analytical descriptions of how both the temperature and stress vary in the medium we can write the non-zero components of the index of refraction tensor describing how the phase-front of the beam will be affected in the event Jones matrices would be used [5]:

$$n_{xx} = n + \frac{\partial n}{\partial T} T'(y) + \beta_{\perp}\sigma_{zz} + \beta_{\parallel}\sigma_{xx} \tag{18}$$

$$n_{yy} = n + \frac{\partial n}{\partial T} T'(y) + \beta_{\perp}\left(\sigma_{zz} + \sigma_{xx}\right) \tag{19}$$

$$n_{zz} = n_{xx} \tag{20}$$

where all other values in the matrix are zero. If it is assumed that the beam is travelling straight through the slab the indices of refraction equations for each direction can be rearranged and written in a two term format:

$$n_x = n^o{}_x\left(1 - \frac{\alpha_x}{2} y^2\right) \tag{21}$$

$$n_y = n^o{}_y\left(1 - \frac{\alpha_y}{2} y^2\right) \tag{22}$$

where the first term is an average/constant value $n^o_{x,y}$ and the second is the index of refraction gradient parameter $\alpha_{x,y}$ describing how the index changes in the y direction. These parameters are given as [5]:

$$n^o{}_x = n + \frac{\partial n}{\partial T}\frac{Qt^2}{24k} - \frac{Qt^2}{24M_s}\left(\beta_\perp + \beta_\parallel\right) \tag{23}$$

$$n^o{}_y = n + \frac{\partial n}{\partial T}\frac{Qt^2}{24k} - \frac{Qt^2}{12M_s}\beta_\perp \tag{24}$$

and

$$\alpha_x = \frac{2}{n^o{}_x}\left(\frac{\partial n}{\partial T}\frac{Q}{2k} - \frac{Q}{2M_s}\left(\beta_\perp + \beta_\parallel\right)\right) \tag{25}$$

$$\alpha_y = \frac{2}{n^o{}_y}\left(\frac{\partial n}{\partial T}\frac{Q}{2k} - \frac{Q}{M_s}\beta_\perp\right) \tag{26}$$

It has been shown that if $\alpha_x Z^2 << 1$ and $\alpha_y Z^2 << 1$, where Z is the length of the slab, then one can use ray matrices to approximate the slab as a birefringent cylindrical lens with a propagation distance Z [13, 14]. The focal lengths in each direction are given as:

$$f_x = \frac{1}{n^o{}_x Z\alpha_x} \tag{27}$$

$$f_y = \frac{1}{n^o{}_y Z\alpha_y} \tag{28}$$

This demonstrates that within the limit of the approximation above, the focusing power f is proportional to 1/Q. Also, if $\beta_\parallel$ and $\beta_\perp$ are equal then the stress induced focusing power in both directions is equal leaving only the thermal gradient as the cause for cylindrical focusing. Furthermore unlike in a rod geometry, for incident radiation that is polarized on either the x or y axis that is sufficiently far from either edge (in the x direction), there is no stress induced depolarization. This can be visualized noticing the stresses are one

dimensional (when far enough from the edge) directed along the x-axis as can be seen in Figure 2.7.

To further improve the operation of a slab amplifier it is desirable to eliminate the cylindrical focusing effects. Conveniently the slab geometry allows for the beam to be totally internally reflected (TIR) off of the flat pump surfaces (shown in Figure 2.8), unlike the rod, thus enabling the beam to take a zig-zag optical path through the slab.

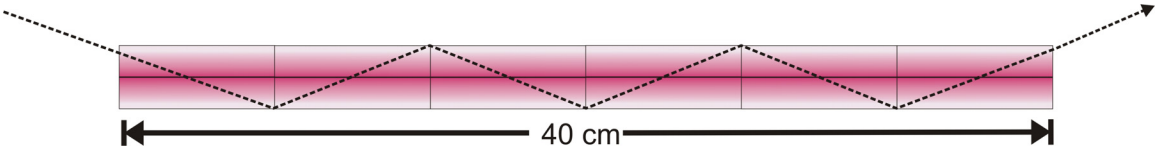

Figure 2.8 - Propagation along zig-zag path through the Nd:Glass slab

This is an advantage because it provides multiple reflections through cool and hot sections of the slab. The averaging of the optical environments traversed by all the rays eliminates first order thermal and stress induced birefringence and cylindrical focusing while averaging of aberrations picked up by propagation [5, 11]. Phase distortions acquired by the beam travelling along a zig-zag optical path through a slab amplifier can be simulated using numerical models which do not use the approximation above [11]. It has been shown in [15] that the resulting phase distortion is proportional to $L^3\alpha_y^2/N^2$ where L is the optical path length and N is the number of TIR bounces through the slab. It is then sufficient to say the averaging effects improve as more TIR bounces are performed. To ensure the benefits of the averaging effects are realized it is imperative that the pump surfaces are polished flat as possible to avoid phase-front errors on reflection. It is also important to note that temperature gradients in the vertical direction can still have an affect on the phase-front if the slab is not cooled properly. In reality the temperature of the coolant varies slightly from top to bottom as the coolant extracts heat

from the slab. This difference in temperature will create a slight difference in the index of refraction that puts a tilt on the phase-front of the beam.

It should be noted that Nd:Glass is not as good a thermal conductor as Nd:YAG and as a result, a Nd:YAG rod performs thermally 7-10 times better. However, Nd:YAG crystals cannot be made extremely large so glass is often used due to area requirements. There have been several implementations of the Nd:Glass slab amplifiers whether flash lamp pumped [16-19] or diode pumped [20-23]. Although diode pumping would be more efficient and less stressful on the glass, it is very expensive at this time and is not used in the system described in the next chapter.

2.2 Zig-Zag Beam Path Options Through a Slab

If it has been determined that a zig-zag optical path will be used, there are many different schemes that can be chosen. Shown in this section are two common options that are used. For the purposes of comparison we will assume the dimensions of the chosen Nd:Glass slab will be 14 cm x 1 cm x 40 cm corresponding to the x, y and z axis shown in Figure 2.6 respectively.

The first scheme, shown in Figure 2.9, uses input/output faces oriented at Brewster's angle from the incident radiation. This scheme will have the advantage of not requiring any optical coatings applied to the input/output faces while minimizing reflection from the interfaces.

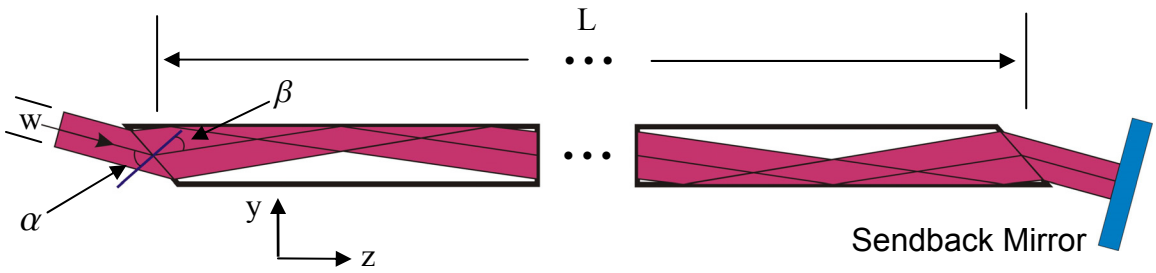

Figure 2.9 – Brewster path through a Nd:Glass slab of length L. The input beam width is w, α is the input angle with respect to the normal of the slab face and β is the refracted angle the beam takes in the glass.

For high-energy/short-pulse applications this may be an extremely attractive feature. As mentioned previously L is 40 cm and the width of the slab (in the y direction) is 1 cm. For a practical setup it is assumed that the beam inside the material will be 8 mm wide giving a 1 mm clearance on either side. The index of refraction of APG-1 (a common Nd doped laser glass) is 1.5260 at 1053 nm [24]. This will give a Brewster's angle α of 56.76 degrees with respect to the normal. Using Snell's law the refracted angle β will be 33.24 degrees. It is customary to vary the angle of the slab's input/output face to control the number of total internal reflections (TIR) that are seen by the propagating beam while ensuring it enters and leaves centered on the face without clipping the sides. It is advisable to maintain an even number of TIR bounces to ensure correct averaging of the aberrations accumulated through the slab. In a case which has been shown to provide sufficient averaging of aberrations [19] where a beam would take six TIR bounces (three on each 14 cm x 40 cm face) through a 40 cm slab, the propagation angle after entering the slab would be required to be 8.5 degrees from the z axis (left to right Figure 2.9). This defines the input/output faces to be angled at 48.42 degrees from the z axis (as opposed to 90 degrees for "flat" faces). With these angles the beam width w is required to be 6.2 mm to achieve an 8 mm beam inside the slab.

As it can be noticed from Figure 2.9 the beam path through a Brewster's angle configured slab cannot take an "opposite bounce" beam path on a returning pass if more than one pass should be made. This can be verified by calculating the exit angle with respect to the normal of the surface (using Snell's law) required by a beam traveling at -8.5 degrees with respect to the z-axis (opposite beam paths shown in Figure 2.10). This gives an angle β with respect to the normal of the interface (previous β of 33.24 + 2*8.5) of 50.24 degrees. Due to the fact that the critical angle of this material with respect to air is 40.94 degrees the resulting α from Snell's law will be imaginary and the beam would be totally internally reflected. Upon further investigation it can also be seen that varying the angle of the input/output faces to allow for a beam to exit from an opposite beam path will yield input/output angles sufficiently far from Brewster's angle resulting in back reflections that are unacceptable. Because of this restriction (depending on the beam width chosen) the beam will only extract energy from ~ 65% of the total active area that would be utilized using opposite beam paths (shown in Figure 2.10). This may or may not be a severe consequence depending on the total energy stored in the amplifying medium. Furthermore only p-polarization may be used to extract energy from the medium due to the strong S reflection at the interface. Also injection and extraction of the beam may need to be controlled by a Faraday Rotator waveplate (WP) polarizing beam-splitter (PBS) combination or a Pockels cell WP PBS combination due to overlapping beam paths. This can add complexity and cost to a system which may be undesired. Finally it should be noted that when fabricating a Brewster's slab the number of TIR bounces a beam will take becomes fixed. Therefore if one would like to change the beam path the slab faces would have to be modified or a new slab would need to be fabricated.

The second scheme described in this section is a flat faced anti-reflection (AR) coated slab. Figure 2.10 shows the same slab described above with flat faces. With this configuration the refracted angle of the input beam β (shown in Figure 2.9) becomes equal to the propagation angle with respect to the z-axis. In the case of a six TIR bounce scheme described above β = 8.5 degrees. This will give an input/output angle α of 13.04 degrees.

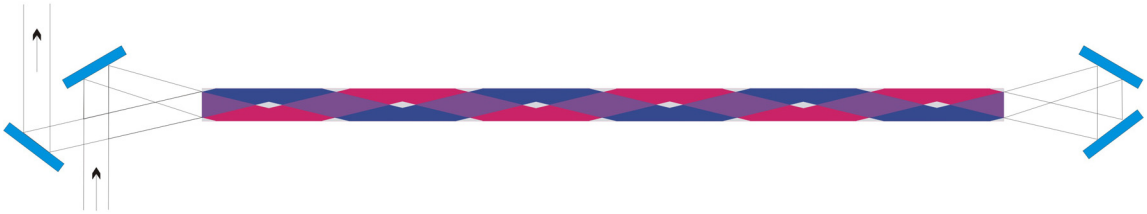

Figure 2.10 – To scale schematic of the 40 cm long six TIR bounce zig-zag optical path taken by an eight mm wide beam through the amplifying medium. The red and blue paths indicate opposite travelling beams and the purple is the region where both beams extract energy. The white sections do not see a beam pass through.

The flat faced scheme does allow for the variation of the input angle with respect to the normal to which will vary the number of TIR bounces the beam will take. This is limited by the range of angles at which the AR coating will be highly transmissive. As can be seen in Figure 2.10 opposite beam paths are shown utilizing a large percentage of the total active area (close to 100%). The red and blue shaded areas show the input and output beam paths respectively. The purple regions indicate an area where both beams extract energy and the white shows where the beam does not pass through. If this scheme is used and it is desired to simulate the amount of energy that will be extracted from the amplifier it is important to keep track of the different areas and how the gain is affected after each pass. This scheme can amplify either S or P polarization as well as allow for

opposite beam double pass extraction without the use of any other components besides mirrors.

Other schemes may be used with the slab geometry and are not discussed here [22, 23, 25, 26]. The flat surface Nd:Glass zig-zag beam path scheme was chosen when developing the amplifier discussed in later chapters. In Chapter 3 the design, characterization and implementation of a Nd:Glass slab amplifier as well as the pulse power and cooling systems that support its operation are discussed.

2.3 References

1. G. D. Baldwin and E. P. Riedel, "Measurements of Dynamic Optical Distortion in Nd-Doped Glass Laser Rods," Journal of Applied Physics **38**, 2726-2738 (1967).
2. J. D. Foster and L. M. Osterink, "Thermal Effects in a Nd:YAG Laser," Journal of Applied Physics **41**, 3656-3663 (1970).
3. W. Koechner, "Thermal Lensing in a Nd:YAG Laser Rod," Appl. Opt. **9**, 2548-2553 (1970).
4. L. M. Osterink and J. D. Foster, "Thermal Effects and Transverse Mode Control In a Nd:YAG Laser," Applied Physics Letters **12**, 128-131 (1968).
5. J. Eggleston, T. Kane, K. Kuhn, J. Unternahrer, and R. Byer, "The slab geometry laser--Part I: Theory," IEEE Journal of Quantum Electronics **20**, 289-301 (1984).
6. W. S. Martin and J. P. Chernoch, "Multiple Internal Reflection Face-Pumped Laser," U.S. Patent 3,633,126 (January 4 1972).
7. E. Hecht, *Optics* (Addison Wesley, San Francisco, CA, 2002).
8. A. E. Siegman, *Lasers* (University Science Books, Mill Valley, CA, 1986).
9. J. F. Nye, *Physical Properties of Crystals* (Oxford Clarendon, Oxford, England, 1967).
10. R. C. Jones, "A New Calculus for the Treatment of Optical Systems. IV," J. Opt. Soc. Am. **32**, 486-493 (1942).
11. T. Kane, J. Eggleston, and R. Byer, "The slab geometry laser-II: Thermal effects in a finite slab," IEEE Journal of Quantum Electronics **21**, 1195-1210 (1985).
12. H. Parker, *Thermal Elasticity* (Blaisdell, Waltham, MA, 1968).

13. A. E. Siegman, *Introduction to Lasers and Masers* (McGraw-Hill, New York, NY, 1971).

14. A. Yariv, *Introduction to Optical Electronics* (Holt, Rinehart and Winston, New York, NY, 1976).

15. J. M. Eggleston, "Theoretical and experimental studies of slab geometry lasers," Ph.D. Dissertation (Stanford University, Stanford CA, 1982).

16. J. Eggleston, G. Albrecht, R. Petr, and J. Zumdieck, "A high average power dual slab Nd:glass zigzag laser system," Quantum Electronics, IEEE Journal of **22**, 2092-2098 (1986).

17. L. A. Hackel and C. B. Dane, U.S. Patent 5 239 408 (1993).

18. J. L. Miller, L. A. Hackel, C. B. Dane, and L. E. Zapata, U.S. Patent 5 285 310 (1994).

19. C. B. Dane, L. E. Zapata, W. A. Neuman, M. A. Norton, and L. A. Hackel, "Design and operation of a 150 W near diffraction-limited laser amplifier with SBS wavefront correction," IEEE Journal of Quantum Electronics **31**, 148-163 (1995).

20. S. Basu and R. L. Byer, "40-W average power, 30-Hz moving-slab Nd:glass laser," Opt. Lett. **11**, 617-619 (1986).

21. M. K. Reed, W. J. Kozlovsky, R. L. Byer, G. L. Harnagel, and P. S. Cross, "Diode-laser-array-pumped neodymium slab oscillators," Opt. Lett. **13**, 204-206 (1988).

22. M. J. Shoup, J. H. Kelly, and D. L. Smith, "Design and testing of a large-aperture, high-gain, Brewster's angle zigzag Nd:glass slab amplifier," Applied Optics **36**, 5827-5838 (1997).

23. K. Du, N. Wu, J. Xu, J. Giesekus, P. Loosen, and R. Poprawe, "Partially end-pumped Nd:YAG slab laser with a hybrid resonator," Opt. Lett. **23**, 370-372 (1998).

24. "APG-1 Specifications Sheet, Provided by SCHOTT North America, Inc., 555 Taxter Road, Elmsford, NY 10523 USA."

25. J. E. Bernard and A. J. Alcock, "High-efficiency diode-pumped Nd:YVO4 slab laser," Opt. Lett. **18**, 968-970 (1993).

26. N. Hodgson, S. Dong, and Q. Lü, "Performance of a 2.3-kW Nd:YAG slab laser system," Opt. Lett. **18**, 1727-1729 (1993).

CHAPTER 3

AMPLIFIER DESIGN AND CHARACTERIZATION

3.1 Amplifier Design

There are many details that must be considered when designing a laser amplifier head. The requirements become even more stringent as the amplifying medium increases in overall size and as it is pumped harder. Care must be taken to mount the glass with very low stress while at the same time creating cooling channels and cavities that can provide sufficient heat removal with uniform optical pumping. Section 3.1 describes the methods used to create a zig-zag Nd:Glass slab amplifier head for the use in a multi-pass amplification scheme.

3.1.1 Physical Design of Amplifier Head

The laser amplifier head is required to hold the laser glass with minimal stress while enabling cooling and optical pumping. The design of the amplifier head developed at Colorado State University is shown in Figure 3.1. The main parts include a titanium frame, two reflector cavities, windows creating the cooling channels on either side of the slab, window braces, flow tubes and the lamps. It is required to have minimal mechanical and thermal stress on the slab in order to minimize aberrations in the beam as well as to prevent the glass from cracking when operating the amplifier at high average powers.

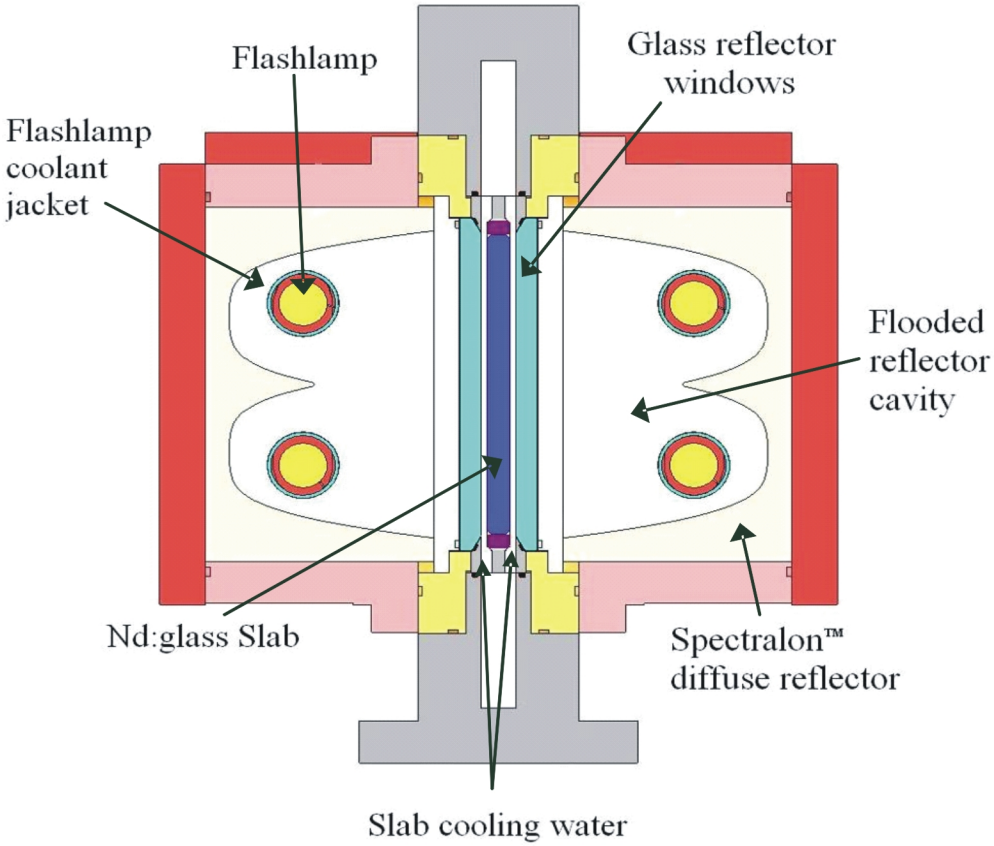

Figure 3.1 – Schematic of slab laser amplifier head illustrating positions of the laser glass, reflector cavities, cooling channels and lamps.

Uniform optical pumping and cooling of the slab is required to maintain relatively uniform temperature gradients and low stress [1-3].

3.1.1.1 Slab, Mount Method & Absorbing Glass

The laser medium is a large slab of neodymium doped advanced phosphate glass (APG-1) manufactured by Schott. APG-1 has better thermal conductivity properties than normal phosphate glass, which is very important for the high energy per pulse/high average power operation. The doping of the glass is ~ 2.7% by weight of Nd corresponding to 3-3.5 x10^{20} Nd atoms/cm^3 [3, 4].

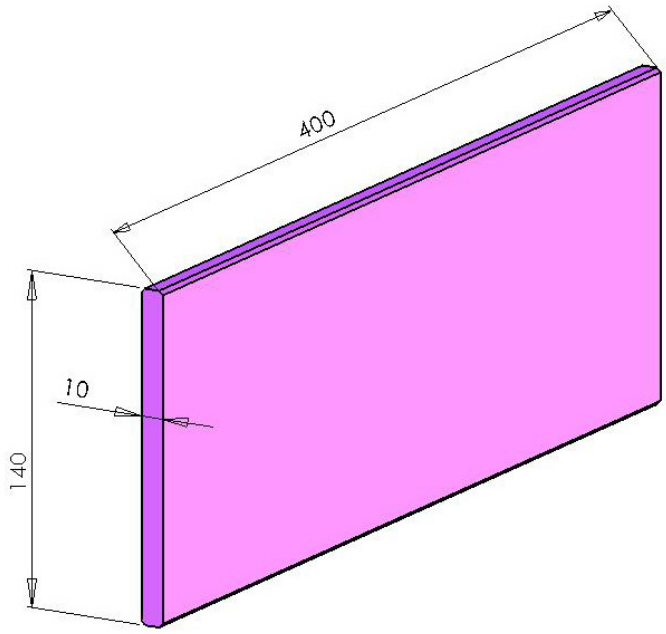

Figure 3.2 –Dimensions of the Nd:Glass slab in mm.

The slab's 1 cm x 14 cm faces (Figure 3.2) are coated with an anti-reflective (AR) coating and are tilted by 1.5 degrees with respect to the propagation axis. This helps to prevent parasitic oscillations resulting from an ASE cavity that could arise if the gain is higher than the losses. The angled faces also help to protect the pre-amplifiers from back reflections. As discussed in the previous chapter the advantage of having flat faces with an AR coating instead of Brewster's angle faces is the insensitivity to the polarization of the beam as well as the allowance of opposite beam paths resulting in higher utilization of the amplifiers bulk area. Therefore the glass slab can amplify either S or P polarization in the same fashion, unlike a Nd:YLF crystal. This advantage can be used if it is desired to passively control the path of the beam with Faraday rotators and polarizing beam splitters.

The mounting of the slab is critical to avoid mechanical stress that can damage the glass, as well as inducing birefringence and/or other problems like deformations that can

cause aberrations in the beam [3]. Titanium braces are used on the top and bottom of the slab to support it. This material, also used for the main frame, was chosen because it is resistant to corrosion in deionized water and has high strength. HA50 infrared absorbing glass, provided by Hoya Corp., is attached to the top and bottom faces of the slab to help reduce the chance of parasitic oscillations occurring due to sufficiently intense optical pumping of the gain material. SYLGARD®$_{\text{brand}}$ 184 index matching elastomer provided by Dow Corning Corp. is used to attach the absorbing glass to the slab which reduces the reflections from the face as shown in Figure 3.3. Once the titanium braces are set atop and underneath the slab the assembly is slid into the titanium frame.

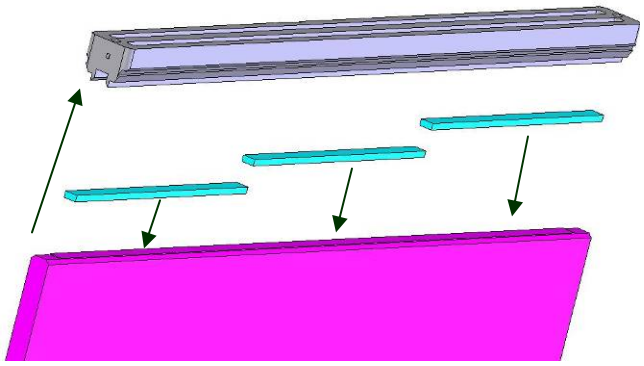

Figure 3.3 – Diagram showing how titanium braces fit on the slab. Absorption glass resides in a grove between the brace and the slab.

3.1.1.2 Reflectors and Reflector Cavity

The reflector cavities are very important for achieving uniform pumping of the slab. There have been studies performed by using ray tracing methods to estimate the type of shape that would produce the most uniform pumping in a two flash lamp cavity [2, 5]. The reflector cavity used is that computed by Miller et al. [2], shown in Figure 3.4. The reflector cavity's shape is defined by an equation of form:

$$f_o(x) = a + b * x + c * x^2 + d * x^3$$

where:

a = 9

b = -0.5

c = 0.5

d = -0.234375

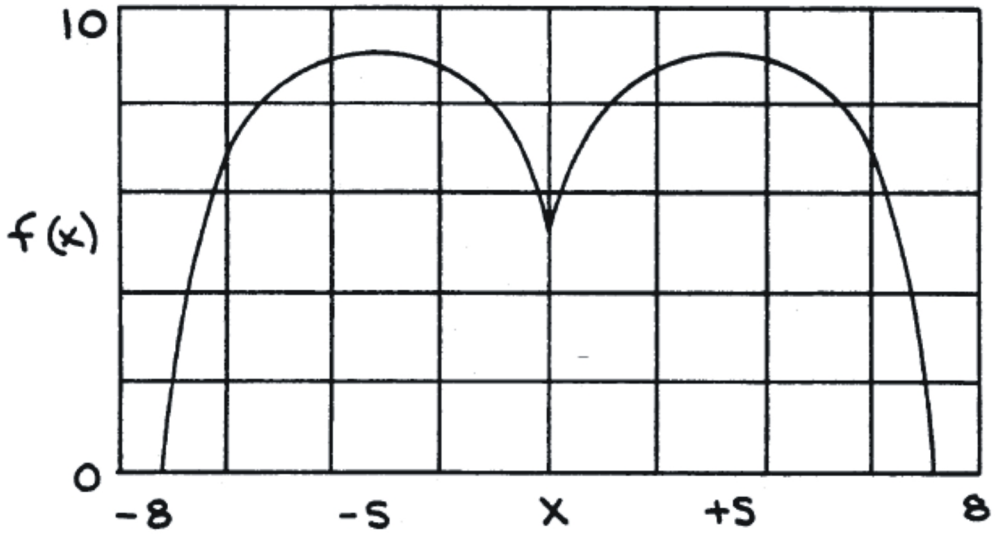

Figure 3.4 –Reflector cavity optimum shape [2].

The curves defining the reflector walls have symmetry axis where the parabola switches directions at s = ±3.2 cm, therefore the following set of equations define the curve:

$$x < -s : f(x) = f_o(-x - s)$$

$$-s < x < 0 : f(x) = f_o(x + s)$$

$$0 < x < s : f(x) = f_o(-x + s)$$

$$s < x : f(x) = f_o(x - s)$$

To obtain the constants for the cubic equation, Miller et al. iterated over many shapes until a uniform pump scheme was achieved [2]. In this geometry the lamps are located at x = ±3.8 cm, y = 5.65 cm. The reflector is machined from Spectralon^{TM}, a diffuse material which is highly reflective for light in the visible region of the spectrum and is compatible with deionized water [3].

3.1.2 Cooling and Chiller Design

Cooling considerations are imperative for the correct operation of the zig-zag slab amplifier. Because of the desired high average pump power, cooling is essential for keeping the beam quality high by ensuring the thermal gradients and stresses in the glass are minimized. As discussed in Chapter 2, the slab geometry along with a zig-zag optical path has been chosen as the optimal geometry for most efficient cooling and having the lowest distortion on the beam. Due to the slab geometry and the uniform pumping provided by the reflector cavities, one-dimensional pumping non-uniformities in the direction of propagation are averaged together along the > 40 cm zig-zag path. This leaves us to consider only the non-uniformities created along the 14 cm long axis of the slab. The thermal analysis in references [1-3] has shown that a pumping deviation of approximately 5% can induce a 1-3 λ tilt in the beam spatially in the vertical direction from a single pass. This is not acceptable if there are to be many passes through the slab. Therefore, it is very important to cool the slab well enough to minimize thermal gradients in both of the transverse directions (height and width) of the slab. To minimize the thermal gradients and keep the slab at a steady state temperature of 35 degrees Centigrade, the slab is water cooled along the large pump surfaces.

The water flow (Figure 3.5) in the amplifier first proceeds through water channels defined by the slab and a set of two glass windows that surround it (Figure 3.1). The water channels are very thin (2.5 mm) to ensure that the fluid velocity is high which is discussed further below. After the slab, the four flash lamps are then cooled in parallel. Water jackets are created by restricting the coolant in between the flow tube and the lamp.

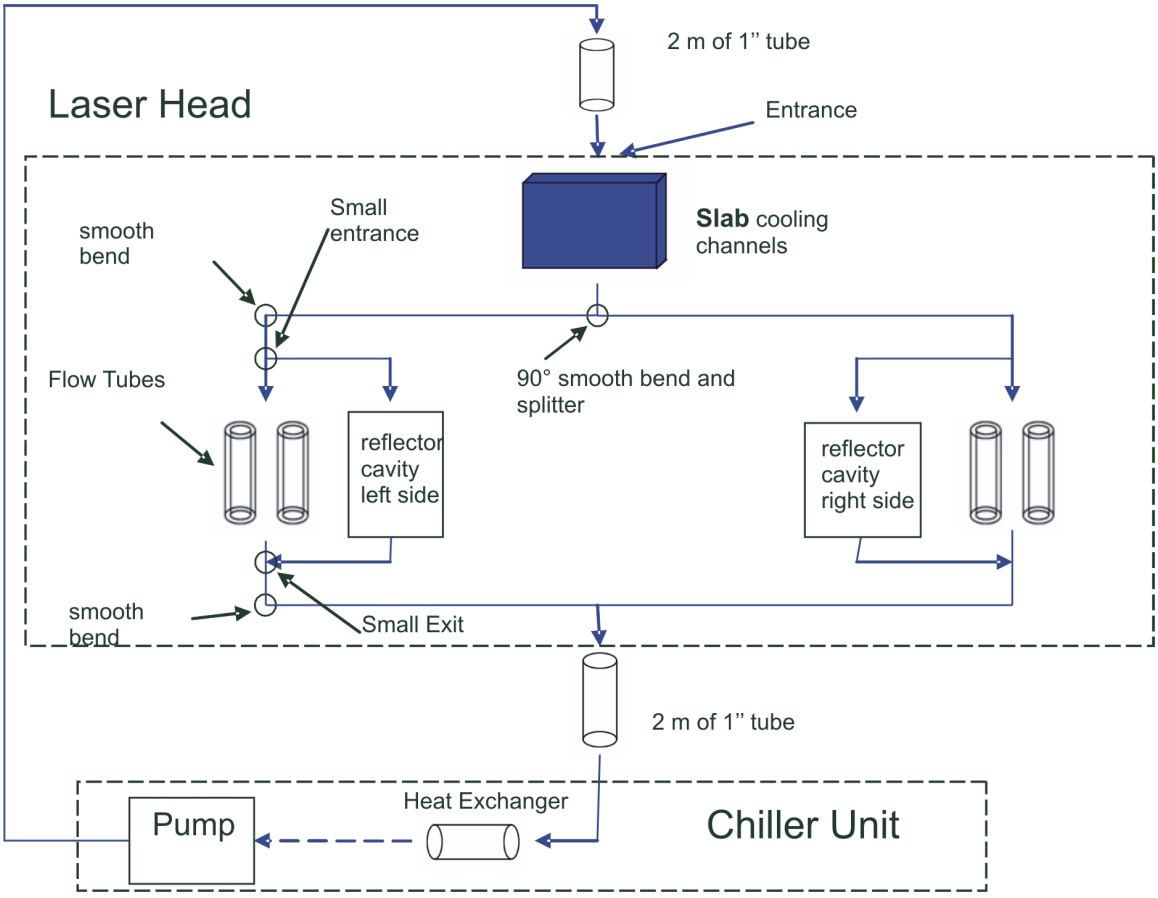

Figure 3.5 – Schematic of the amplifier's water cooling system.

The water also flows in parallel through the reflector cavities to cool the reflecting walls, but the flow required is minimal. The water then exits and returns to the chilling unit which controls the temperature. This chiller produces a flow rate of up to 180 liters per minute to ensure the dissipation of up to 15 kW of heat giving it the ability to minimize

the temperature gradients discussed. The pressure drops for all of the channels, flow tubes and hoses were calculated to determine the correct pump specifications and to ensure the slab will not see too large of a pressure differential which will minimize stress. Calculations of the pressure drops, a diagram and more detailed Reynolds number calculations are included in Appendix A. The next sections discuss the heat removal from the slab and the lamps.

3.1.2.1 Cooling Channels

It is important to minimize the gradual change in the index of refraction due to a temperature increase along the vertical direction. It has been shown that a difference of 1 ^{o}C can induce a wavefront tilt of 3 λ [1-3]. We have chosen to keep the temperature differential between the top and bottom of the slab at 0.1 ^{o}C even in the case of operation at several Hz repetition rate. The coolant mass flow rate necessary to maintain this temperature difference under steady state operation can be computed using [5]:

$$P_{in} = m_p \cdot C_p \cdot \Delta T$$

where P_{in} is the thermal power that is deposited, C_p is the specific heat of the coolant, ΔT is the temperature change in the coolant and m_p is the mass flow rate of the coolant. The specific heat for water is 4.184 J/gm ^{o}C and our desired temperature difference is 0.1 ^{o}C. With this information the mass flow rate for a specific input power is easily obtained. Because of the difficulty in calculating the exact amount of heat deposited in the slab, we have chosen a flow rate of 3 l/s which is what was used in ref. [3] to keep the temperature differential of 0.1 ^{o}C at 3 Hz while removing 1250 W of heat. More heat may be removed at higher temperature differentials**.** The percentage of pump light absorbed by the slab

that will be reemitted as heat will typically range from 0.5-0.7 [6] depending on the material and doping properties. This will translate to a typical 2%-10% of the total electrical pump power delivered to the lamps [7]. To obtain uniform cooling and high efficiency heat transfer the water must have a turbulent flow. To achieve this, the water channels need to be sufficiently small and have a sufficiently high mass flow rate. According to fluid mechanics, a water channel is typically in the turbulent regime when the Reynolds number, which is the ratio of the inertia and viscous forces, is above 2300 [5, 8]. The Reynolds number for our channel is given by:

$$\mathrm{Re} = 4 * m / \mu * P$$

where m is the mass flow rate, μ is the dynamic viscosity of the coolant and P is the wetted perimeter [5]. This equation was derived assuming a rectangular channel which is a good approximation for our waterway [5, 8]. As mentioned above and illustrated in Figures 3.1, the cooling channels are formed by placing two windows on either side of the laser glass. This forms two thin 2.5 mm channels for water to run through. Given our rectangular channel (2.5 mm x 360 mm), the dynamic viscosity for water is μ = 0.00764 gm/cm*s and our chosen mass flow rate of about 3000 gm/s (half in each channel), the calculated Reynolds number is

$$\mathrm{Re} = 4 * 1500/(0.00764 * 2*(0.25 + 36)) = 10{,}870$$

which is sufficient to define a turbulent flow.

3.1.2.2 Discussion of Stress Fracture Limit

Another design point that is crucial is the stress fracture limit. The key question is: At what temperature gradient does the glass crack? There have been thorough

investigations into this problem by many groups [1-3, 5, 9]. Most materials expand linearly as they are heated. The point at which fracture occurs is called the stress fracture limit. It is difficult to predict exactly when a piece of glass will fracture because of the inherent elastic properties that cause stretching after a certain point of heating. After this point, defects in the glass become a very important factor in determining the probability of fracture [10]. Koechner and Bass [9] give an expression to compute the maximum temperature differential that a piece of Nd:Glass can tolerate before fracturing:

$$\Delta T_{max} = 3 R_s / 2K$$

where R_s is the thermal shock parameter and K is the thermal conductivity of the glass. R_s is given by [2.15]:

$$R_s = K (1-\nu) \sigma_{max} / \alpha E$$

where ν is Poisson's ratio, α is the thermal expansion of the glass, E is Young's modulus and σ_{max} is the maximum surface stress before failure. For our glass σ_{max} is not known and should be experimentally measured. However, as discussed below semi-empirical considerations can be used to determine the safe operation of the slab. In Figure 3.6 the temperature distribution across the 14 cm x 1 cm cross sectional area of the slab is shown for a 1250 W load on the glass. The temperature change is 38 ^{o}C which has been experimentally shown to be under the stress fracture limit [3]. As the repetition rate of the amplifier is increased great care is required even though it is expected not to see a fracture up to 5 Hz. As stated above, this prediction is based on a demonstration done by Dane et al. [3] who ran a similar zig-zag slab amplifier at up to 5 Hz with 2.5 kJ/pulse of electrical energy provided to the flash lamps.

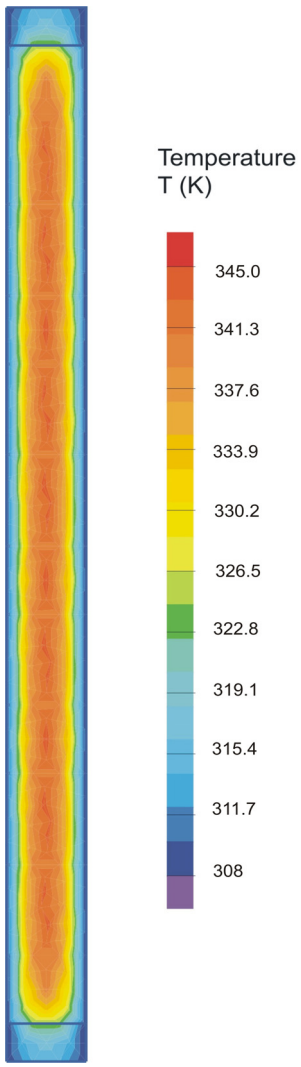

Figure 3.6 – Computed temperature distribution for 1250 W load and turbulent cooling

3.1.2.3 Flashlamp Cooling

Flow tubes surround the lamps (Figure 3.7) to provide cooling with a large Reynolds number. Cooling in this region is not as critical as in the slab region, but it is important because of the significant amount of heat produced in this area. The heat is a result from the inefficiency associated with the conversion of electrical energy to light. Heat is also generated from the flow tubes which are intentionally doped with cerium to absorb ultraviolet (UV) radiation that is emitted from the lamps. It is desirable to block

UV radiation because of its degradation effects on materials such as solarization in glass. Also, as mentioned previously, the laser transition in the slab is pumped by the visible spectrum, which implies that UV light unnecessarily adds heat to the slab.

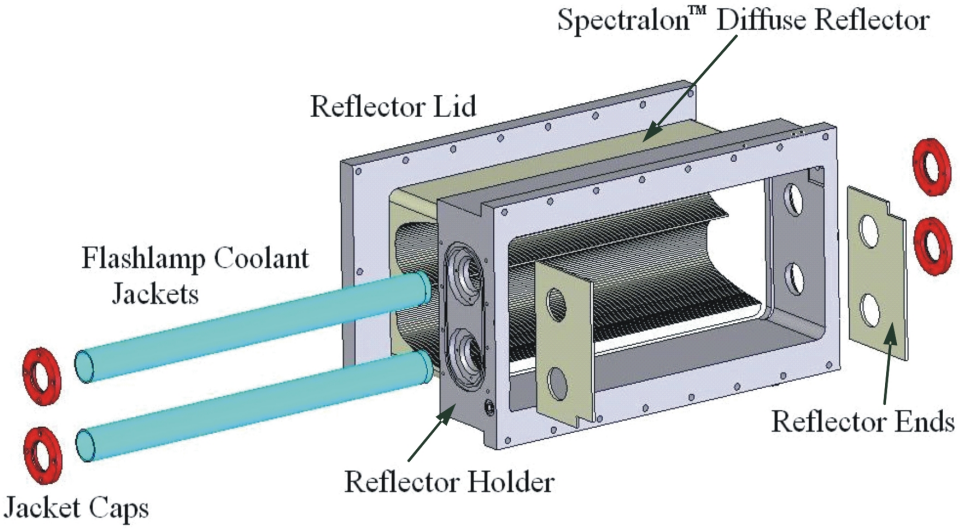

Figure 3.7 – Schematic showing the reflector cavity with reflectors, flow tubes and water seals [11].

The transmission spectrum for the flow tubes is shown in Figure 3.8 and presents a cutoff at a wavelength of about 350 nm [12].

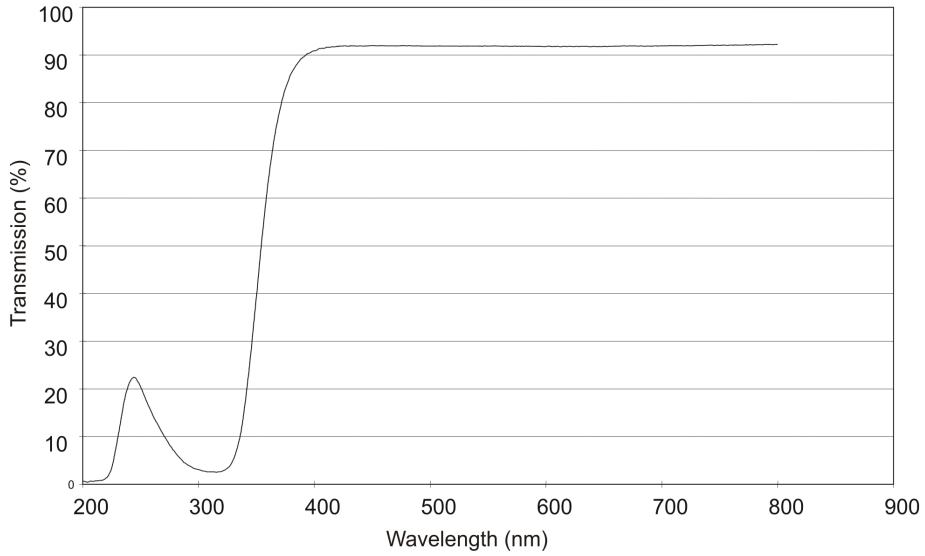

Figure 3.8 – Transmission spectrum of flow tubes [12].

The Reynolds number for the flow tube channels was calculated, in a similar fashion as above, to be 25,093. This is sufficiently high to efficiently extract the heat deposited in the flash lamps and flow tubes.

3.1.2.4 Temperature Measurements

Chiller units were designed and constructed entirely at Colorado State University to dissipate up to 15 KW and to fulfill all the specifications defined by the computations discussed above. Testing of the chilling units involved ensuring they provide an adequate flow of 3 l/s along with smooth start and stop processes as necessary to avoid any possible shock to the head and ensuring they could regulate the temperature properly. To test the cooling system an undoped slab made from float glass was mounted in the amplifier head in place of the costly Nd:Glass slab as a precaution. The flashlamps were fired at increased frequency until reaching a maximum repetition rate of 5 Hz. The temperature difference between the water at the input and output of the test slab, corresponding to the bottom and top of the slab, was monitored as a function of repetition rate for a capacitor charging voltage of 4.95 kV, corresponding to a pump energy of 2.5 kJ/pulse. The data points are presented in Figure 3.9. As can be seen, at 1-2 Hz the temperature differential stays close to 0.1 ^{o}C and remains below 0.5 ^{o}C at 5 Hz repetition rate. From this test it was determined that the cooling system met expectations. It should be noted that this will not be the same temperature difference that would result when the test slab is replaced by the doped laser glass. The strong fluorescence of the Nd:glass is likely to emit considerable radiation through the faces of the slab, reducing the

temperature increase. It has been verified that when operating the slab amplifier heads at 2.5 Hz, a temperature differential of 0.1-0.2 ^{0}C was measured.

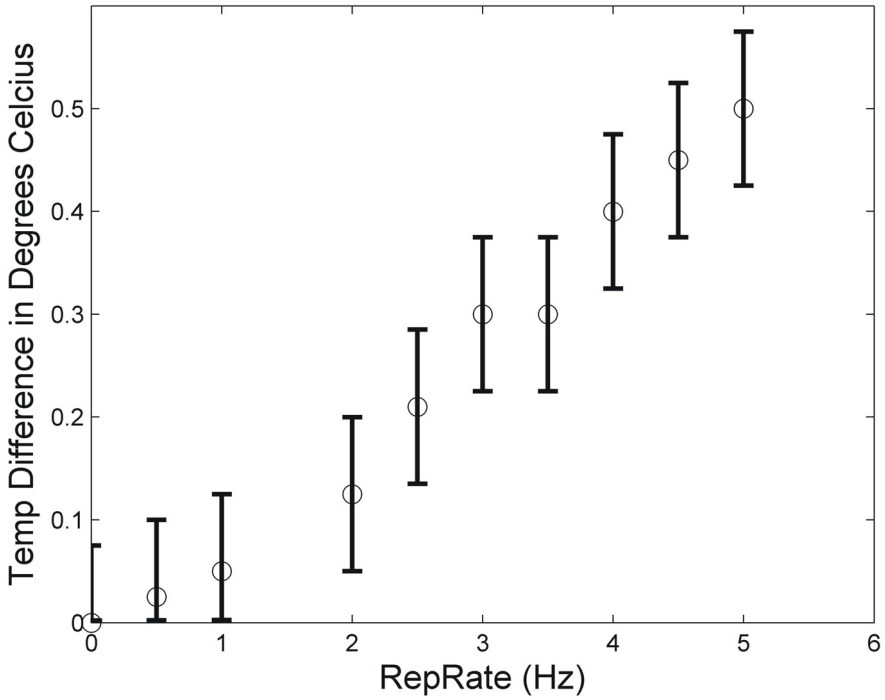

Figure 3.9 – Water temperature differential between the input and output when cooling the test transparent slab as a function of repetition rate for pump energy of 2.5 kJ per pulse.

3.2 Power System

The power system used to drive this amplifier consists of an RLC circuit which releases a 270 μs current pulse through the flashlamps. The lamp can be modeled as a time dependent resistor. A critically damped RLC circuit is used which allows for control of the pulse width and current flow through the lamps. The power requirement amounts to a maximum of 1 kJ per lamp resulting in a total of 4 kJ per pulse of electrical energy supplied to the laser head. The amplifier was designed to run at a nominal energy of ~ 2.7 kJ per shot (675 J per lamp). This level of pumping is expected to result in a single pass

gain of about 3.3x [1-3]. Two Pulse Forming Networks (PFNs) pump the four lamps of the amplifier. Each PFN contains the RLC circuit mentioned above along with support electronics which provide simmer control for two lamps in series, precision switching, and safety interlocks.

3.2.1 PFN Design and Considerations

The PFN consists of a damped RLC circuit. The main challenge here lies in the fact that the resistance of the RLC circuit is provided on great part by the plasma of the lamps and therefore is not constant. It has been shown that the resistance given by the lamp can be approximated by [13]

$$R = k_o / \sqrt{I}$$

where k_o is a constant defined by the lamp properties and I is the current through the lamp. Therefore, the voltage across that lamp is given by:

$$V = k_o * \sqrt{I}$$

It is important to have a small amount of current always flowing through the lamp (simmer current) to initiate breakdown of the gas and create an axially uniform plasma column for energy deposition. As stated above, requirements for the current pulse are to deposit a maximum of 1 kJ of energy per lamp within 270 μs. This time period is related to the lifetime of the metastable laser upper level of Nd:Glass which is about 300 μs [3, 14]. It is desirable to deliver the entire amount of pump energy before significant decay of the laser upper level occurs. To accomplish this, a critically damped or nearly critically damped pulse is required to ensure that ringing is minimized. If there is significant ringing, then it becomes difficult to keep the lamps lit after the high energy pulse is released, as discussed below. It is also not desirable to have excessive damping because

then the delivery of energy will be spread out in time which is not acceptable. Fenix Technology, a vendor of the flashlamps, offers a tool which defines capacitor and inductor pair values when given the energy of the pulse, the pulse width and the properties of the lamp. For this situation it was desired to have two lamps in series which requires the capacitor to be able to store 2 kJ of energy. The capacitor and inductor values were obtained using the tool given by Fenix for the chosen lamps and were chosen to be 145.16 μF and 55.8 μH respectively. The circuit is shown in Figure 3.10.

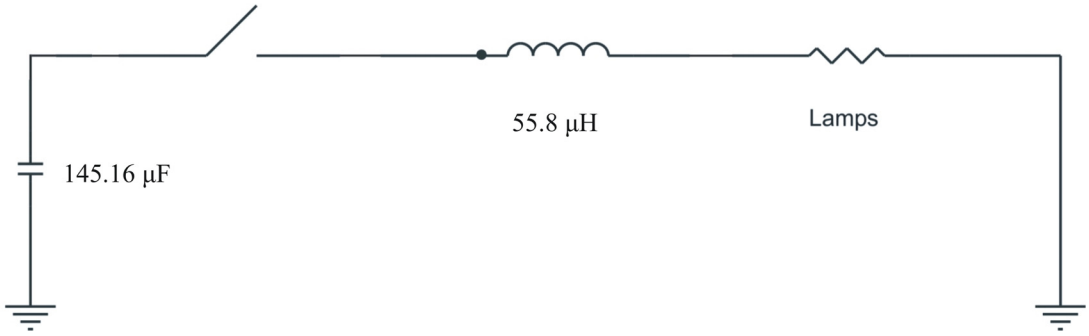

Figure 3.10 –Simplified RLC circuit diagram of the Pulse Forming Network.

The lamps used are filled with Xe gas at 170 Torr, have an internal bore of 18 mm and an arc length of 15.35 inches. This gives a total of 30.7 inches of arc length because we are running two of them in series. The k_o value given for these lamps is 22.82, or 45.64 when running two in series. If these lamps were to be run at the 1 kJ per lamp specification, the energy would still be only at 6 % of the explosion limit as defined by the vendors. This information indicates the lamps should be able to withstand hundreds of thousands of shots before needing to be changed [15]. More about the lifetime of the lamps is discussed in section 3.2.4. To reach energy of 2 kJ the capacitor needs to be charged to 5.3 kV. The circuit was simulated using p-Spice [16] approximating the lamp resistance as 1 ohm. This model showed that for the capacitance and inductance values selected the

pulse width should be about 250 μs at FWHM while the peak current should reach 4 kA. The p-Spice model was also used to simulate the charging of the capacitors (Figure 3.11), the simmer current and the resulting current pulse used to excite the lamps (Figure 3.12). The PFN system was designed to run at up to 10 Hz. This is at least double the maximum repetition rate at which the amplifier will ever be run at, but it is important to over design to prevent unexpected failures. At 10 Hz, the RMS current is close to 150 Amps, which requires a 1 AWG wire. Also, all of the components included in the system need to be able to withstand the charge voltage of 6 kV and rings of up to 12 kV. From these specifications, we can then choose the necessary "switch". Two 4 kV thyristors that can handle 1 kA of current RMS in series were selected to serve this function. These thyristors can also handle 12 – 15 kA non-repetitive surge currents which is important for a long lifetime [17]. Because of the high voltage values of operation the triggering system is not trivial and requires careful design. To serve this function we decided to acquire a commercial trigger unit along with the thyristors (DCR1050F) from Dynex Semi-Conductor. A 6 kV, 10 kJ/s capacitor charging power supply supplied by General Atomics Energy Division is used to power each of the PFN units**.** To operate the units at 5 Hz the charging and firing need to happen in less than 200 ms. It can be seen in Figure 3.11 that the supply can charge the capacitor to 4.6 kV within a 200 ms window which is theoretically sufficient for 2.5 kJ per shot operation. To operate at higher charge voltages at the same repetition rate of 5 Hz the charge time needs to be reduced, which could be accomplished by adding another charging supply in parallel.

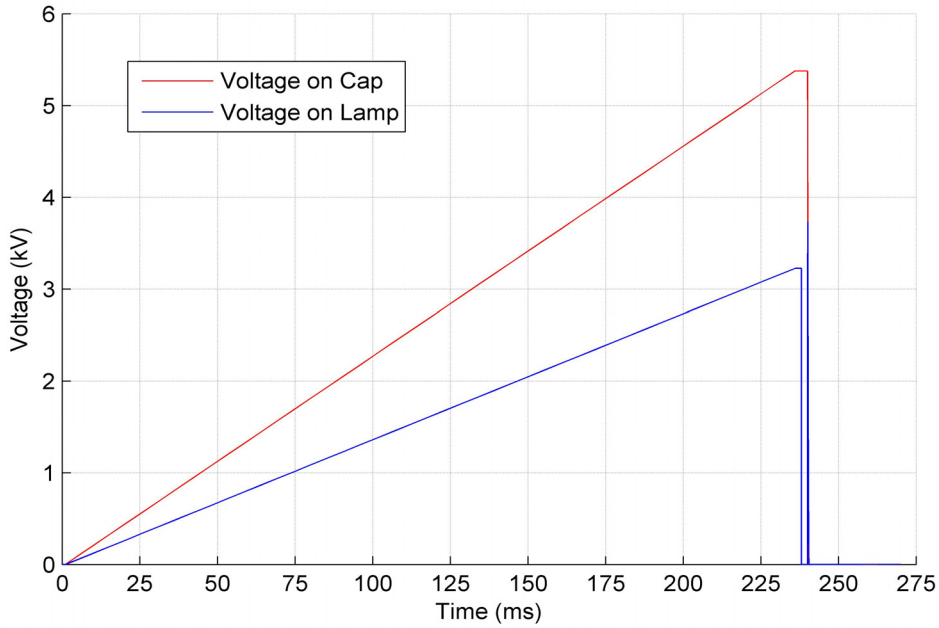

Figure 3.11 – Simulated charging and firing (240 ms) of the pulse forming network.

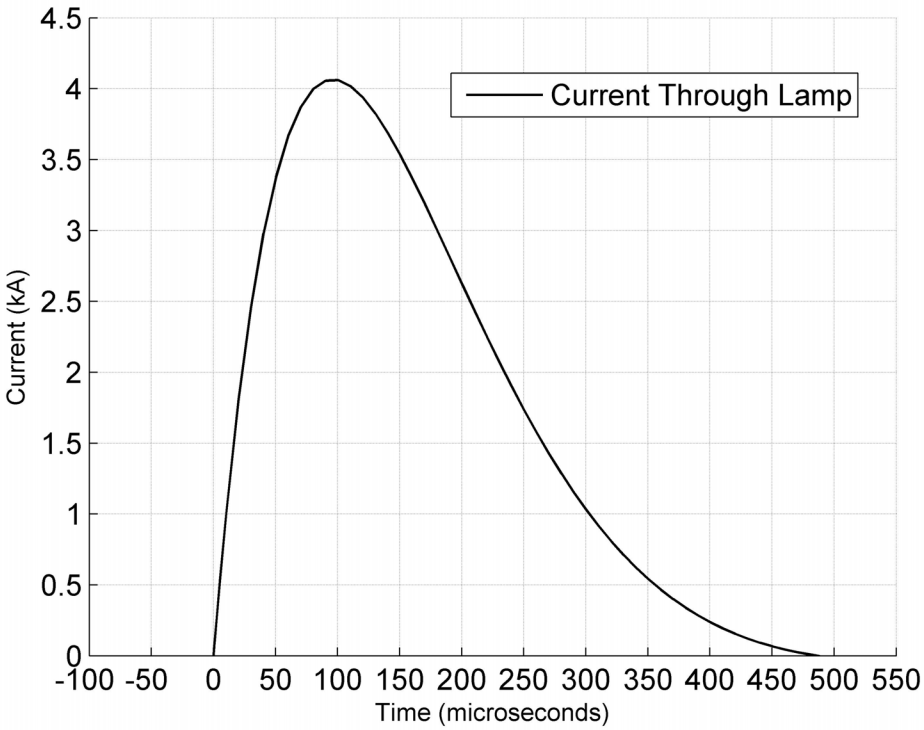

Figure 3.12 – Simulated 210 µs FWHM current pulse delivered by the pulse forming network into a set of two lamps connected in series approximated at 1 ohm.

3.2.2 Simmering of Lamps and Ignition

To light the lamps a field close to 1kV per inch of arc length is needed. This is over 15 kV for one lamp and 30 kV for two lamps in series. This voltage is much larger than the charge voltage required for the capacitor to reach the required energy. The solution employed to solve this problem is to create a large transient electric field between the anode and the wall of the lamp. If the field is large enough, an arc will develop between the two which then cascades down the inner surface of the lamp to the cathode, creating a current path. This allows the lamp to light. A field of sufficient magnitude can be created by wrapping a thin wire around the length of the flow tube that encloses the lamp (Figure 3.13). To ignite the lamp a large voltage is applied to the anode (~ 3 kV) while the wire is randomly pulsed at a voltage close to -20 kV.

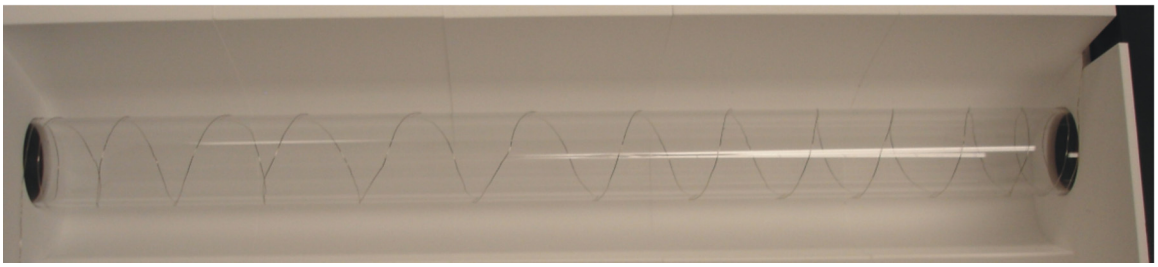

Figure 3.13 – Picture of ignition wire wrapped around the flow tube that cools the lamp.

As the arc starts, it follows the spiraling wire down to the cathode. To simmer the lamp, current is provided at the time the lamp ignites. To create the "- 20 kV" pulses, small pulse transformers with a fairly high turn ratio of 1:36 are employed which converts a provided 63 mJ, -520 V pulse to -18.7 kV. These pulses are just longer than 1 μs in time and occur at rate of 20-30 Hz until the lamp is lit.

The simmering of the lamps must be carefully investigated for it is not trivial due to the large energy pulses and the inherent variable resistance. A lamp may “blow out” (stop simmering) after a large energy pulse if an under-damped response is initiated causing a severe decline or reversal in the simmering current. As discussed above, the resistance of the lamps is dependent on the current flowing through them. An under-damped response is often initiated after a high energy large current pulse because of the extremely small resistance the LC circuit interacts with at the time of the peak value of the current. As the large amount of energy stored in the capacitor is dissipated, the inductance in the circuit will continue to try and draw the large current that was seen earlier. The voltage on the capacitor should not reverse if the RLC circuit is sufficiently damped, but in this case the current will rapidly decrease and possibly reverse, thus raising the resistance in the lamps. Eventually the current falls below a certain threshold and the lamp “blow out” occurs. A large robust independent current source can prevent this from happening by keeping the current above the simmering threshold and ensuring the resistance does not approach infinity. It is important to make sure the lamps do not turn off after the high energy pulse because the process to light the lamps is random, and the process can only occur when the 20-30 Hz trigger pulse is present. If it is desired to run the system, at for example 5 Hz, the system cannot be dependent on a random process to light the lamps after every shot, otherwise they may not be simmering when the large energy pulse arrives. This could cause many problems such as incorrect timing of the flash pulse, stress on protection electronics from the lamps not firing, degradation of the thyristors and the production of erratic current pulses.

To control the trigger pulses and provide a simmer current we selected to use a commercially available simmer. In general, most commercial simmers have circuitry that control the trigger pulses mentioned above while holding a large voltage on the anode. Once it senses the lamps are lit, the simmer circuit stops the trigger pulses and provides current at a lower voltage, which is similar to fluorescent lighting ballasts. However, unlike the ballasts, the circuitry can also sense when an energy pulse has been fired. Upon detection of an energy pulse, the unit boosts the simmer current being provided by as much as 60% for a short amount of time compensating for the under-damped effect to keep the lamps simmering. After some research, it was found that a commercially available simmer for our rather large lamps did not exist. The most powerful simmer available is rated at 60 W with a maximum simmer current of 500 mA (the minimum recommended for these lamps), and a boost current of 800 mA. Because of the two large lamps in series that this PFN has to drive, we chose to use two of these commercial simmers provided by Analog Modules in parallel. This gives the unit 1 A of simmer current and 1.6 A of boost current. Even though this is a sufficient amount of current, the maximum voltage the unit can provide is only 1500 V. It was found experimentally that this voltage is not sufficiently large to light the two lamps in series along with the trigger pulses. The first solution attempted was to add a large resistance in parallel with the thyristors to raise the voltage on the lamps. Since in most cases the capacitor is charged above 4 kV, this method provides a high enough voltage on the anode for the lamp to light. This solution is also convenient because the semi-conductor switches being used already have two 47 kΩ resistors in series across each thyristor to ensure voltage sharing across the two. However, care must be taken when building this system because the

simmer units can only withstand a voltage of 3 kV. A solution for this problem is to have protection diodes in series that can handle the 500 mA of current and the high voltage. We chose to use three 5 kV diodes in series that can endure a current of 1 A, rather than submerging a smaller number in an insulating material like silicon or oil. If more than 3.3 kV is applied across one single diode it would create a large probability of arcing across the unit causing significant damage. As stated above, a boost current of 1.6 A is enough to keep the lamps lit even if they were larger. However, once a prototype was built, it was found that the lamps would go out after every shot. The problem developed from the fact that the simmer units are only 60 W. As discussed above, after the large energy pulse the current drops and may start to reverse which raises the resistance of the lamp. To overcome this, the boost current normally engages and would be able to prevent the rise of resistance and keep the lamps on. However, because the resistance becomes large, the required voltage across the lamps to maintain a current flowing also becomes larger. This effect lowers the simmers' ability to provide sufficient current. At 120 V the simmer can provide 500 mA, but at 1500 V, the simmer can only provide 40 mA which is not enough current to simmer the lamps let alone drive the resistance down and overcome a voltage reversal caused by the ringing of the RLC circuit. As seen in section 3.3, when a lamp shot is fired the resistance grows sufficiently to cause a voltage spike of up to 3 kV on the lamps (dependent on the charge voltage of the capacitor) which is larger than the maximum voltage the simmers can provide. A robust current source that can solve this problem must be able to provide tens of milliamps at kilovolts which can drive the resistance of the lamps down.

The solution chosen to overcome this problem consisted in the use of a high voltage transformer which can provide the current needed at a sufficiently high voltage. Fellow graduate student Mike Grisham found a standard 9 kV (center tapped to ground) neon sign transformer which had a power rating of 360 VA. This is a relatively inexpensive solution because it is based on a standard component used in many industries. The output of this transformer is rectified and connected in parallel to the simmers (Figure 3.14).

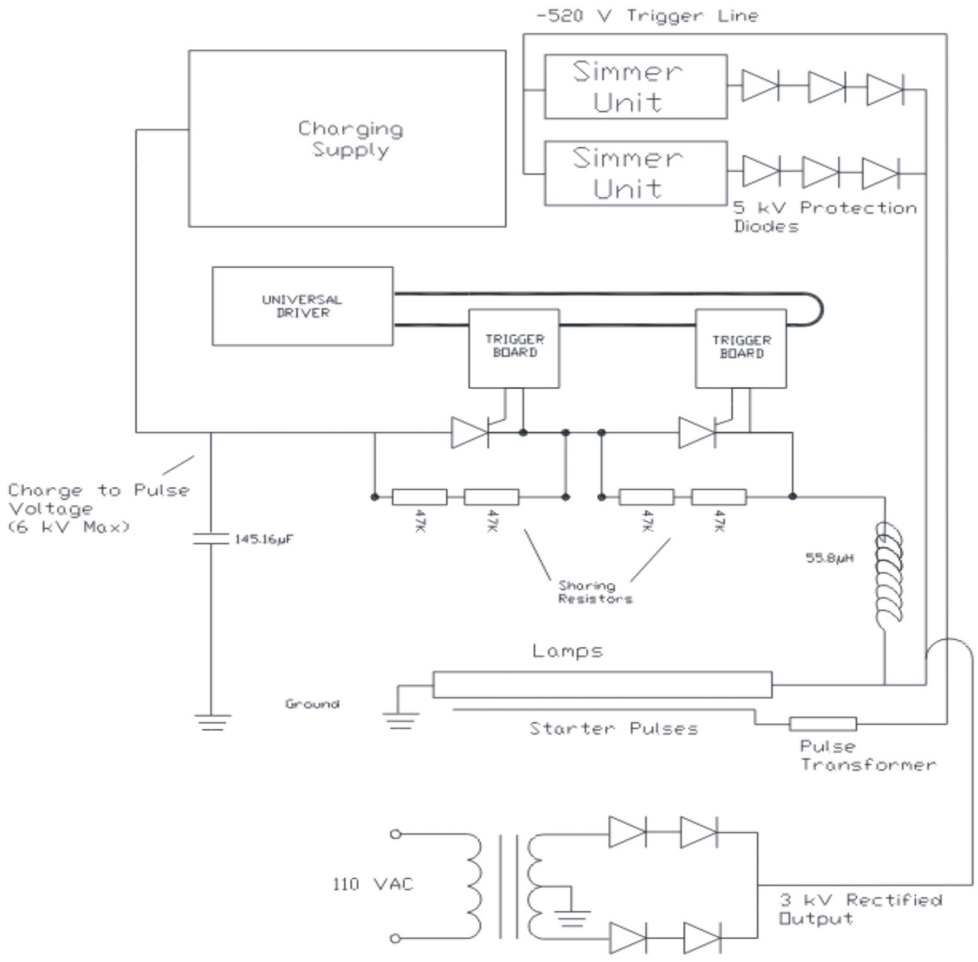

Figure 3.14 – PFN schematic with high voltage transformer included.

As a result of the rectification, the transformer's output became a 4.5 kV half sinusoid that can provide a robust 60 mA AC current**.** This solved the problem of the lamps blowing out after the high energy pulse while allowing the lamps to light independent of the charge voltage on the capacitor. Shown in Figure 3.14 is a schematic of the final design including the neon sign transformer.

3.2.3 Control

Aside from the PFN and simmer systems, there is a simple support and control electronic system that was designed for safety, troubleshooting and trigger control. We included a power control switch which turns on the system's components, including the semi-conductor switch driver board and fans. There is also a simmer control switch which activates the simmers and the neon sign transformer. When this switch is closed it also opens a relay connected between the large capacitor and a resistor to ground as a safety measure. When the simmers are off, the safety resistor drains the capacitor to prevent any dangers that can arise from a charged capacitor. The triggering of the semi-conductor switches is controlled by a TTL signal generated from another PFN or a signal generator which manages the whole laser system. The signal can be viewed by the two red LEDs that are also located on the front panel. This TTL signal is opto-coupled into the universal driver board of the SCRs to create isolation in case of failure. The front panel also contains a voltage display that shows the voltage on the capacitor and normally reads zero unless the SCRs have not fired. Indicator lights are provided to signify power to the unit, active power to the simmer supplies, and a simmer indication is added to notify the user the lamps are simmering. As stated above, the capacitor is charged by a

commercially available capacitor charging power supply, which is housed in a separate unit. This supply can be adjusted from 0 to 6 kV as to control the amount of energy delivered to the lamps. These power supplies are controlled by a 10 V inhibit signal. When the unit sees a 10 V signal it charges. An independent timing unit such as a Stanford DG535, can be used to control the charging of the capacitor and the subsequent firing of the thyristors. In Figure 3.15 the timing of the signals is shown.

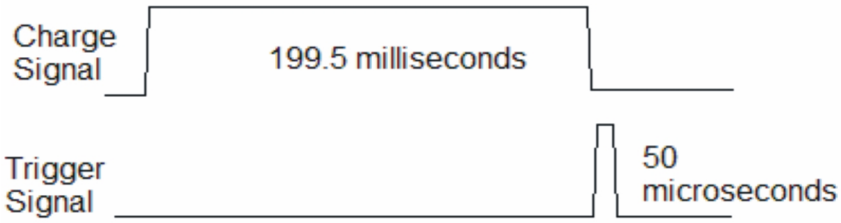

Figure 3.15 – Simple timing diagram for control of PFNs

This trigger pulse does not need to be any specific width as there is an intermediate timing board installed in the unit. This timing board converts any trigger signal that is provided into a 50 μs pulse, which is required by the SCRs. It also should be noted that the minimum amount of time the SCRs can be latched before they can recover and stop the flow of current is 500 μs. As long as the charge time is kept below 200 ms the theoretical repetition rate the PFN system can operate at is 5 Hz. The PFN units also have interlocks that prevent simmering and firing of the SCRs if the conditions are not correct. The unit will not fire if the lamps are not simmering. Furthermore there is an interlock that detects a signal from the chilling units which will disable both charging of the capacitor as well as simmering if water is not flowing or the temperature becomes too high.

3.2.4 Lifetime of Lamps

The lifetime of the lamps has been a difficult issue in the construction of the slab amplifier heads and the improvement has become an iterative processes which involves the participation of three companies; Fenix Technology, Applied Photon Technology and Heraeus Noblelight. Each company has provided a different version of the lamps changing the anode and cathode materials and shape, the electrical connection method as well as the bore material. Originally Fenix technology provided a lamp with 12 gauge wire connections, a bore material of simple low quality quartz and an anode/cathode glass seal design that would crack when the lamps were run at a repetition rate higher than 1 Hz. Through much iteration the new lamps provided by all three companies now have anode/cathode designs that do not sputter when fired, anode/cathode seals that do not crack when operated at 5 Hz, new higher quality bore materials and 6 mm connection stubs. The use of silver plated connectors which are loaded with gold plated springs provide an electrical connection that reduces stress on the lamp while providing good electrical conductivity. All of these improvements have reduced heating and stress effects while increasing the lifetime of the lamps. Shown in Figure 3.16 is a generic drawing for the lamps used.

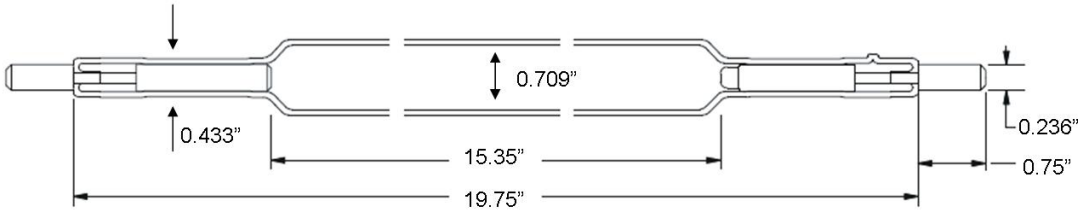

Figure 3.16 – Drawing of Xe flashlamp.

The lifetime of the lamps seems to now be dependent on the time it takes for the bore material to solarize. This UV degradation effect reduces the transmission of the glass resulting in less pump light arriving to the slab lowering the gain. To combat this effect Fenix Technology has provided higher quality quartz, Heraeus Noblelight has provided Titanium-doped quartz and APT has provided both Ti-doped quartz as well as Cerium-doped quartz. The three bore materials are expected to further increase the lifetime and are now is use in our system. This will eventually provide direct lifetime comparison data.

3.3 Electrical Pulse Measurements

Presented in Figure 3.17 are three voltage pulses measured at the anode of the two lamps in series using the circuit configuration with the high voltage transformer disconnected. In all three cases the lamps blew out. It can be seen 1.7 ms after the beginning pulse that the voltage drop across the lamps starts to rise due to the increase in the lamp's resistance. This results from the fact that there is not enough current being provided by the simmers. Also it can be observed that as the capacitor voltage is increased and more energy is deposited into the lamps, the slower the resistance grows. Figure 3.18 shows a voltage pulse measured across the lamps for the case of operation with the simmer transformer connected. As can be seen, the resistance does not grow for several milliseconds after the pulse. It was observed that the lamps did stay on using this circuit configuration.

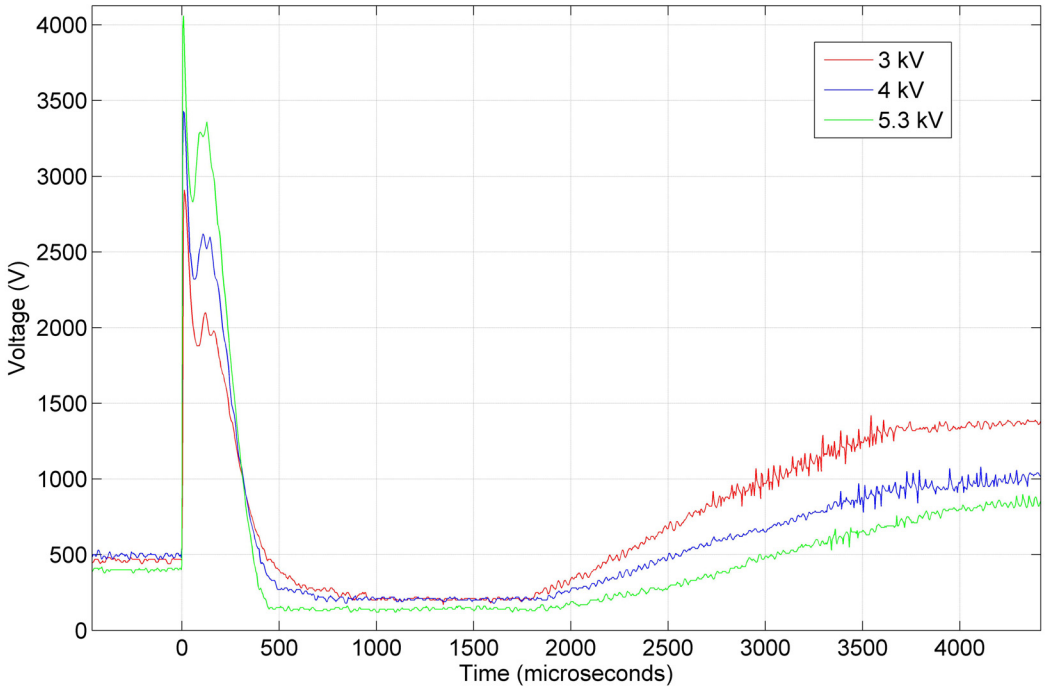

Figure 3.17 – Voltage differentials measured across two lamps in series corresponding to different capacitor charge voltages without the high-voltage transformer.

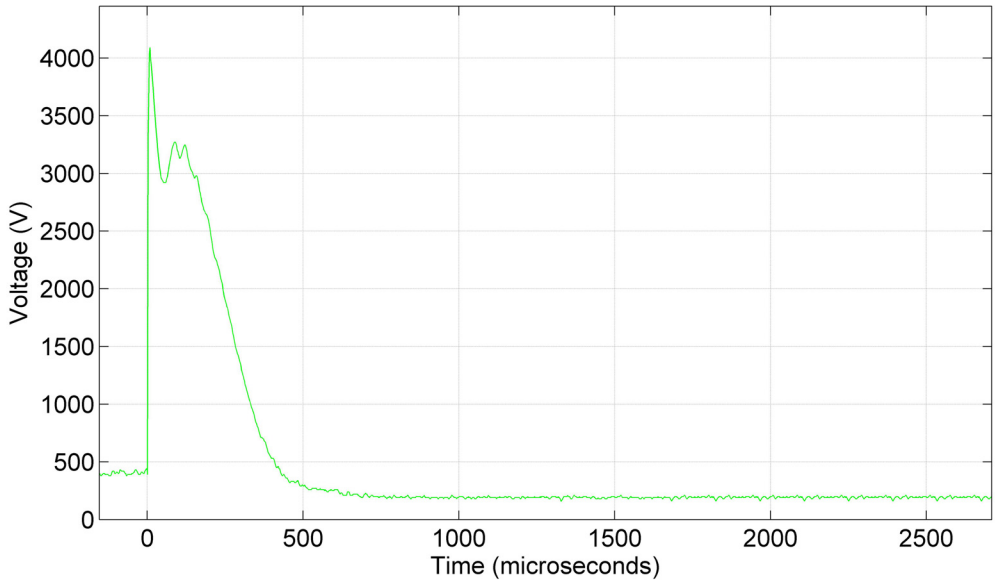

Figure 3.18 – Voltage differentials measured across two lamps in series corresponding to a 5.3 kV capacitor charge voltage with the high-voltage transformer connected.

Figure 3.19 shows the resistance does eventually grow, but the voltage never really increases much above 1 kV before it falls back to a normal simmering voltage.

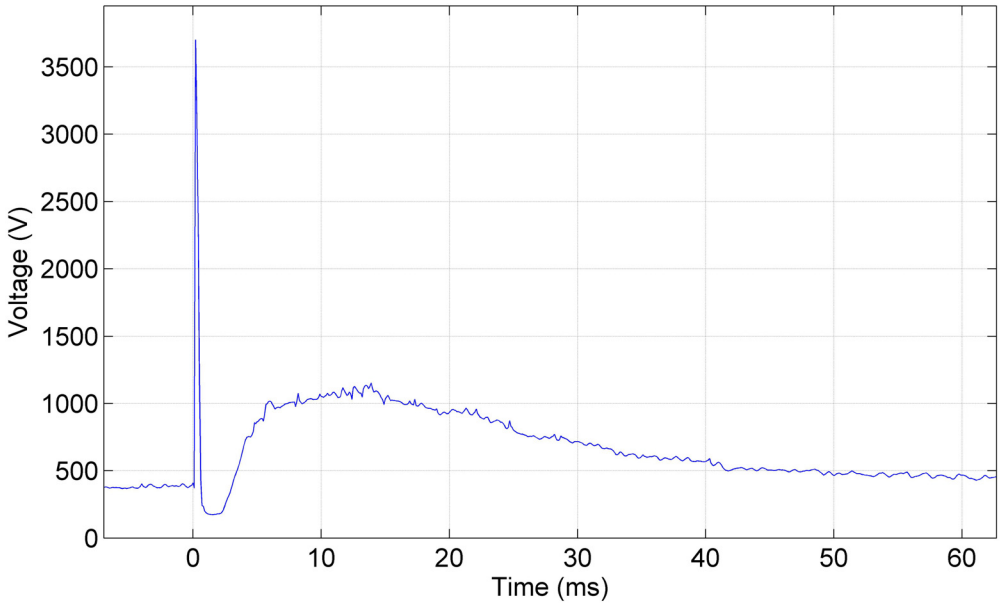

Figure 3.19 – Voltage differentials measured across two lamps in series corresponding to a 5.3 kV capacitor charge with high-voltage transformer connected.

From the figures above, it can be concluded that it is important to have a robust simmering configuration capable of supplying enough current at a high enough voltage to overcome the rise in resistance. Also, with new lamps, blow outs are still observed for ~ 100 "break in" shots, even with the simmer transformer installed. This problem in principle could be corrected with a higher voltage rated transformer (6 kV instead of 4.5 kV) and/or a higher current rated transformer capable of slowing down the rise in resistance even further. It should be noted that it is recommended on commercial PFNs to "break in" lamps before continuous use. This process ablates material from the anode and cathode removing coatings and impurities that may be present from the manufacturing process which can cause stability problems in the lamps. Figure 3.20 shows a voltage

pulse measured at the anode of two lamps in series which were pulsed with a simmer current lower than 100 mA. In this case the lamp did not blow out and the voltage spikes represent instabilities in the plasma column resulting in random increases in resistance.

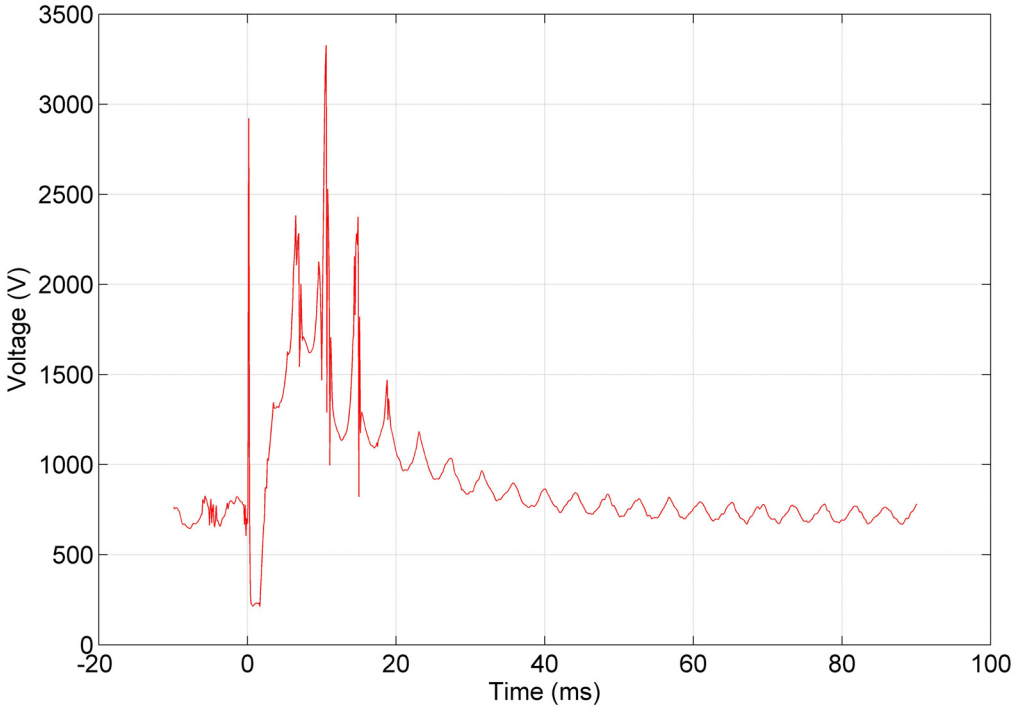

Figure 3.20 – Voltage differentials measured across two lamps in series corresponding to a 5.3 kV capacitor charge with < 100 mA simmer current. Modulations show instabilities in the plasma resulting in resistance spikes.

This data illustrates the importance of having enough simmer current to keep the resistance in the lamp low, thus allowing the pulse forming network to deliver energy with a smooth and stable current pulse.

Testing of a constructed prototype showed that the PFNs generate the expected current pulse width of close to 270 μs half cycle duration (Figure 3.21). Two PFN units were constructed and connected to power all four lamps in the laser head. Temperature tests were then on an undoped test slab while testing the repetition rate of the PFNs, as

discussed in section 3.1.2.4. Once 5 Hz operation of the PFN units was demonstrated using the undoped slab, the Nd:Glass slab was installed in the laser system.

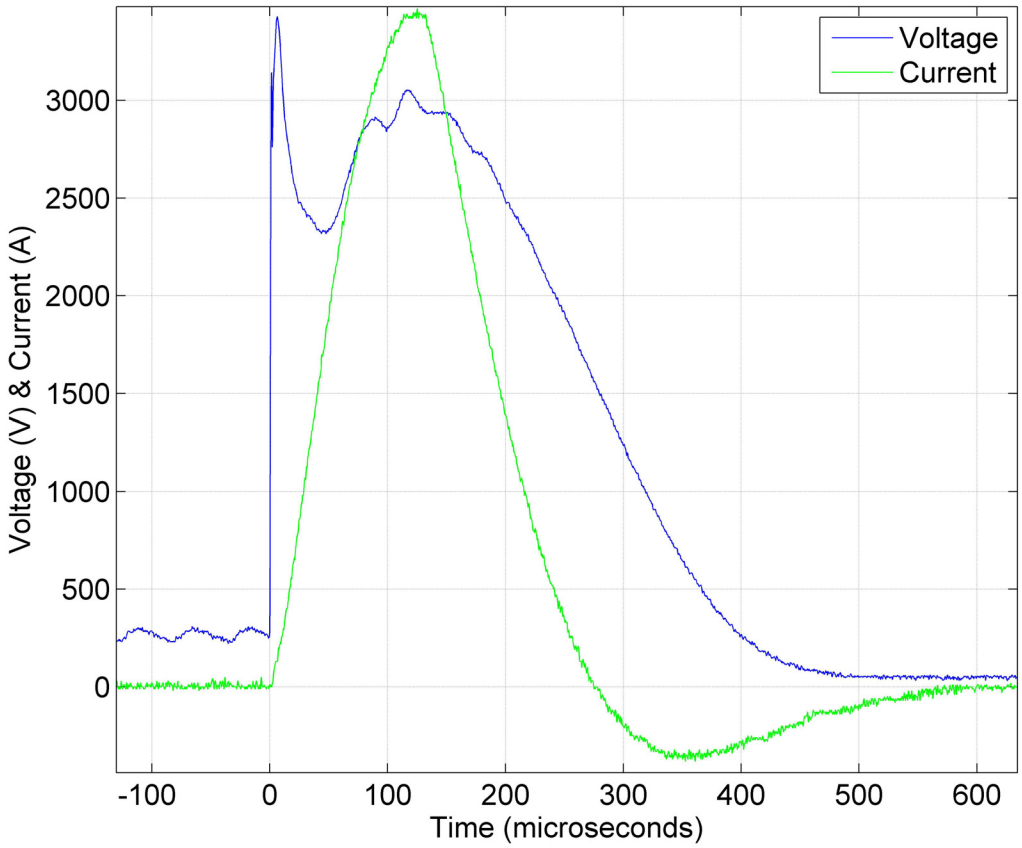

Figure 3.21 – Simultaneous voltage & current measurement across the two lamps connected in series

Results of the gain measurements presented in section 3.4 showed lower values of single pass amplification than expected for the excitation energy that is stored in the capacitor at given charge voltages [3]. To clarify the discrepancies, the measured current and voltage drops across the lamps (Figure 3.21) were integrated to obtain the energy, rather than assuming the capacitor's stored energy. Figure 3.22 compares the total measured energy delivered to all four lamps with the stored energy in a 145 µF capacitor (value specified in the design phase) as a function of capacitor charge voltage.

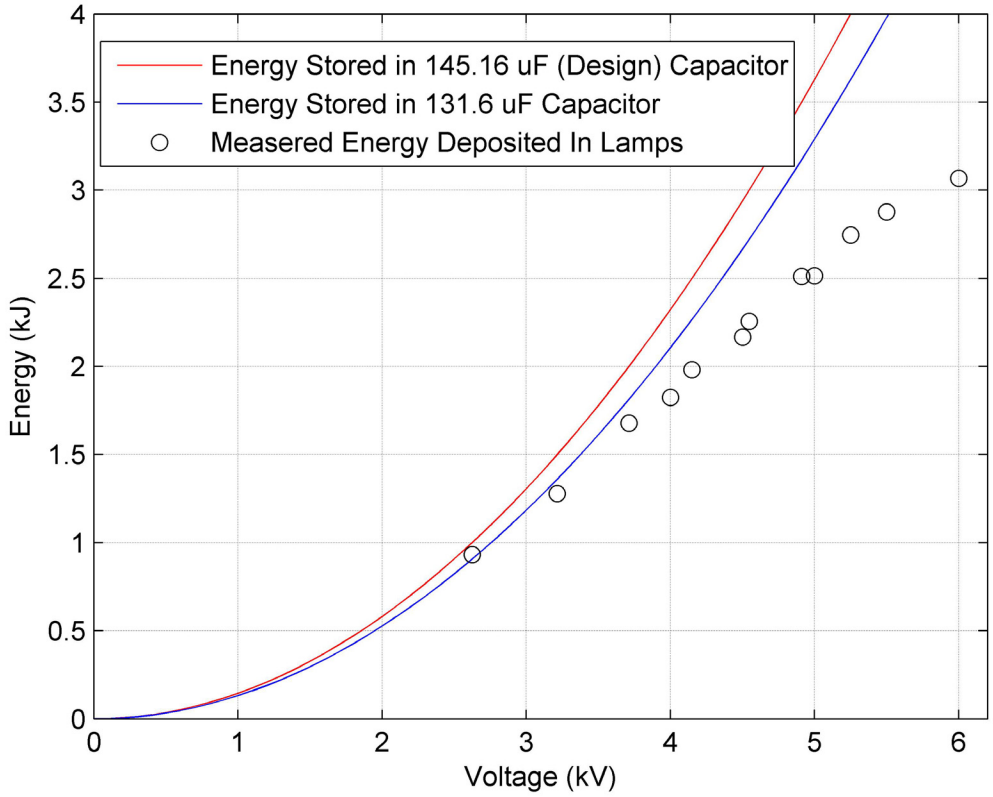

Figure 3.22 – Comparison of stored energy in the design capacitor (145.16 µF), the stored energy in the installed capacitor (131.6 µF) and the energy at the lamps versus capacitor charge voltage.

As discussed above, for one PFN, a 5.3 kV charge voltage corresponds to 2 kJ of energy stored in such a capacitor. This translates to 4 kJ deposited into four lamps when using two PFN units to power them. A lower measured 2.7 kJ pulse energy deposited into all four lamps at this charge voltage prompted further investigation. It was found that the capacitance value on the PFN discharge capacitor was lower than the specification, ~ 131 µF. More importantly, we found significant energy losses caused by energy dissipation in several of the PFN components. Because the resistance of the lamps drops at large currents values, the other resistance values inherent in the inductor and the wire become important. At high current values these small resistances play a significant role in determining the voltage drop across the lamps, and therefore the energy that is delivered.

For example, from a stored energy of 1.65 kJ obtained by charging a 131 μF capacitor to 5.3 kV, it was found that 266 J is dissipated in the inductor and 22 J is dissipated in the wire. In this case, the measured energy deposited into the lamps was determined to be 1.36 kJ for two lamps connected in series or 2.72 kJ for four lamps. This is a difference of close to 18% when compared to the stored energy in the discharge capacitor. Voltage drop measurements were taken across the components for a charge voltage of 4 kV in increments of 500 V up to 6 kV, and the percentage energy loss was calculated. Figure 3.23 shows the energy loss in the PFN circuit becomes larger as the charge voltage is increased due to the resistance in the lamps falling.

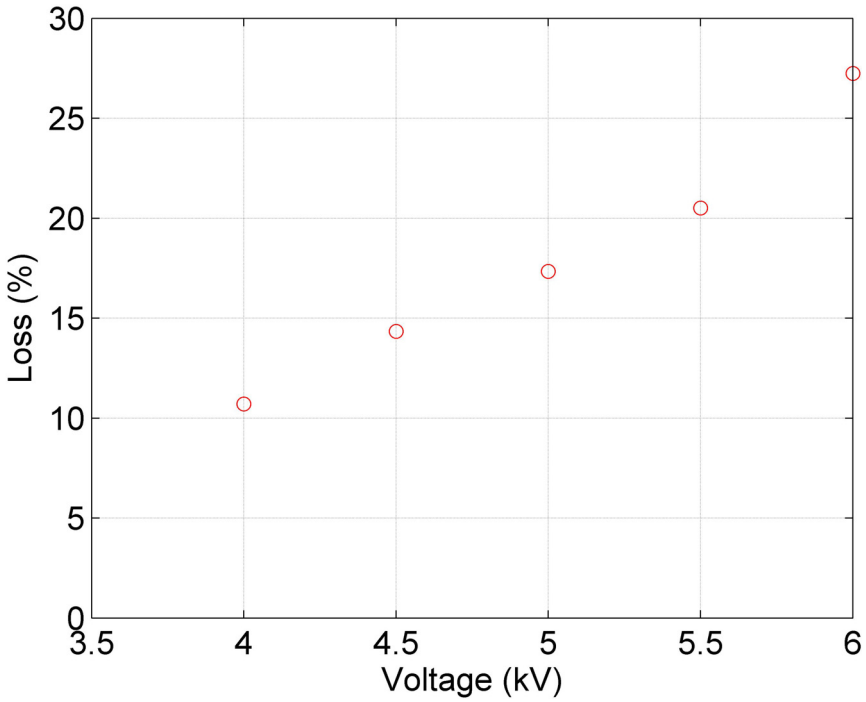

Figure 3.23 – Measured percentage of stored energy in a 131 μF capacitor lost in the PFN components as a function of capacitor charge voltage.

As described above, the observed increase in energy loss is due to a drop in the lamp resistance at high current values, which results in a larger fraction of the energy being dissipated in the rest of the circuit's inherent resistances.

3.4 Gain Measurement

In this section results are presented of the operation of the laser amplifier. The single pass gain as a function of flash lamp pump energy was measured and compared with those of a similar slab amplifier developed by C.B. Dane et al. [3].

3.4.1 Experimental Setup

To measure the single pass gain of the amplifier we used a 1053 nm wavelength probe pulse generated by the Q-switched Nd:YLF laser oscillator mentioned in Chapter 2. The oscillator produces pulses of about 10 mJ with a ~ 20 ns duration at a repetition rate of 5 Hz. However, a shutter was used to allow for measurements at a repetition frequency of two shots per minute. A probe laser beam with a diameter of 6 mm was used to measure the variation of the gain as a function of position along the 14 cm height of the slab amplifier.

The experimental setup used to perform the measurement is shown in Figure 3.24. The beam was aligned along the same path as a full sized beam would take. This path involved 6 total internal reflections before exiting out the opposite side, to constitute a total path length of 40.4 cm through the glass slab, of which approximately 39.6 cm are through the region pumped by the lamps.

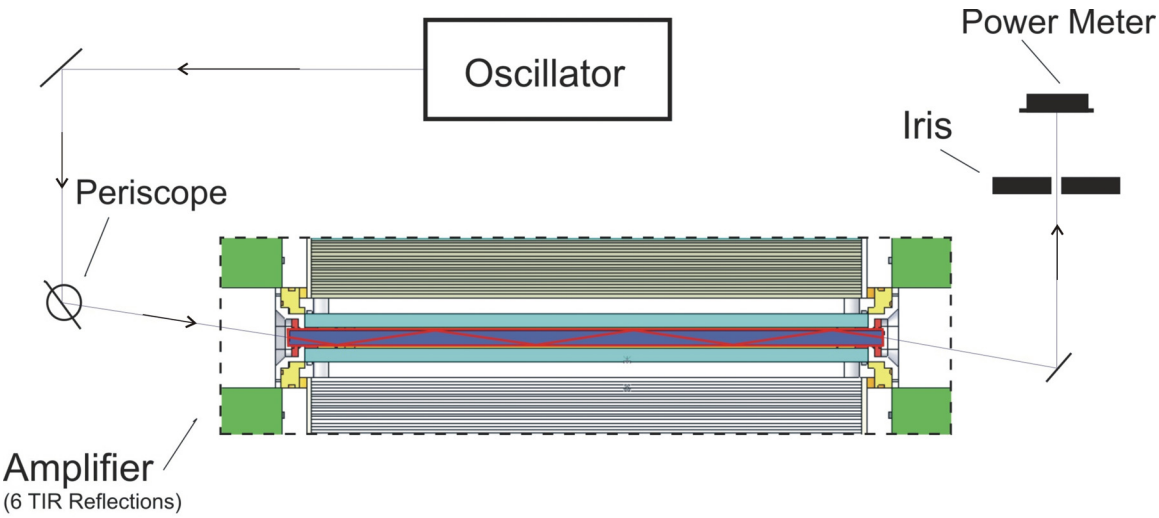

Figure 3.24 – Experimental setup of gain measurement.

Once the beam passed through the slab it impinged on a mirror which re-directed the beam through an iris placed at 120 cm from the exit of the slab. The iris served the purpose of reducing the amount of ASE reaching the power meter to ensure that it would not affect the measurements. This was verified by closing the iris until the meter did not respond when the amplifier was flashed with no pulse present. The measurements were conducted using a pyro-electric power meter which was calibrated shortly before the measurements were conducted.

3.4.2 Single Pass Gain Measurements

Single pass gain measurements were taken as a function of flash lamp energy. The amplification was determined by measuring the ratio of the energy of the amplified output beam over the input beam energy. An average of ten shots was obtained for each lamp voltage. Prior to conducting the measurements we optimized the time delay between the initiation of the flashlamp pulse and the injection of the probe beam into the amplifiers. The measurements were conducted for excitation pulses of 2.5 kJ at the

location corresponding to the center of the 14 cm dimension of the slab. Maximum amplification was observed at 260 μs after the firing of the flashlamps.

Originally the capacitor charge voltages were used to compute the amount of energy that was put into the lamps. Under this condition the gain measured was smaller than expected. It was found, as described in Section 3.3, that losses in the PFN supply reduced the voltage applied to the lamps to values significantly lower than the capacitor charge voltage, resulting in a lower excitation energy and lower gain. To plot the correct dependence of gain as a function of excitation voltage we proceeded to measure the voltage drop directly across the lamps.

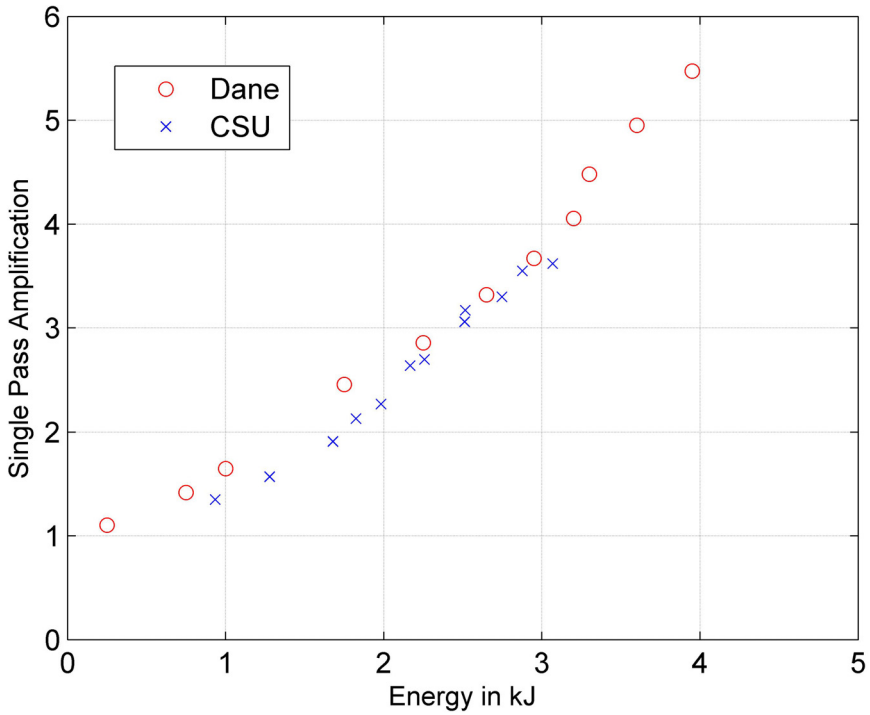

Figure 3.25 – Measured single pass amplification vs. energy deposited at lamps. The measurements are compared to published data corresponding to a similar amplifier [3.1].

In Figure 3.25 the excitation energy is computed based on the lamp voltage and current. The corresponding charge voltages can be taken from Figure 3.22 in section 3.3. As can be seen in Figure 3.25, the measured single pass gain data points have a very similar slope and value when compared to what is reported in the literature for a similar amplifier [3]. Because of the losses the PFNs, which were designed for a maximum charging voltage of 6 KV, could not reach total deposited lamp energy of 4 kJ. The energy delivered to the lamps for this maximum voltage was just above 3 kJ. Even though it was found that 4 kJ/pulse could not be reached, the amplifier was successful in obtaining a gain of 3.3x per pass at a lamp excitation energy of 2.7 kJ/pulse, which was the goal stated earlier.

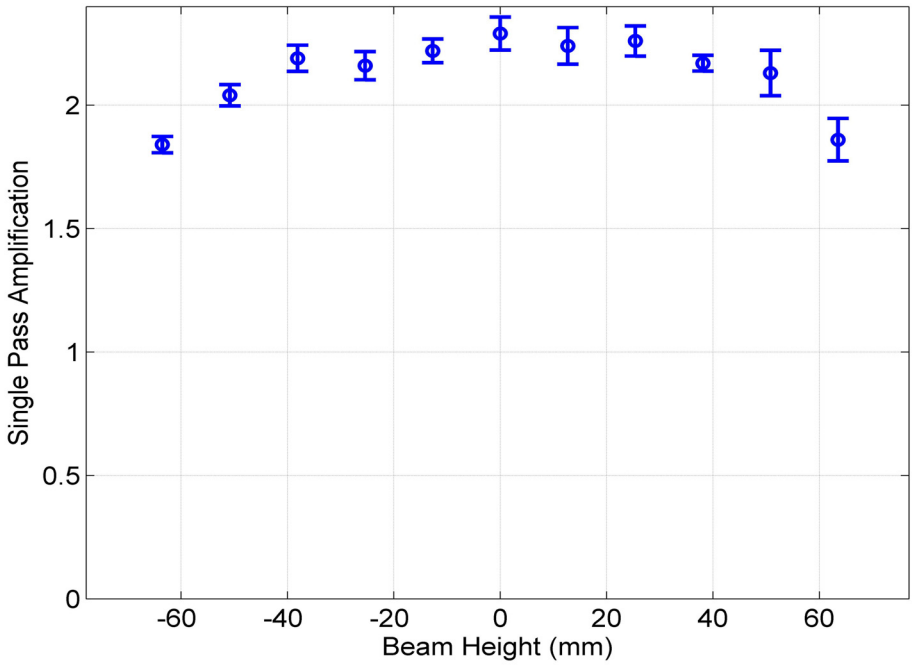

Figure 3.26 – Measured single pass amplification vs. beam height in the glass slab. The zero of the horizontal axis corresponds to the center of the slab.

The spatial variation of the gain along the height of the slab was also measured. This gain distribution depends on the uniformity of the pumping. Figure 3.26 shows the

gain distribution measured using a periscope to send the beam through at different heights. This data was taken at lamp excitation energy of 2 kJ per pulse. This energy level was not known at the time of the measurement because losses in the PFN had not been determined, but was calibrated afterwards. It shows that in the 8 cm midsection of the slab the gain is relatively uniform, tapering off at both ends of the slab. This is due to diminished pumping towards the edges of the slab.

3.5 Summary

Covered in this chapter are the physical design considerations for the amplifier head, the power system, the chilling unit and gain characterization. Also described is the integration of all the components, including the sensors and interlocks installed to facilitate the reliable and safe operation of the system. The technical solutions that were implemented to obtain reliable simmering of the flashlamps are described, as well as the testing and characterization of the electrical and cooling parameters. Measurements were conducted to determine the relationship between the energy stored in the capacitors and the energy delivered into the lamps. It was found that due to the decrease of the resistance in the lamps with increased excitation current, the percentage PFN stored energy delivered into the lamps decreases as the excitation energy is incremented. At the maximum capacitor charge voltage of 6 kV excitation energy of 3 kJ is delivered to the lamps, with a corresponding loss of 27% of the energy in the PFN components. The slab cooling unit designed to provide a turbulent cooling flow of 180 liters per minute was tested, and the water temperature increase across the slab was measured under repetitive flash lamp operation. Data was also presented indicating that a Nd:Glass slab amplifier

has successfully been built to generate a single pass gain of 3.3. The gain was measured to be relatively uniform in the ~ 8 cm central region of the main axis of the slab face, tapering off towards the edges as the pumping flux decreases. The measured uniformity and gain of 3.3 is sufficient to generate a beam with the desired energy after multi-pass amplification. The PFN and chilling units have proved to be reliable.

3.6 References

1. L. A. Hackel and C. B. Dane, U.S. Patent 5 239 408 (1993).
2. J. L. Miller, L. A. Hackel, C. B. Dane, and L. E. Zapata, U.S. Patent 5 285 310 (1994).
3. C. B. Dane, L. E. Zapata, W. A. Neuman, M. A. Norton, and L. A. Hackel, "Design and operation of a 150 W near diffraction-limited laser amplifier with SBS wavefront correction," IEEE Journal of Quantum Electronics **31**, 148-163 (1995).
4. "APG1 Specifications Sheet," (Provided by SCHOTT North America Inc., 555 Taxter Road, Elmsford, NY 10523 USA).
5. M. J. Shoup, J. H. Kelly, and D. L. Smith, "Design and testing of a large-aperture, high-gain, Brewster's angle zigzag Nd:glass slab amplifier," Applied Optics **36**, 5827-5838 (1997).
6. J. Eggleston, T. Kane, K. Kuhn, J. Unternahrer, and R. Byer, "The slab geometry laser--Part I: Theory," IEEE Journal of Quantum Electronics **20**, 289-301 (1984).
7. T. Kane, J. Eggleston, and R. Byer, "The slab geometry laser-II: Thermal effects in a finite slab," IEEE Journal of Quantum Electronics **21**, 1195-1210 (1985).
8. D. Pnueli, *Fluid Mechanics* (Cambridge Univeristy Press, New York, NY, 1992).
9. Koechner and Bass, *Solid-State Lasers* (Springer-Vrelag, New York, NY, 2003).
10. D. R. Askeland and P. P. Phulé, *The Science and Engineering of Materials,* 5 ed. (Nelson, a division of Thomson Canada Limited, Toronto, Ontario, Canada, 2006).
11. E. Doner and P. Platte, (Figure Authors).

12. "Ovisil Transmission Spectrum of #482 glass tube," (2005).

13. J. F. Holzrichter and J. L. Emmett, "Design and Analysis of a High Brightness Axial Flash lamp," Appl. Opt. **8**, 1459-1465 (1969).

14. C. Bibeau, S. A. Payne, and H. T. Powell, "Direct measurements of the terminal laser level lifetime in neodymium-doped crystals and glasses," J. Opt. Soc. Am. B **12**, 1981-1992 (1995).

15. "Specifications from Fenix Technology, Applied Photon Technology and Heraeus Noblelight."

16. OrCAD - PSpice Analog and Mixed Signal Simulator, Cadence Design Systems Inc., 2005.

17. "Doc. DS5550-1.0 for Model DCR1050F," (Dynex Semi-Conductor, 2002).

CHAPTER 4

LARGE AREA HIGH EFFICIENCY BROAD BANDWIDTH 800 NM DIELECTRIC GRATINGS FOR HIGH ENERGY LASER PULSE

Published in: Optics Express Vol. 17, Issue 26, pp. 23809-23816 © 2009 Optical Society of America

Author List: D. H. Martz, H. T. Nguyen, D. Patel, J. A. Britten, D. Alessi, E. Krous, Y. Wang, M. A. Larotonda, J. George, B. Knollenberg, B. M. Luther, J. J. Rocca and C. S. Menoni

Abstract: We have demonstrated broad bandwidth large area (229 mm x 114 mm) multilayer dielectric diffraction gratings for the efficient compression of high energy 800 nm laser pulses at high average power. The gratings are etched in the top layers of an aperiodic $(Nb_{0.5}Ta_{0.5})_2O_5$-SiO_2 multilayer coating deposited by ion beam sputtering. The mean efficiency of the grating across the area is better than 97% at the center wavelength and remains above 96% at wavelengths between 820 nm and 780 nm. The gratings were used to compress 5.5 J pulses from a Ti:sapphire laser with an efficiency above 80 percent.

4.1 Introduction

The grating compressor [1] is one of the most critical components of a high power chirped pulse amplification (CPA) laser system [2]. Requirements for the diffraction gratings include: high diffraction efficiency, high damage threshold, and often the ability

to withstand high average powers. Until recently, CPA laser systems have almost exclusively made use of metallic diffraction gratings, in which the diffractive structure is typically coated with a thin gold film. These gold-coated pulse compression gratings have allowed the implementation of a number of high power laser systems around the world. [3-5]. An all-dielectric grating alternative was first proposed in 1991 as a possible solution to improve throughput, increase the damage threshold and maximize average power operation [6]. Moreover, dielectric gratings are less prone to experience the degradation that is frequently observed in gold coated gratings. Since then, the fabrication method pioneered at Lawrence Livermore National Laboratory has allowed the production of very large area multilayer dielectric (MLD) gratings operating at a centered wavelength λ= 1 μm with all the advantages listed above [7, 8]. However, it has been difficult to produce a dielectric grating design for pulse compression at λ= 800 nm. Recently, results from λ= 800 nm all-dielectric HfO_2-SiO_2 gratings and metal-dielectric gratings manufactured in 25 mm diameter substrates have been reported [9]. The dielectric gratings were reported to have a diffraction efficiency of 96 percent over a bandwidth of 38 nm, and a high damage threshold.

Hereafter we present results of the development and fabrication of broad bandwidth large area MLD gratings for the compression of Ti:sapphire laser pulses based on a $(Nb_{0.5}Ta_{0.5})_2O_5$-SiO_2 multilayer coating. The measured -1st order diffraction efficiency of these MLD gratings is better than 97% at 800 nm and above 96% over a spectral bandwidth of at least 40 nm. The gratings were used to compress 5.5 J pulses from a Ti:sapphire laser with an efficiency more than 80 percent.

4.2 Grating design

The grating was designed to have a line density of 1740 lines/mm, giving a Littrow angle of 44.1 degrees at a wavelength of 800 nm, while allowing for a large acceptance angle of at least 10 degrees from Littrow. This corresponds to input and output operating angles of ~35 and ~55 degrees respectively. The grating was designed to have maximum diffraction efficiency at a center wavelength of 800 nm and a bandwidth acceptance of more than 60 nm.

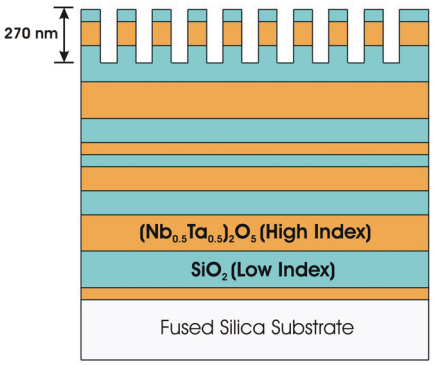

Figure 4.1 Schematic diagram of a dielectric multilayer deposited on top of a fused silica substrate. The reflective multilayer stack has 20 layers.

The grating design consists of a MLD high reflectance interference coating with grooves etched into the top layers (Figure 4.1). The high reflector (HR) is created by an asymmetric dielectric stack with 20 alternating layers of high $(Nb_{0.5}Ta_{0.5})_2O_5$ and low SiO_2 index materials. This material combination was selected because it offers large index contrast and the possibility of designing a large bandwidth grating at 800 nm. The grooves are etched to be 270 nm deep, and reside in the top three layers rather than confined to the low index capping layer, which is a common practice.

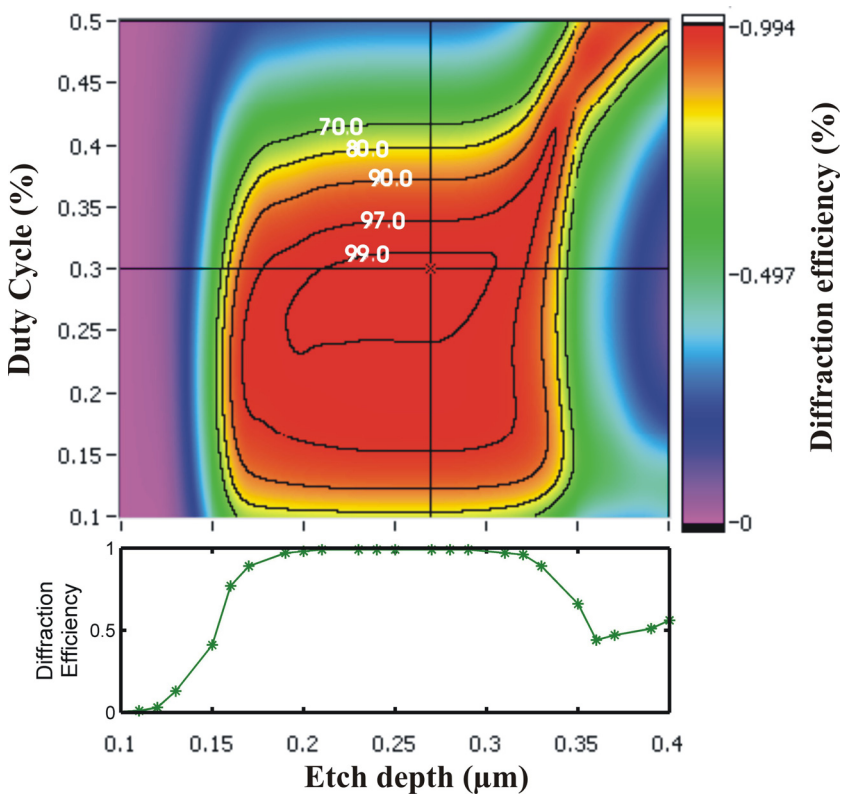

Figure 4.2 Simulated diffraction efficiency map of the -1st order of an 800 nm grating operating at an angle of 38 degrees as a function of etch depth and duty cycle of the line pattern. The contours indicate constant diffraction efficiency. The cut shows the variation of diffraction efficiency versus etch depth at the optimum, 30% duty cycle.

Figure 4.2 shows the simulated -1st order diffraction efficiency of the MLD grating operating at an angle of incidence of 38 degrees computed as a function of the groove depth and the linewidth/separation ratio (duty cycle) of the line pattern. Both parameters affect the diffraction efficiency significantly. The crossed lines in Figure 4.2 identify the combination of parameters selected for fabrication, a groove depth of 270 nm and a duty cycle of 30%, and the corresponding simulated diffraction efficiency. Figure 4.3 illustrates the sensitivity of the MLD diffraction efficiency to variations of a few

percent to the duty cycle and groove depth. These effects make the manufacturing of MLD gratings very challenging if the process is not well controlled.

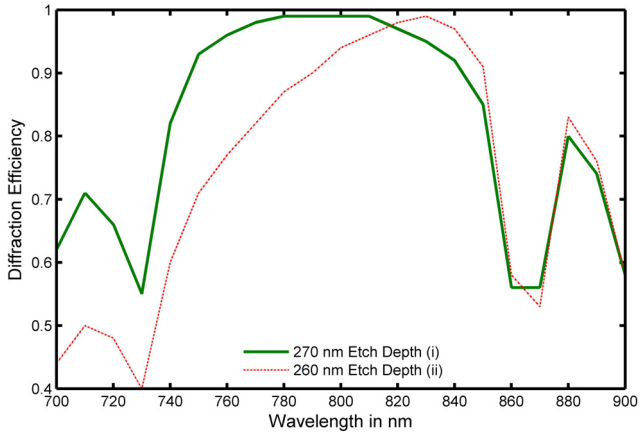

Figure 4.3. Simulated diffraction efficiency of the -1st order of an 800 nm grating operating at an angle of 38 degrees. (i) Optimum 270 nm groove depth with a 30% duty cycle (ii) 260 nm groove depth with a 36% duty cycle.

4.3 High reflector design, fabrication and testing

The MLD stack consists of sequential layers of SiO_2 and $(Nb_{0.5}Ta_{0.5})_2O_5$ with layer thickness varying from a minimum of 40 nm (thickness of the low index capping layer) to a maximum of 300 nm. The design offers 99.99% reflectivity at a centered wavelength of 800 nm. The reflection at a wavelength of 413 nm, corresponding to the krypton ion laser used in the lithographic process, is less than 10 percent. This requirement ensures minimum degradation of the holographic line pattern due to back-reflections. The MLD stacks were deposited by ion beam sputtering using a Veeco Spector ion beam deposition system equipped with a planetary apparatus capable to accommodate large substrates. The Spector® platform utilized a 16 cm RF deposition source and a 12 cm assist source which provided substrate cleaning and thin film stoichiometry control. Stringent control of layer thicknesses during deposition was

required to match the design and maintain a coating reflectivity uniformity of <1% centered at 800 nm across the entire substrate area.

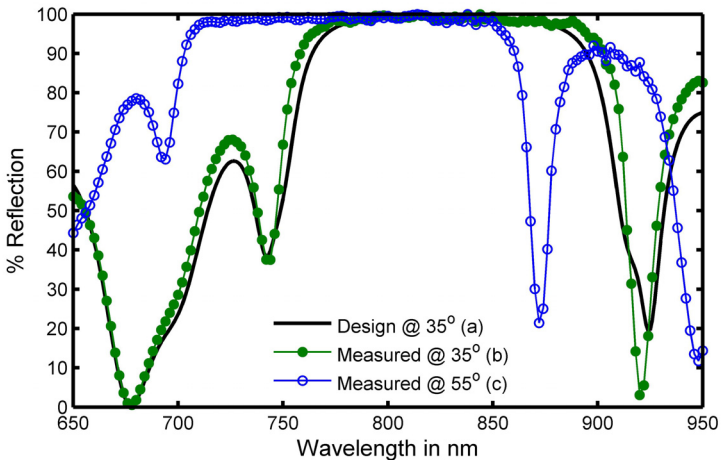

Figure 4.4 S-polarization spectral response of the asymmetric 20 layer MLD high reflector. Simulated (a) reflection at 35 degrees, measured reflection at 35 (b) and 55 (c) degrees.

The MLD stack was deposited onto 229 mm x 114 mm fused silica slabs. The measured S-polarization reflection of the MLD coatings obtained by elipsometery is shown in Figure 4.4. The plot compares the designed reflectivity at 35 degrees incidence angle (a) with the measured response (b). The agreement highlights the reliable layer thickness control obtained with the dual ion beam deposition system. The plot also compares the measured reflectance of the MLD stack at incidence angles of 35 (b) and 55 (c) degrees respectively, showing that the HR interference coating offers a 100 nm spectral window centered around 800 nm.

4.4 Grating fabrication and performance

The grating structure was printed into the multilayer dielectric coating by interferometric photolithography. A layer of photoresist deposited on top of the multilayer stack was exposed using a holographic exposure tool based on the λ= 413 nm

line of a krypton ion laser. Following exposure, the substrates were baked to harden the resist after which the fused silica slabs were inserted into a reactive ion-beam etching (RIBE) tool capable of etching submicron features into substrates. Etching was carried out with an etching gas mix of CHF_3, Ar and O_2 using the same protocol described in [8] for the fabrication of 1 μm MLD gratings. As mentioned above, the groove depth has a critical effect on the diffraction efficiency, requiring accurate control of the etching process across the entire grating surface.

The efficiency of the MLD gratings was measured over the entire area of the fused silica slab using the scanning photometry tool described in [10]. Figure 4.5 shows a map of the -1st order diffraction efficiency of a completed grating measured at a wavelength of 800 nm and at an incident angle of 38 degrees.

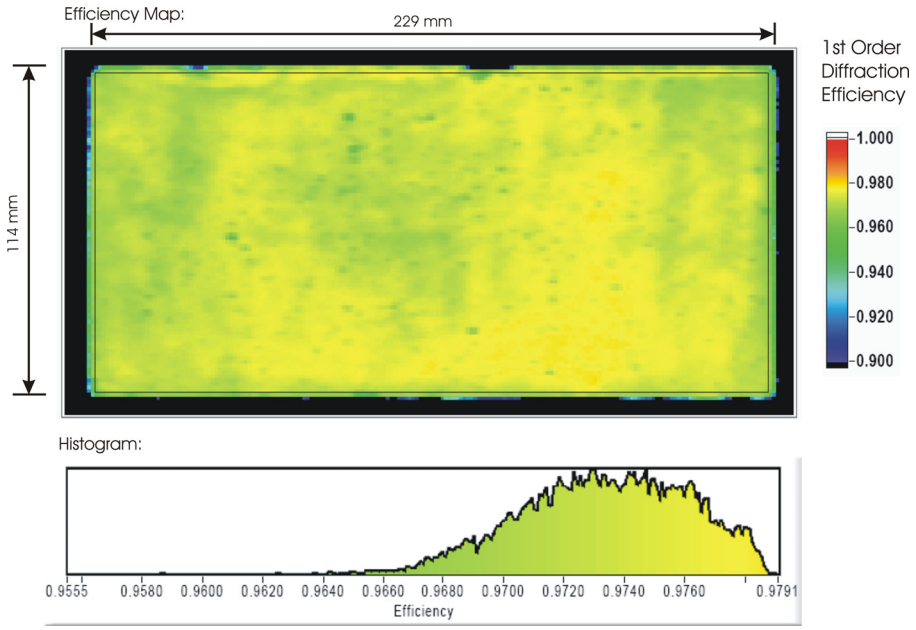

Figure 4.5 Map of the -1st order diffraction efficiency of a 229 mm x 114 mm grating measured at an operating angle of 38 degrees at a wavelength of 800 nm. The mean efficiency is 97.3% with a standard deviation of 0.3%. The histogram shows the distribution of diffraction efficiency over the entire grating area.

A diffraction efficiency of 97.3% with a standard deviation of 0.3% was measured across the full slab area. The mean diffraction efficiency remained above 96% for wavelengths between 820 nm and 780 nm. Figure 4.6 compares the measured diffraction efficiency with the design.

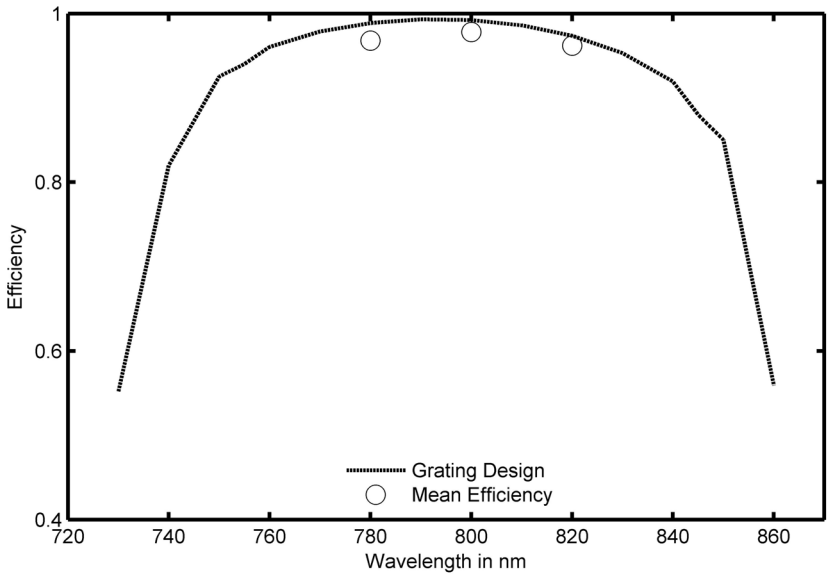

Figure 4.6 Diffraction efficiency of the -1st order of an 800 nm grating operating at 38 degrees: The line shows the design simulation of the diffracted light with a 270 nm groove depth. The circles are the measured mean efficiencies of the fabricated 229 mm x 114 mm grating.

The design has a large bandwidth acceptance of over 70 nm at 95% -1st order diffraction efficiency (>90 nm at 90% -1st order diffraction efficiency). The measured mean diffraction efficiencies show that the grating performs as expected, and furthermore, that the manufacturing process has high reproducibility. This is demonstrated in Table 4.1 which displays the measured mean diffraction efficiency values of the -1st order at λ= 800 nm for four different gratings.

	780 nm		800 nm		820 nm		Averaged Diffraction Efficiencies 780-820 nm
	Mean	RMS	Mean	RMS	Mean	RMS	
1	96.8	0.9	97.8	0.2	96.2	0.5	**96.9**
2	97.2	0.6	96.7	0.3	94.5	0.5	**96.1**
3	96.8	0.7	97.3	0.3	93.9	0.7	**96.0**
4	97.8	0.2	96.1	0.7	91.9	1.6	**95.3**

Table 4.1 Measured -1st order diffraction efficiencies for four different 229 mm x 114 mm gratings (%)

The values of the diffraction efficiency averaged over a 40 nm bandwidth centered at 800 nm are also shown.

4.5 Damage testing of the MLD high reflector and grating

The single-pulse laser damage threshold of the MLD interference coatings and of the completed grating were measured for different laser pulse lengths by adjusting the pulsewidth of a CPA 10 Hz Ti:Sapphire laser. The setup used for the damage threshold measurement is shown schematically in Figure 4.7.

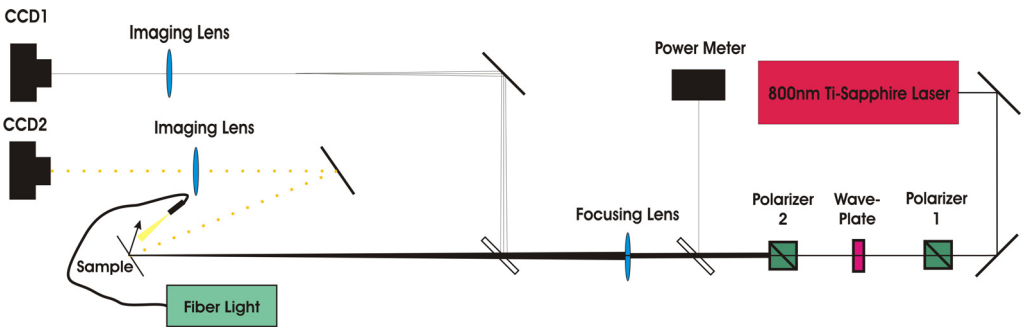

Figure 4.7 Schematic diagram of the setup used to determine damage threshold.

Two polarizing beam splitters and a waveplate were used to control the laser pulse energy. The samples were irradiated at an operating angle of 55 degrees with an S-polarized beam focused into a ~ 200 μm diameter spot by a 3 m focal length lens. The beam fluence on the sample was determined by simultaneously monitoring the intensity

profile and the laser pulse energy using a high transmission beam splitter. The energy of every shot was monitored with a Gentec TPM-300 power meter and the intensity profile was monitored by imaging the laser beam onto a CCD camera with a 100 mm focal length lens. To determine when damage occurs, the surface of the sample was monitored using a second imaging system composed of a 100 mm focal length imaging lens and a camera. The surface of the sample was illuminated with the light emanating from an optical fiber bundle to increasing the visibility of the irradiated area. The damage threshold of the multilayer coating was measured to decrease from 7 +/- 0.5 J/cm^2 for 120 ps pulses to 0.4 +/- 0.02 J/cm^2 for 120 fs pulses with a value of 0.87 +/- 0.2 J/cm^2 for 1 ps pulses.

Damage threshold measurements were also performed on the finished MLD grating structures using 50 mm diameter ridealong samples. The measured damage threshold using the S-polarized Ti:sapphire beam with an incident angle of 55 degrees varied from 1.76 +/- 0.1 J/cm^2, down to 0.18 +/- 0.02 J/cm^2 for pulsewidths ranging from 120 ps down to 120 fs respectively. Table 4.2 summarizes the results of the measurements. The damage threshold of the gratings for 1 ps pulses is ~2.4 times lower than that of the MLD interference coating. This is due to increased electric field at the edges of the grating ridges [8, 11].

	120 fs	1 ps	10 ps	120 ps
MLD Stack (J/cm^2)	**0.40 +/- 0.02**	**0.87 +/- 0.06**	**2.3 +/- 0.2**	**7.07 +/- 0.5**
MLD Grating (J/cm^2)	**0.18 +/- 0.02**	**0.37 +/- 0.02**	**0.74 +/- 0.04**	**1.76 +/- 0.1**

Table 4.2 Damage threshold of MLD stack and MLD gratings at 55 degrees

4.6 Pulse compression results

A set of four (229 mm x 114 mm) MLD gratings were used to setup a double pass vacuum compressor for the compression of 5.5 J pulses from a Ti:sapphire laser. The photograph displayed in Figure 4.8 shows a partial view of the compressor in which two of the gratings are visible.

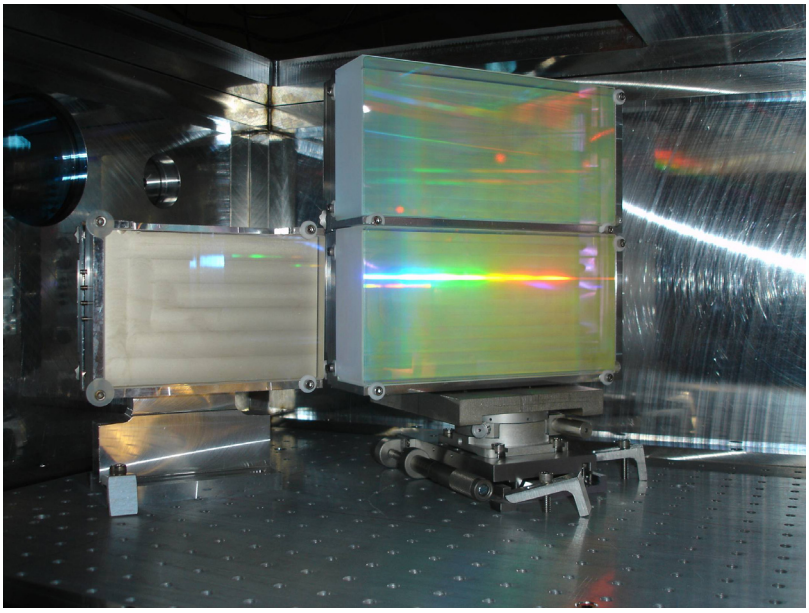

Figure 4.8 Photograph of two 229mm x 114 mm dielectric gratings that are part of a vacuum pulse compressor for high energy Ti:sapphire laser pulses.

The compressor was configured to compress 220 ps Ti:sapphire pulses that had been chirped by a grating stretcher implemented using a MLD grating produced in the same run. In this configuration the grating compressor has a bandwidth acceptance of 60 nm for a beam diameter of 96 mm. Although the measured spectral performance data shows the gratings will support the compression of 25 fs pulses, the separation of the gratings was set to generate pulses of 3-6 picosecond durations which are optimum for the excitation of transient collisional soft x-ray lasers in several elements [12-14]. The throughput of the compressor was measured to be greater than 80%. We have used the

gratings to compress input pulses of 5.5 J at repetition rates up to 2.5 Hz for several months without observing any grating degradation. Interferometry of the grating surface, subjected to several times this average fluence detected no measurable deformation, showing these MLD gratings are suited for high average power applications. This is in contrast with a previous setup that made use of gold coated replica gratings where we observed wavefront distortion due to thermal deformation at similar fluences. In another application we used smaller gratings made in the same fabrication process to compress pulses to pulsewidths below 70 fs, verifying that the MLD gratings have the bandwidth necessary for high average power femtosecond laser applications.

4.7 Conclusions

We have developed durable broad bandwidth high efficiency large area λ= 800 nm multilayer dielectric diffraction gratings for pulse compression of high energy Ti-Sapphire laser pulses at high average power. The MLD gratings have a mean efficiency that is better than 97% at the center wavelength and remains above 96% at wavelengths of 820 nm and 780 nm. The gratings were employed in the implementation of a high energy vacuum compressor with a throughput greater than 80%. The compressor was used to generate picosecond duration Ti:sapphire laser pulses with an energy ~ 4.5 J at a repetition rate of up to 2.5 Hz for several months without signs of degradation.

4.8 Acknowledgements

This work was supported by the NSF Center for Extreme Ultraviolet Science and Technology under NSF Award Number EEC-0310717 and the United States Department of Energy by the Lawrence Livermore National Laboratory under contract number DE-AC52-07NA27344.

4.8 References

1. E. B. Treacy, "Optical Pulse Compression With Diffraction Gratings," IEEE Journal of Quantum Electronics **5**, 454 (1969).
2. D. Strickland, and G. Mourou, "Compression of amplified chirped optical pulses," Optics Communications **55**, 219-221 (1985).
3. M. D. Perry, D. Pennington, B. C. Stuart, G. Tietbohl, J. A. Britten, C. Brown, S. Herman, B. Golick, M. Kartz, J. Miller, H. T. Powell, M. Vergino, and V. Yanovsky, "Petawatt laser pulses," Optics Letters **24**, 160-162 (1999).
4. C. B. Edwards, R. M. Allott, J. L. Collier, C. N. Danson, M. H. R. Hutchinson, D. Neely, and B. E. Wyborn, "Vulcan upgrade: a petawatt laser facility for experiments at 10^21 Wcm^-2," in *ECLIM 2000: 26th European Conference on Laser Interaction with Matter* (2001), pp. 63-69.
5. Y. Kitagawa, H. Fujita, R. Kodama, H. Yoshida, S. Matsuo, T. Jitsuno, T. Kawasaki, H. Kitamura, T. Kanabe, S. Sakabe, K. Shigemori, N. Miyanaga, and Y. Izawa, "Prepulse-Free Petawatt Laser for a Fast Ignitor," IEEE Journal of Quantum Electronics **40**, 281-293 (2004).
6. A. S. Svakhin, V. A. Sychugov, and A. E. Tikhomirov, "Efficient diffraction elements for TE-polarized waves," Soviet Physics - Technical Physics **36**, 1038-1040 (1991).
7. M. D. Perry, R. D. Boyd, J. A. Britten, D. Decker, B. W. Shore, C. Shannon, and E. Shults, "High-efficiency multilayer dielectric diffraction gratings," Optics Letters **20**, 940 (1995).

8. J. A. Britten, W. A. Molander, A. M. Komashko, and C. P. Barty, "Multilayer dielectric gratings for petawatt-class laser systems," in *Laser-Induced Damage in Optical Materials: 2003*, H. Guenther, N. Kaiser, K. L. Lewis, M. J. Soileau, and C. J. Stolz, eds. (SPIE, 2004), pp. 1-7.

9. F. Canova, O. Uteza, J. Chambaret, M. Flury, S. Tonchev, R. Fechner, and O. Parriaux, "High-efficiency, broad band, high-damage threshold high-index gratings for femtosecond pulse compression," Optics Express **15**, 15324-15334 (2007).

10. P. P. Lu, K.-X. Sun, R. L. Byer, J. A. Britten, H. T. Nguyen, J. D. Nissen, C. C. Larson, M. D. Aasen, T. C. Carlson, and C. R. Hoaglan, "Precise diffraction efficiency measurements of large-area greater-than-99%-efficient dielectric gratings at the Littrow angle," Optics Letters **34**, 1708-1710 (2009).

11. J. Neauport, E. Lavastre, G. Razé, G. Dupuy, N. Bonod, M. Balas, G. d. Villele, J. Flamand, S. Kaladgew, and F. Desserouer, "Effect of electric field on laser induced damage threshold of multilayer dielectric gratings," Optics Express **15**, 12508-12522 (2007).

12. J. J. Rocca, Y. Wang, M. A. Larotonda, B. M. Luther, M. Berrill, and D. Alessi, "Saturated 13.2 nm high repetition rate laser in Nickel-like Cd," Optics Letters **30**, 2581 (2005).

13. Y. Wang, M. A. Larotonda, B. M. Luther, D. Alessi, M. Berrill, V. N. Shlyaptsev, and J. J. Rocca, "Demonstration of saturated high repetition rate tabletop soft x-ray lasers at wavelength down to 13.9 nm," Physical Review A **72**, 053807 (2005).

14. B. M. Luther, Y. Wang, M. A. Larotonda, D. Alessi, M. Berrill, M. C. Marconi, J. J. Rocca, and V. N. Shlyaptsev, "Saturated high-repetition-rate 18.9-nm tabletop laser in nickellike molybdenum," Optics Letters **30**, 165-167 (2005).

CHAPTER 5

HIGH ENERGY 13.9 NM TABLE-TOP SOFT X-RAY LASER AT 2.5 HZ REPETITION RATE EXCITED BY A SLAB-PUMPED TI:SAPPHIRE LASER

Published in: Optics Letters, Vol. 35, Issue 10, pp. 1632-1634 © 2010 Optical Society of America

Author List: D. H. Martz, D. Alessi, B. M. Luther, Y. Wang, D. Kemp, M. Berrill and J. J. Rocca

Abstract: We have demonstrated repetitive operation of a table-top $\lambda = 13.9$ nm nickel-like Ag soft x-ray laser that generates laser pulses with 10 μJ energy. The soft x-ray laser is enabled by a Ti:Sapphire laser pumped by high repetition rate frequency-doubled high energy Nd:glass slab amplifiers. Soft x-ray laser operation at 2.5 Hz repetition rate resulted in 20 microwatt average power.

5.1 Introduction

There is significant interest in the table-top generation of high average power coherent soft x-ray (SXR) radiation for applications. Powerful optical pump lasers have been used to generate ps duration SXR lasers in the 13 nm spectral region with energies of ~10-25 μJ at a rate of one shot every several minutes [1, 2]. Recently high repetition rate table-top SXR lasers in this spectral range have reached energies up to ~1.5 μJ when pumped by 5-10 Hz rep. rate optical lasers [3-5]. These SXR lasers have been

successfully used as the light source for table-top broad area microscopes with resolutions down to 38nm [6, 7]. This and other applications can significantly benefit from table-top SXR laser sources with higher average power.

In this Letter we report a significant increase in the pulse energy of multi-Hz table top SXR lasers in the 13 nm spectral region utilizing a newly developed Ti:Sapphire pump laser system driven by the frequency-doubled output of Nd:glass zig-zag slab amplifiers. Using this pump laser we have demonstrated $\lambda = 13.9$ nm laser pulses with maximum energies above 10 μJ. Operation of this SXR laser at 2.5 Hz rep. rate resulted in average power up to 20 μW and a 7% pulse energy fluctuation.

5.2 Laser System

The SXR laser pulses were generated in a Ag plasma created and heated by a sequence of pulses from a chirped pulse amplification (CPA) Ti:Sapph system comprising a mode-locked oscillator and three multi-pass amplifiers. The 3rd amplification stage is pumped by up to 20 J of 527 nm light from the frequency-doubled output of a Nd:glass zig-zag slab laser developed in house. This dual-arm pump laser configuration (Figure 5.1) was designed to operate at rep. rates of several Hz. It has long been recognized that the slab geometry has advantages that can overcome some of the limitations imposed by the more commonly used rod configuration [8, 9]. The optical propagation along a zig-zag path, confined to the slab by total internal reflection, eliminates 1st-order thermal and stress induced focusing. It also reduces stress induced birefringence and allows for high rep. rate, high average power operation limited only by stress induced fracture of the laser glass [10].

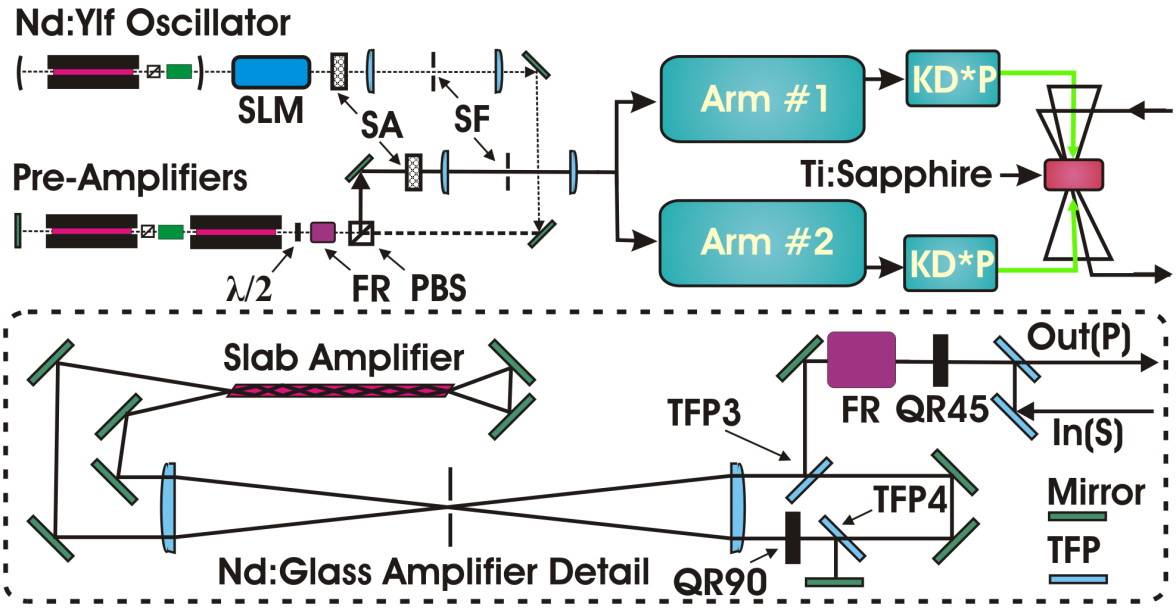

Figure 5.1 Top: Block diagram of the 3rd amplification stage of the Ti:Sapph pump laser system and associated slab amplifier laser system. Bottom: Schematic diagram of the 8-pass Nd:glass slab amplifier.

The slab geometry has been previously used to amplify ns pulses to energies up to 25 J [11, 12]. More recently, a ps CPA laser based on Nd:glass slab amplifiers has been used to pump SXR lasers at a rep. rate of 0.1 Hz producing pulse energies up to ~1 μJ [13, 14].

In our Ti:Sapph laser system, pulses from a Kerr lens mode-locked oscillator are stretched to 210 ps FWHM with a grating stretcher. The first two amplifier stages are pumped by a commercial 10Hz frequency-doubled 800 mJ Q-switched Nd:YAG laser, resulting in 800 nm laser pulses with ~200 mJ energy, and the 3rd multi-pass amplifier is pumped by the Nd:glass slab amplifiers. The front end of the slab laser consists of a Q-switched 1053 nm Nd:YLF oscillator that produces 1 mJ pulses of ~19 ns FWHM at 5 Hz rep. rate. The pulses from the oscillator are directed through an active liquid crystal spatial light modulator (SLM) and are relay imaged onto a serrated aperture (SA) and then spatially filtered to produce a beam with a super-Gaussian intensity profile. The beam is then imaged into a pre-amplifier consisting of two 7 mm dia. Nd:YLF rods

arranged in a double-pass configuration to obtain pulse energies of ~120 mJ. The double pass is accomplished by using a polarizing beam splitter (PBS) cube, a Faraday rotator (FR) and a half waveplate (λ/2) combination. The output of the pre-amplifier is imaged onto a 2nd SA and spatial filter (SF) pair to obtain a flat-top beam profile. This profile is relay imaged throughout the rest of the system. The beam is subsequently stretched onto an oval of 8 x 120 mm^2 dimension through a pair of cylindrical anamorphic imaging telescopes (not shown in Figure 5.1) to conform to the 10 x 140 mm^2 cross section of the slab amplifiers. The resulting beam is split into two identical arms by a 50% beam splitter and each beam is amplified by 8 passes through the 400mm long slab amplifiers. The slabs are pumped by four Xe flashlamps which are driven with a 300 μs electrical pulse depositing ~700 J of electrical energy per lamp. Each arm operates in the following fashion. The input (S polarized) beam reflects off a thin film polarizer (TFP) pair and travels through a 45 deg. quartz rotator (QR45)/FR combination. The beam remains S pol. and is then injected into an 8-pass amplifier cavity by a 3rd TFP (TFP3). Using a relay imaging telescope the pulses are directed into the slab for two passes of amplification. The same telescope images the beam back through a 90 deg. quartz rotator (QR90) changing the polarization to P, resulting in transmission through TFP4. The beam is then re-injected along the path of the input beam (passing through TFP3) for an additional 2 passes through the slab. After a total of 4 passes the beam again passes through QR90 restoring the polarization to S thereby causing it to be ejected by TFP4 to a normal incidence mirror. The mirror directs the beam back upon itself reversing the process for a total of eight passes before being sent back through the QR45/FR pair resulting in P pol. and ejection by the input TFP.

Each slab amplifier arm generates pulses with an energy of up to 18 J that are frequency doubled in a pair of KD*P crystals to produce up to 10J of λ = 527 nm light in each arm.

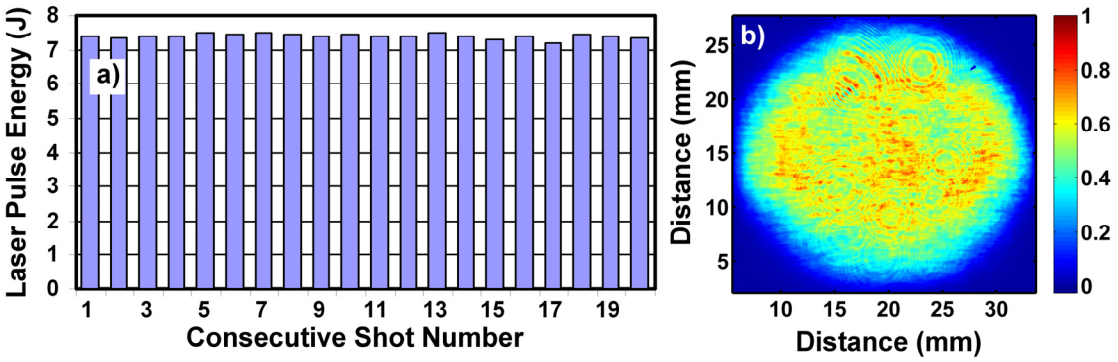

Figure 5.2 (a) Shot to shot variation of amplified λ = 800 nm Ti:Sapph laser pulse energy measured at 1Hz rep. rate. The average laser pulse energy is 7.4 J and the standard deviation σ = 1%. (b) Typical intensity profile of the amplified λ = 800 nm beam.

Both beams are reshaped to 30 mm dia. and imaged into the 30 mm thick 3rd stage Ti:Sapph amplifier rod. A near flat-top pump beam is achieved by adjusting the input beam's intensity profile using the SLM. Three-pass amplification of the λ = 800 nm 200mJ laser pulses through the 3rd stage Ti:Sapph amplifier produce pulse energies up to 7.5 J at 2.5 Hz rep. rate with a typical spatial profile shown in Figure 5.2b. Figure 5.2a shows a series of consecutive shots acquired while operating the amplifier at 1 Hz rep. rate. The shot to shot energy variation was measured to be ~ 1%.

5.3 Soft X-Ray Generation

The λ = 13.9 nm Ni-like Ag SXR laser was pumped focusing 4.9 J of total Ti:Sapph laser energy onto a ~30 μm FWHM wide, 6.3 mm FWHM long line on the surface of a polished 8x40mm^2 Ag slab target. The beam was split to create 210 ps pre-

pulses with an energy of ~2.2 J that were directed at normal incidence onto the target to create a plasma with a large fraction of Ni-like Ag ions (Ag^{+19}). The remaining energy was directed into a vacuum grating compressor using recently developed high efficiency 800 nm dielectric gratings [15], producing 6 ps 2.7 J pulses. The plasma was allowed to expand to smooth the density gradient and was subsequently rapidly heated by the 6 ps pulse impinging at 23 deg. grazing incidence. This inherently traveling wave pumping geometry takes advantage of the refraction of the pump beam in the electron density gradient of the pre-created plasma to efficiently deposit energy into a plasma density region with optimum conditions for amplification [16, 17]. The electron density in this region of the plasma is ~ 2.6×10^{20} cm^{-3}. The plasma is then rapidly heated to electron temperatures of up to ~550 eV resulting in a transient population inversion that amplifies the λ = 13.9 nm $4d^1S_0 \rightarrow 4p^1P_1$ transition of Ni-like Ag into saturation. The highly monochromatic SXR laser output (Figure 5.3a & 5.3b) was monitored using the combination of a flat field spectrometer and a back-illuminated CCD detector. Five Zr filters with parylene support with a combined thickness of 2.3μm were used to attenuate the SXR laser beam. The transmissivity of the combined set of filters was measured to be 1.4×10^{-4} using a beamline of the ALS synchrotron at Berkeley.

SXR laser pulses with an energy exceeding 10 μJ were generated at 0.5 Hz rep. rate (Figure 5.3c). When operating the SXR laser at 2.5 Hz rep. rate the average power reached 20 μW, the highest reported to date for a table-top SXR laser operating in the 13 nm spectral region. Figure 5.3d shows the shot-to-shot output pulse energy variation of the SXR laser when operated at 2.5 Hz. The average pulse energy of this series of shots is 7.4 μJ with a standard deviation of 7%. This relatively good stability is the result of

operating the SXR amplifier in a highly saturated regime. However, during day to day operation we measured average powers up to 20 μW with a standard deviation of 12%.

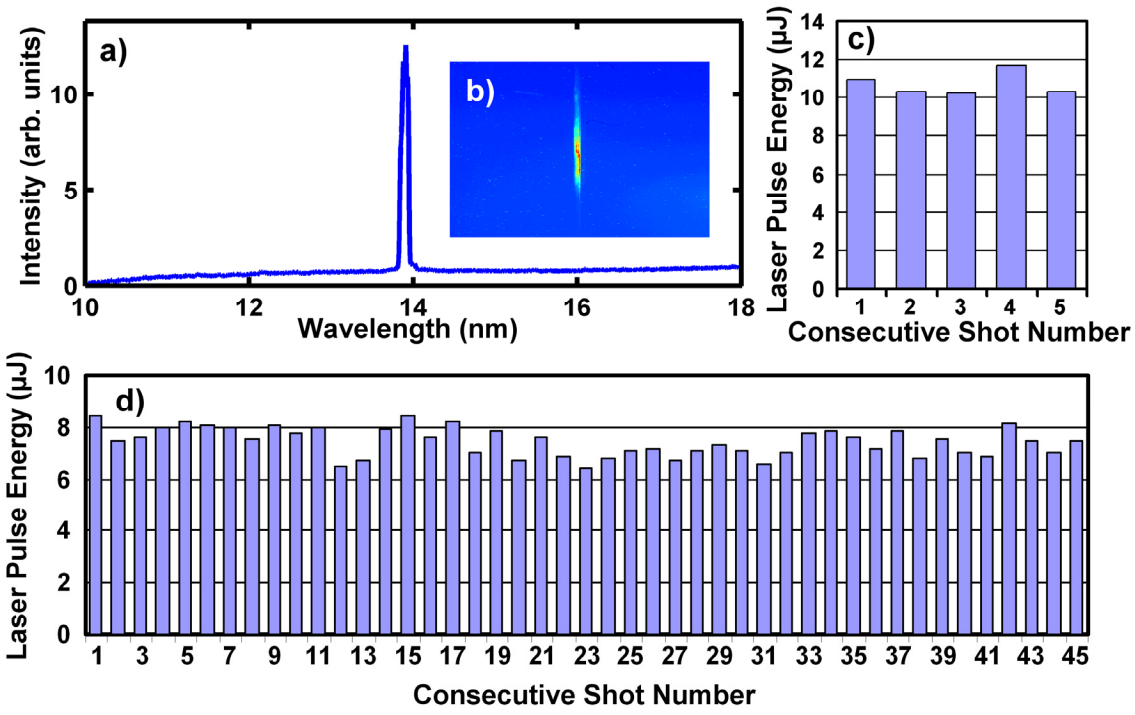

Figure 5.3 (a) Spectra of the Ni-like Ag plasma amplifier showing highly monochromatic laser emission at λ = 13.9 nm. (b) Spectrally resolved CCD image of the laser output. (c) Laser output pulse energy of the λ = 13.9 nm laser operating at 0.5 Hz and (d) 2.5 Hz SXR laser operation with an average energy of 7.4 μJ with a shot-to-shot laser pulse energy variation of σ = 7%.

The larger shot to shot variation respect to that of the pump is likely to be due to the stability of the alignment of the pre-pulse and the short pulse line focuses. The full angle beam divergence was measured to be 9.8±0.5 mrad FWHM perpendicular to the target surface and 8.8±0.5 mrad FWHM parallel to the target surface. The spatial coherence is expected to be similar to that reported in [18]. The SXR amplifier can be used to obtain pulses with full spatial and temporal coherence employing the injection seeding technique demonstrated in [19]. The SXR laser pulse duration is expected to be similar to

that we previously measured for a transient 13.9 nm Ag laser excited at the same grazing incidence angle, ~ 5 ps [20]. Increasing the rep. rate to the design maximum of 5 Hz by compensating for 2nd order lensing effects in the slab laser can be expected to further increase the SXR laser average power. This table-top pump laser system was also used to create several μW of λ = 13.2 nm radiation from a Ni-like Cd SXR laser that enabled at-wavelength line-edge roughness measurements of patterned extreme ultraviolet lithography masks on a table-top [21].

5.4 Conclusions

In conclusion we have demonstrated a table-top λ = 13.9 nm SXR laser that produces pulse energies above 10 uJ. Operation at 2.5Hz rep. rate produced an average power of ~20 μW. High rep. rate operation of this laser is enabled by a newly developed Nd:glass zig-zag slab pump laser that is capable of pumping a high energy Ti:Sapphire amplifier at a rep. rate of several Hz with high shot to shot stability and good beam quality. This laser will make possible new applications of coherent SXR light requiring high average power on a table-top.

5.5 Acknowledgements

This work was supported by the Engineering Research Centers Program of the National Science Foundation under Award EEC-0310717.

5.6 References

1. J. Dunn, Y. Li, A. L. Osterheld, J. Nilsen, J. R. Hunter, and V. N. Shlyaptsev, "Gain Saturation Regime for Laser-Driven Tabletop, Transient Ni-Like Ion X-Ray Lasers," Physical Review Letters **84**, 4834–4837 (2000).
2. T. Kawachi, M. Kado, M. Tanaka, A. Sasaki, N. Hasegawa, A. V. Kilpio, S. Namba, K. Nagashima, P. Lu, K. Takahashi, H. Tang, R. Tai, M. Kishimoto, M. Koike, H. Daido, and Y. Kato, "Gain saturation of nickel-like silver and tin x-ray lasers by use of a tabletop pumping laser system," Physical Review A **66**, 033815 (2002).
3. J. J. Rocca, Y. Wang, M. A. Larotonda, B. M. Luther, M. Berrill, and D. Alessi, "Saturated 13.2 nm high repetition rate laser in Nickel-like Cd," Optics Letters **30**, 2581-2583 (2005).
4. Y. Wang, M. A. Larotonda, B. M. Luther, D. Alessi, M. Berrill, V. N. Shlyaptsev, and J. J. Rocca, "Demonstration of saturated high repetition rate tabletop soft x-ray lasers at wavelength down to 13.9 nm," Physical Review A **72**, 053807 (2005).
5. H. T. Kim, I. W. Choi, N. Hafz, J. H. Sung, T. J. Yu, K. H. Hong, T. M. Jeong, Y. C. Noh, D. K. Ko, K. A. Janulewicz, J. Tümmler, P. V. Nickles, W. Sandner, and J. Lee, "Demonstration of a saturated Ni-like Ag x-ray laser pumped by a single profiled laser pulse from a 10-Hz Ti:sapphire laser system," Physical Review A **77**, 023807 (2008).
6. G. Vaschenko, C. Brewer, F. Brizuela, Y. Wang, M. A. Larotonda, B. M. Luther, M. C. Marconi, J. J. Rocca, C. S. Menoni, E. H. Anderson, W. Chao, B. D.

Harteneck, J. A. Liddle, Y. Liu, and D. T. Attwood, "Sub-38 nm resolution tabletop microscopy with 13 nm wavelength laser light," Optics Letters **31**, 1214-1216 (2006).

7. F. Brizuela, Y. Wang, C. A. Brewer, F. Pedaci, W. Chao, E. H. Anderson, Y. Liu, K. A. Goldberg, P. Naulleau, P. Wachulak, M. C. Marconi, D. T. Attwood, J. J. Rocca, and C. S. Menoni, "Microscopy of extreme ultraviolet lithography masks with 13.2 nm tabletop laser illumination," Optics Letters **34**, 271-273 (2009).
8. W. S. Martin and J. P. Chernoch, "Multiple Internal Reflection Face-Pumped Laser," U.S. Patent 3,633,126 (January 4 1972).
9. J. Eggleston, T. Kane, K. Kuhn, J. Unternahrer, and R. Byer, "The slab geometry laser--Part I: Theory," IEEE Journal of Quantum Electronics **20**, 289-301 (1984).
10. T. Kane, J. Eggleston, and R. Byer, "The slab geometry laser-II: Thermal effects in a finite slab," IEEE Journal of Quantum Electronics **21**, 1195-1210 (1985).
11. C. B. Dane, L. E. Zapata, W. A. Neuman, M. A. Norton, and L. A. Hackel, "Design and operation of a 150 W near diffraction-limited laser amplifier with SBS wavefront correction," IEEE Journal of Quantum Electronics **31**, 148-163 (1995).
12. M. J. Shoup, J. H. Kelly, and D. L. Smith, "Design and testing of a large-aperture, high-gain, Brewster's angle zigzag Nd:glass slab amplifier," Applied Optics **36**, 5827-5838 (1997).
13. Y. Ochi, N. Hasegawa, T. Kawachi, and K. Nagashima, "Development of a chirped pulse amplification laser with zigzag slab Nd:glass amplifiers dedicated to x-ray laser research," Applied Optics **46**, 1500-1506 (2007).

14. Y. Ochi, T. Kawachi, N. Hasegawa, M. Nishikino, T. Ohba, M. Tanaka, M. Kishimoto, T. Kaihori, K. Nagashima, and A. Sugiyama, "Demonstration of SubmicroJoule, Spatially Coherent Soft-X-ray Laser Pumped by 0.1 Hertz, 10 Joule, Picosecond Laser," Jpn. J. Appl. Phys. **48**, 120212 (2009).

15. D. H. Martz, H. T. Nguyen, D. Patel, J. A. Britten, D. Alessi, E. Krous, Y. Wang, M. A. Larotonda, J. George, B. Knollenberg, B. M. Luther, J. J. Rocca, and C. S. Menoni, "Large area high efficiency broad bandwidth 800 nm dielectric gratings for high energy laser pulse compression," Optics Express **17**, 23809-23816 (2009).

16. R. Keenan, J. Dunn, P. K. Patel, D. F. Price, R. F. Smith, and V. N. Shlyaptsev, "High-Repetition-Rate Grazing-Incidence Pumped X-Ray Laser Operating at 18.9 nm," Physical Review Letters **94**, 103901 (2005).

17. B. M. Luther, Y. Wang, M. A. Larotonda, D. Alessi, M. Berrill, M. C. Marconi, J. J. Rocca, and V. N. Shlyaptsev, "Saturated high-repetition-rate 18.9-nm tabletop laser in nickellike molybdenum," Optics Letters **30**, 165-167 (2005).

18. Y. Liu, Y. Wang, M. A. Larotonda, B. M. Luther, J. J. Rocca, and D. T. Attwood, "Spatial coherence measurements of a 13.2 nm transient nickel-like cadmium soft x-ray laser pumped at grazing incidence," Optics Express **14**, 12872-12879 (2006).

19. Y. Wang, E. Granados, F. Pedaci, D. Alessi, B. Luther, M. Berrill, and J. J. Rocca, "Phase-coherent, injection-seeded, table-top soft-X-ray lasers at 18.9 nm and 13.9 nm," Nature Photonics **2**, 94-98 (2008).

20. M. A. Larotonda, Y. Wang, M. Berrill, B. M. Luther, J. J. Rocca, M. M. Shakya, S. Gilbertson, and Z. Chang, "Pulse duration measurements of grazing-incidence-pumped high repetition rate Ni-like Ag and Cd transient soft x-ray lasers," Optics Letters **31**, 3043-3045 (2006).

21. C. Menoni, F. Brizuela, Y. Wang, D. Alessi, S. Carbajo, B. Luther, A. Sakdinawat, W. Chao, Y. Liu, E. Anderson, K. Goldberg, D. Attwood, M. Marconi, and J. Rocca, "First At-Wavelength Defect Characterization of EUV Lithography Reticles Using a Table-Top Laser," in *International Symposium on Extreme Ultraviolet Lithography,* (Prague, Czech Republic, 2009).

CHAPTER 6

APPLICATIONS OF THE HIGH ENERGY TI-SAPPHIRE LASER TO EUV LASER SCIENCE

6.1 Further Experiments Conducted at Colorado State University

Following the completion and successful operation of the high energy chirped pulse amplification Ti-Sapphire extreme ultraviolet (EUV) pump laser, experiments have been conducted utilizing the new capabilities. Working with other research scientists at Colorado State University it was possible to make further advancements in EUV laser science.

We have realized the first demonstration of a table-top aerial imaging metrology system utilizing 1 Hz operation of the 13.2 nm Ni-like Cd laser [1]. This imaging application demonstrates the ability to characterize pattern and defect printability in Mo/Si extreme ultraviolet lithography (EUVL) masks. Because the system imitates a EUVL stepper, results of line-edge roughness measurements on a EUVL mask have the potential to gain significant industrial interest.

Improvement in beam quality and scaling to shorter wavelengths is also of interest for the advancement of EUV lasers. Two papers are presented in this chapter discussing the seeded operation of the Ni-like 13.9 nm Ag laser as well as further scaling of saturated operation of the table-top Ni-like Te laser operating at 10.9 nm.

6.2 Improved Beam Characteristics of Solid-Target Soft X-Ray Laser Amplifiers by Injection-Seeding with High Harmonic Pulses

Published in: Optics Letters, Vol. 35, Issue 14, pp. 2317-2319 © 2010 Optical Society of America

Author List: M. Berrill, D. Alessi, Y. Wang, S.R. Domingue, D.H. Martz, B. M. Luther, Y. Liu, and J.J. Rocca

Abstract: Injection-seeding of solid-target soft x-ray laser amplifiers with high harmonic pulses is shown to dramatically improve the far-field laser beam profile and reduce the beam divergence. Measurements and 2-dimensional simulations for a 13.9 nm nickel-like Ag amplifier show that the amplified beam divergence depends strongly on the seed, and can therefore be controlled by selecting the divergence of the seed. The near-field beam size of both the seeded and unseeded lasers is shown to be determined by the size of the gain region and the divergence of the amplified beams.

6.2.1 Introduction

High average power table-top soft x-ray (SXR) laser beams at wavelengths between 10 and 30 nm have been generated by optical laser excitation of solid targets [2-6]. However, the beams produced by these amplifiers are characterized by relatively large beam divergence (5-15 mrad) [2-6], highly speckled patterns (Fig 1a and Ref. [7]), and limited spatial [8] and temporal coherence [9]. Previous work by Tanaka et al. demonstrated a significantly reduced far-field divergence and increased spatial coherence using an injection technique scheme that makes use of two soft x-ray plasma amplifiers [10]. Injection-seeding of SXR amplifiers with high harmonic (HH) pulses is a promising

technique for improving the characteristics of SXR lasers that has additional advantages [11-16]. In addition to a reduced beam divergence and providing full spatial coherence [13], this technique can generate intense SXR laser pulses with full temporal coherence [16], shorter pulsewidth [16], and defined polarization [11]. The seeding of broad bandwidth solid-target SXR laser amplifiers with HH pulses has the potential of generating femtosecond SXR laser pulses [11, 16]. Herein we report the results of the characterization of the near-field and far-field patterns of a seeded 13.9 nm solid target amplifier that show that injection-seeding dramatically decreases the beam divergence and results in a nearly Gaussian far-field profile (Figure 6.1b). The far field divergence is shown to be strongly dependent on that of the initial HH seed, and can therefore be tailored by selecting the divergence of the seed. The near field beam size of both the seeded and unseeded amplifiers is shown to depend on the size of the gain region and the beam divergence.

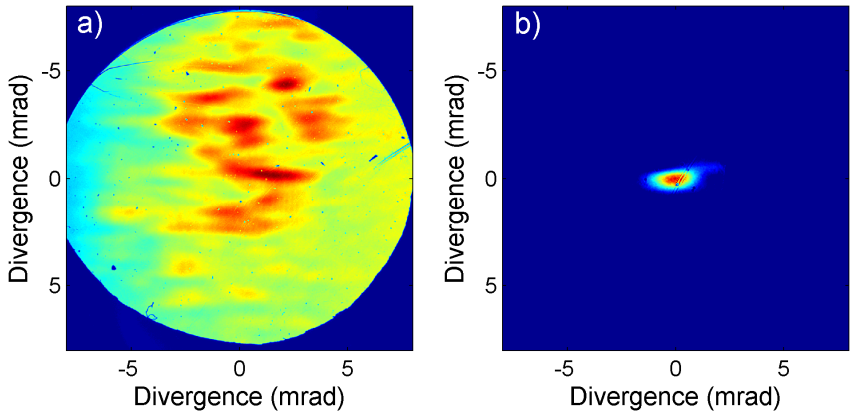

Figure 6.1 Comparison of the far-field from an un-seeded 13.9 nm Ni-like Ag amplifier (a), and of the same amplifier seeded by high harmonic pulses (b). Injection-seeding results in a ~10X decrease of the beam divergence. The circular aperture in (a) is from a filter frame.

6.2.2 Experimental Setup and Simulation

The experiments were conducted with a nickel-like Ag SXR laser amplifier excited using pump conditions similar to those described in [15]. A 815 nm Ti:sapphire laser was used to create a sequence of pump pulses consisting of a 10 mJ pre-pulse of 120 ps duration, followed after about 5 ns by a second ~350 mJ pre-pulse impinging at normal incidence, which in turn was followed after 200 ps by a ~0.9 J heating pulse of 6.7 ps duration impinging at a grazing incidence angle of 23 degrees. The pump pulses were focused onto the target to form a 30 μm x 4.1 mm FWHM long line. The length of the target was 3 mm. A small portion of the pump laser energy (~ 20 mJ) was split, compressed in a separate pulse compressor, and focused into a Ne gas jet with a f =1.2 m lens to produce 59^{th} seed pulses. The output of the gas jet was relay imaged onto a ~100 μm diameter spot at the input of the plasma amplifier using a gold-coated toroidal mirror designed to operate at a grazing incidence angle of 10 degrees.

The plasma amplifier was simulated using a 2D hydrodynamic plasma model developed in-house. The left column in Figure 6.2 shows the evolution of the main plasma properties as a function of distance from the target, and the right column shows the 2D spatial distribution of the electron density, electron temperature, and small signal gain at the time delay of 202 ps after the peak of the main prepulse. The prepulse is computed to heat the plasma to ~90 eV, resulting in a degree of ionization of ~18 at the time of arrival of the short pulse. The short pulse rapidly heats the plasma to ~400 eV in the region where the electron density is 2-3 x 10^{20} cm^{-3}, resulting in a small-signal gain coefficient of ~80 cm^{-1} at 35 μm from the target surface. These results were then fed into a 3D ray-trace post processor code that can compute beam profiles for direct comparison

with the experiments. This code fully treats saturation effects by solving the atomic rate equations with stimulated emission at each point along the SXR amplifier.

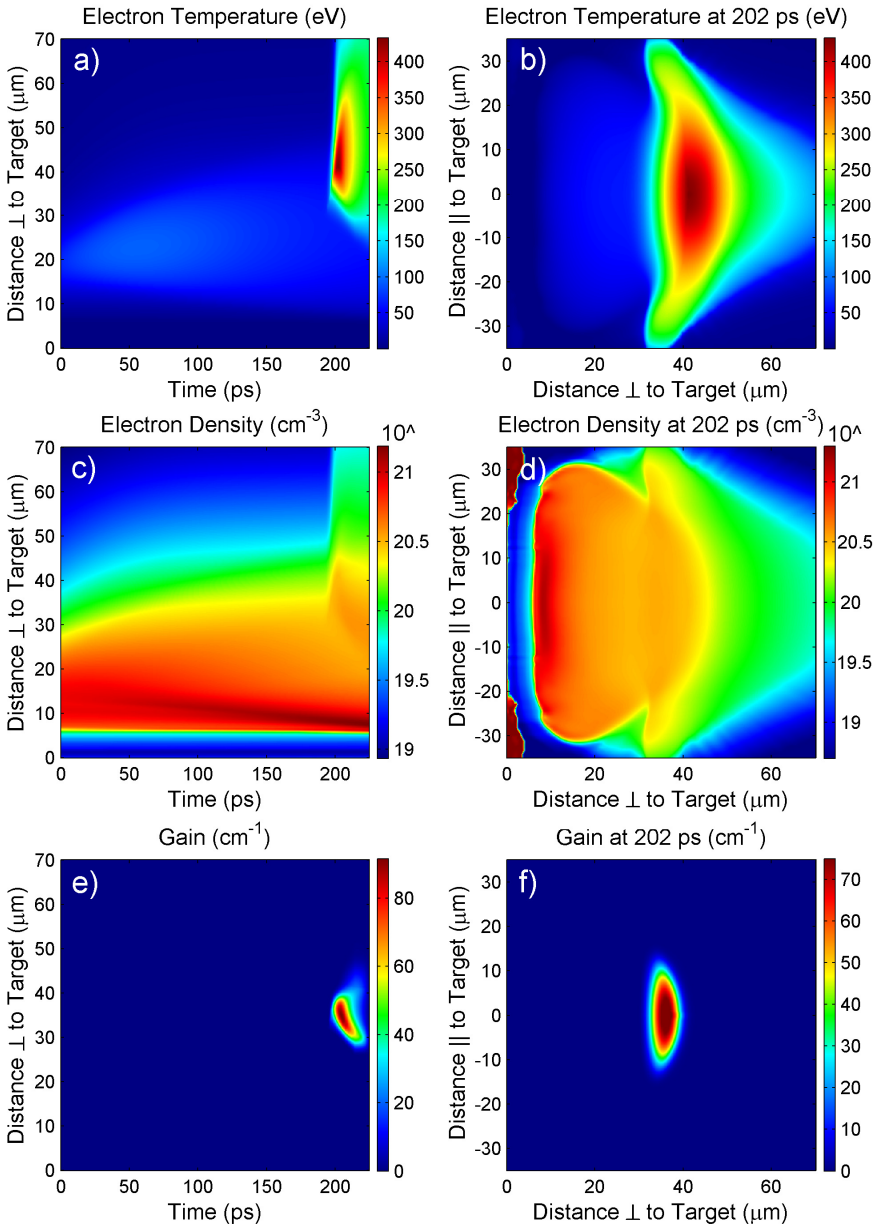

Figure 6.2 - Simulated plasma characteristics and gain distribution of a 13.9 nm soft x-ray laser plasma amplifier. The excitation conditions are those described in the text.

6.2.3 Results

The far-field beam pattern was recorded by placing a back-thinned CCD detector at 0.86 m from the plasma. Two 0.3 μm thick Zr filters with parylene support were used to filter visible light and attenuate the SXR lasers. Laser experiments were conducted using two different seed pulse divergences to study the dependence of the amplified beam on the seed. A comparison with the simulated far-field beam profiles for the two cases is illustrated in Figure 6.3 along with the corresponding profile of the HH seed. When a HH seed pulse with a FWHM divergence of 0.5±0.03 x 0.7±0.04 mrad in the directions perpendicular and parallel to the target respectively was used to seed the plasma, an amplified pulse with a divergence of 1.4±0.14 x 0.7±0.07 mrad was measured to result (Figure 6.3c). Simulations agree in showing that the divergence of the amplified beam in the direction parallel to the target surface closely resembles that of the seed beam, while the divergence perpendicular to the target surface is larger due to refraction**.** When the divergence of the HH seed was increased to 1.6±0.3 x 1.4±0.4 mrad, an amplified pulse with a divergence of 1.5±0.08 x 1.2±0.15 mrad was measured (Figure 6.3d). The results show that when the divergence of the input HH seed is larger than ~1 mrad the far field of the amplified seed is almost completely dominated by the seed, while for smaller divergences it is controlled by both the input seed and refraction. These beam divergences are nearly an order of magnitude smaller than those corresponding to the unseeded amplifier (Figure 6.1).

The near-field beam pattern was recorded by projecting the exit plane of the amplifier onto the CCD with 15.2X magnification using the combination of a concave (R=0.5 m) mirror and a flat Mo-Si multilayer mirror placed on a Z-fold configuration. A

pinhole was placed in front of the imaging mirror to help discriminate the seeded beam from the amplified spontaneous emission (ASE). Figure 6.4 compares the measured near-field profiles of the unseeded and seeded beams.

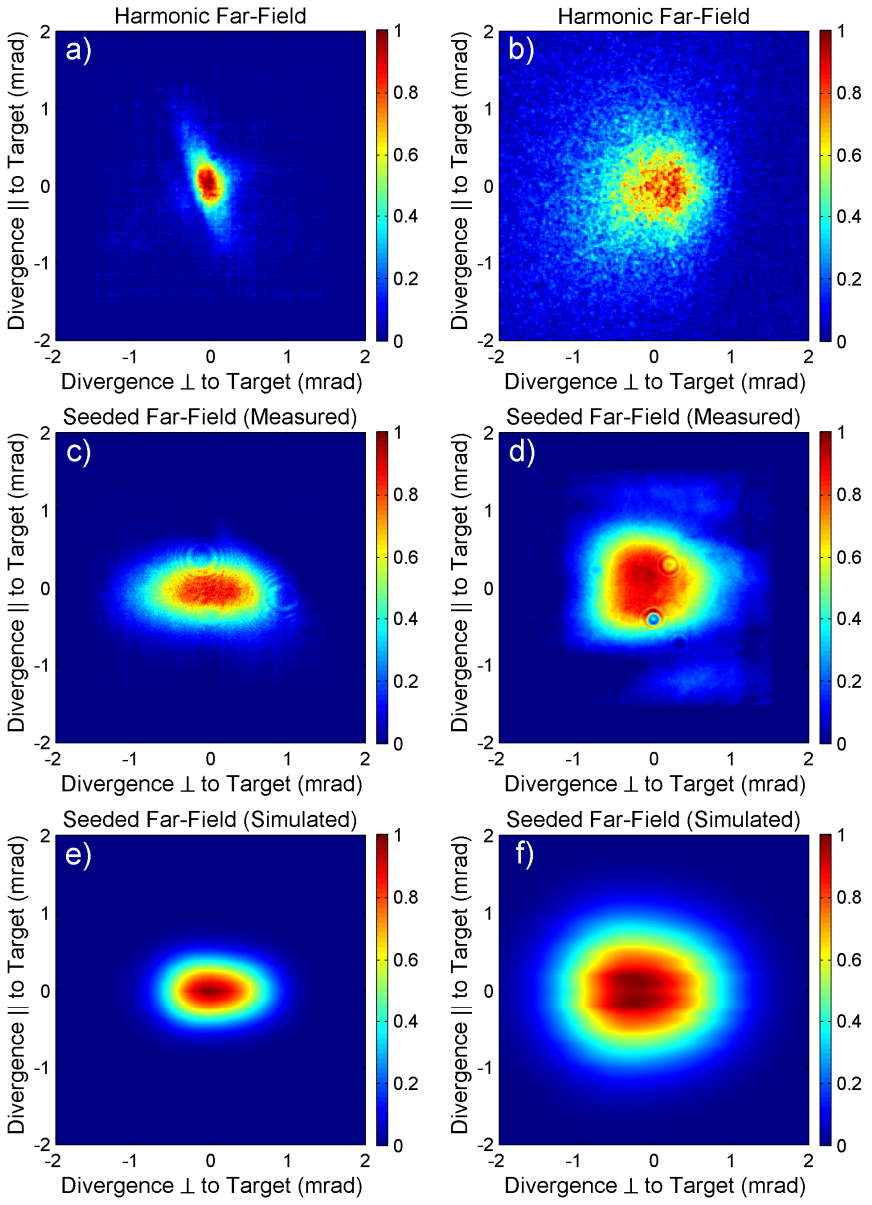

Figure 6.3 - Comparison of far-field profiles of : a) and b) measured high harmonic seeds with two different divergences; c) and d) corresponding measured seeded laser beams; and e) and f) simulated seeded laser beams.

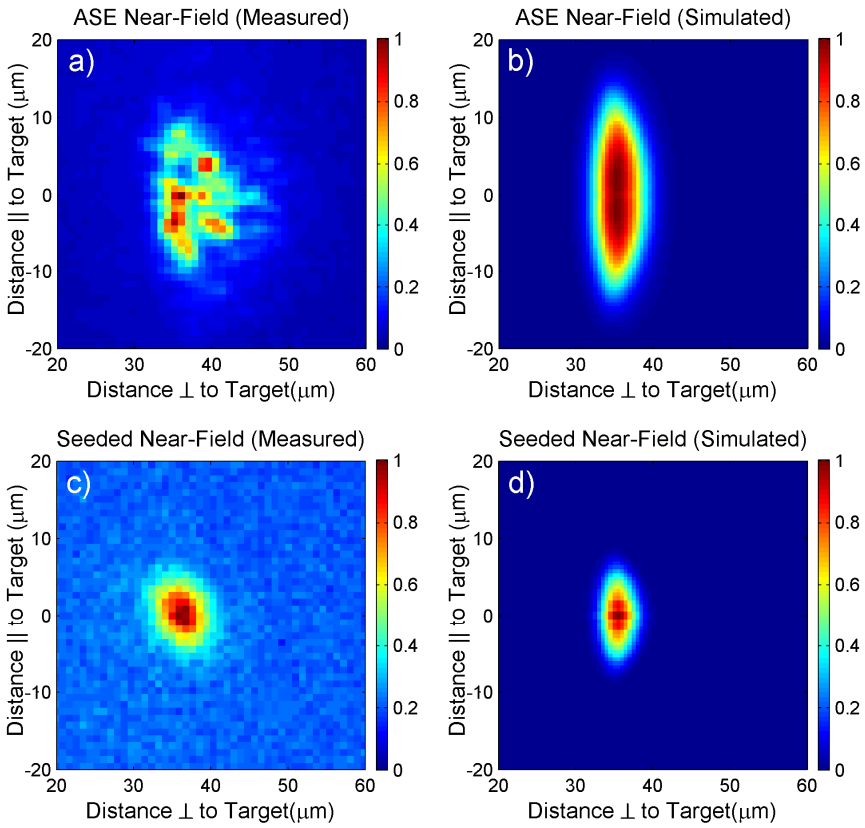

Figure 6.4 - Measured and simulated near-field beam profiles for the ASE and seeded lasers.

The location of the center of the near-field beam spot with respect to the target surface (Figure 6.4a, 6.4c) is dominantly determined by the position of the peak of the gain (~35 μm from the target in Figure 6.2f), and was measured to be at a distance of 33±4 μm in good agreement with the simulated near field profile (Figure 6.4b, 6.4d). Model simulations show that the location of the gain is in turn dependent on the early pre-pulse that is responsible for creating the initial plasma profile, and that the absence of this pre-pulse shifts the gain closer to the target surface (to a distance of ~15 μm). As the seed propagates through the plasma amplifier, its intensity quickly saturates, yielding a near field profile that is dominantly determined by the spatial distribution of the saturation fluence integrated over the amplifier length. The measured near-field size of the unseeded

ASE laser (Figure 6.4a) is characterized by a full-width at half maximum of 11.3±4 x 13.3±3 μm in the directions perpendicular and parallel to the target surface respectively. The measured size of the seeded laser beam (Figure 6.4c) is smaller, 6.0±0.6 x 8.3±1.5 μm. The larger near-field spot size of the ASE laser in the direction parallel to the target surface is due to the larger divergence of the ASE laser, which allows rays with different trajectories to amplify across the entire gain region. By contrast the narrow divergence of the HH seed causes all the rays to effectively take similar paths, resulting in a narrower beam profile. This size difference is enhanced in the direction parallel to the target surface due to the larger gain size, and to the fact that the seeded beam is more sensitive to refraction caused by the electron density profile of the plasma amplifier (Figure 6.2d) which acts as a weak negative lens. It should be noticed that the simulation results shown in Figure 6.4 assume a perfect overlap between the laser pulses. Computations show that a 10 μm misalignment causes the gain region and resulting near-field beam size to decrease by ~20% in the direction parallel to the target surface.

6.2.4 Conclusions

In conclusion, we have characterized for the first time the near-field and far-field distributions of an injection-seeded solid target SXR laser amplifier with experiments and 2-dimensional simulations. Seeding is shown to reduce the far field divergence by an order of magnitude and to allow for control of the far-field beam characteristics by tailoring the divergence of the seed.

6.2.5 Acknowledgements

This work was supported by the NSF Center for Extreme Ultraviolet Science and Technology under NSF Award No. EEC-0310717, and by the Chemical Sciences, Geosciences and Biosciences Division, Office of Basic Energy Sciences, Office of Science, U.S. Department of Energy, using a facility initially made possible with the support of the W.M. Keck foundation. M.B. acknowledges support from DOE CSGF under Grant No. DE-FG02-97ER25308.

6.3 1 Hz Operation of a Gain-Saturated 10.9 nm Table-Top Laser in Nickel-Like Te

Published in: Optics Letters, Vol. 35, Issue 3, pp. 414-416 © 2010 Optical Society of America

Author List: D. Alessi, D. H. Martz, Y. Wang, M. Berrill, B. M. Luther and J. J. Rocca

Abstract: We report the demonstration of a gain-saturated 10.9 nm table-top soft x-ray laser operating at 1 Hz repetition rate. Lasing occurs by collisional electron impact excitation in the $4d^1S_0 \rightarrow 4p^1P_1$ transition of nickel-like Te in a line-focus plasma heated by a chirped pulse amplification Ti:sapphire laser. With an average power of 1 microwatt and pulse energy up to ~2 microjoules this laser extends the ability to conduct table-top laser experiments to a shorter wavelength.

6.3.1 Introduction

There is great interest in extending table-top soft x-ray lasers to shorter wavelengths for applications. Of particular interest is the development of gain-saturated lasers that can be fired repetitively, producing the average power required for many applications. Both capillary discharges and laser-created plasmas have been successfully used to demonstrate gain-saturated collisionaly excited table-top lasers that operate at wavelengths between 46.9 nm and 13.2 nm at repetition rates of several Hz [2-4, 17-23]. However, the steep wavelength scaling of the energy necessary to pump such lasers imposes a challenge to the demonstration of gain-saturated high repetition rate lasers at shorter wavelengths. As a result, the use of table-top soft x-ray lasers in applications has been limited to wavelengths above 13 nm. The shortest wavelength table-top laser used in

applications is a gain-saturated 13.2 nm nickel-like Cd laser that enabled the implementation of broad area microscopes with spatial resolution down to 38 nm [24].

Herein we report the demonstration of a gain-saturated table-top 10.9 nm in the $4d^1S_0 \rightarrow 4p^1P_1$ transition of nickel-like Te that operates at 1 Hz repetition rate. Lasing in nickel-like Te was first demonstrated using 520 J of laser pump energy to heat a collisionally pumped plasma [25]. More recently gain in this transition was obtained in a table-top setup using 1 J pulses of 8 ps duration impinging at a grazing angle of 23 degrees to heat a pre-created plasma [3]. However, the output laser intensity was weak and far from saturation, producing an insufficient photon flux for applications. Model computations conducted using a 1.5 dimension hydrodynamic/atomic physics code developed in house suggest that gain-saturated lasing in the λ=10.9 nm $4d^1S_0 \rightarrow 4p^1P_1$ transition of nickel-like Te can be generated by irradiation of a solid Te target with a sequence of pulses from a chirped pulse amplification laser with a total energy of less than 4 J. Figure 6.5 shows the simulated evolution of the plasma parameters and resulting gain coefficient for the 10.9 nm laser line. The plasma is assumed to be created by a sequence of two 210 ps duration pre-pulses with intensities of 4.8×10^{10} Wcm^{-2} and 1.8×10^{12} Wcm^{-2} separated by 5.6 ns, and to be subsequently transiently heated with a 5 ps FWHM duration pulse with an intensity of 9.8×10^{13} Wcm^{-2} impinging at 30 degrees grazing incidence. This pumping geometry, that is inherently traveling wave, takes advantage of the refraction of the pump beam in the electron density gradient of the pre-created plasma to efficiently deposit energy into a plasma density region with optimum conditions for amplification [2-4, 19-21, 23, 26].

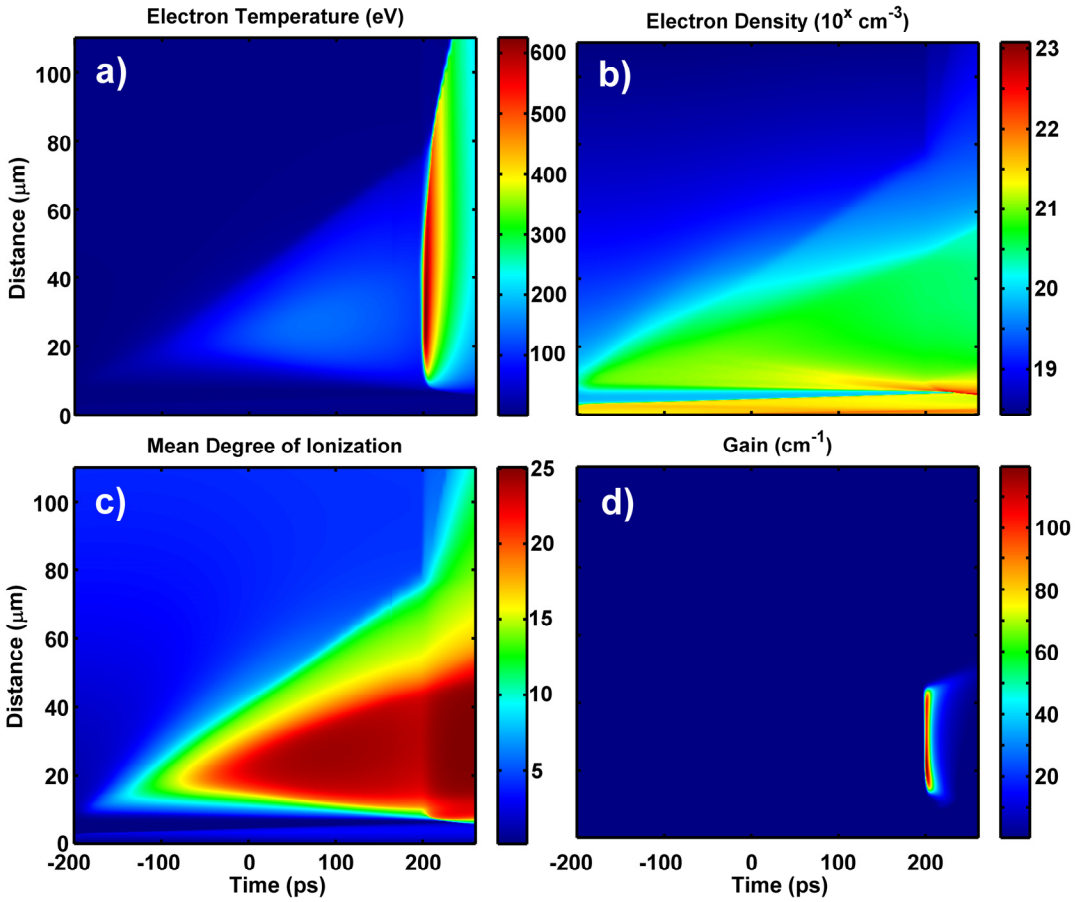

Figure 6.5 - Simulated evolution of a) electron temperature, b) electron density, c) mean degree of ionization, and d) λ = 10.9 nm gain coefficient for a Te plasma amplifier.

The first laser pulse is responsible for creating the ion density profile and the second laser pulse heats the plasma, ionizing 40% of the ions into the nickel-like state over a relatively broad region (Figure 6.5c). A dip in the degree of ionization develops between the outer region where the pre-pulse energy is absorbed and the target region dominated by pressure ionization. The short pulse energy is coupled by refraction into a region where the electron density is ~4×10^{20} cm^{-3}, and rapidly increases the electron temperature to ~ 600 eV (Figure 6.5a). This is computed to generate a transient inversion resulting in a peak gain of ~120 cm^{-1} with a FWHM duration of ~9 ps (Figure 6.5d). A 3-D post processor ray tracing code predicts a spatially integrated gain of 64 cm^{-1}. The

experiments described below used similar excitation conditions to demonstrate a $\lambda = 10.9$ nm table-top nickel-like Te laser operating at a repetition rate of 1 Hz with an average power of ~1 μW.

6.3.2 Experimental Setup

The experiment was conducted by rapidly heating a 5 mm wide solid Te slab target at the irradiation conditions described above using a chirped pulse amplification Ti:sapphire laser system. Three stages of amplification were used to amplify $\lambda = 800$nm pulses to energies up to 5.5 J before compression. After the third amplification stage the stretched pulses have a duration of 210 ps. A beam splitter placed after the final amplification stage was used to re-direct 40% of the energy into a pre-pulse arm used to create a plasma with relatively smooth density gradients. About 2% of the energy was split to create an initial plasma that was subsequently ionized to the nickel-like ionization stage by the second 210 ps duration pulse. The two pre-pulses, separated by 5.6 ns, were focused into a 30 μm x 5 mm FWHM line onto the target. The remaining 60% of the laser energy was compressed into a 5 ps FWHM pulse in a vacuum grating compressor constructed using dielectric diffraction gratings [27] and focused into an overlapping line of the same dimension. The plasma emission was filtered by a 0.3 μm thick Al foil and a 0.3 μm thick Zr foil both with parylene support and was directed onto a grazing incidence spectrometer consisting of a 1200 lines per millimeter variable line spaced grating and a back-illuminated CCD detector.

6.3.3 Experimental Results

Figure 6.6 shows the measured λ = 10.9 nm laser intensity as a function of time delay between the peaks of the main pre-pulse and the short pulse.

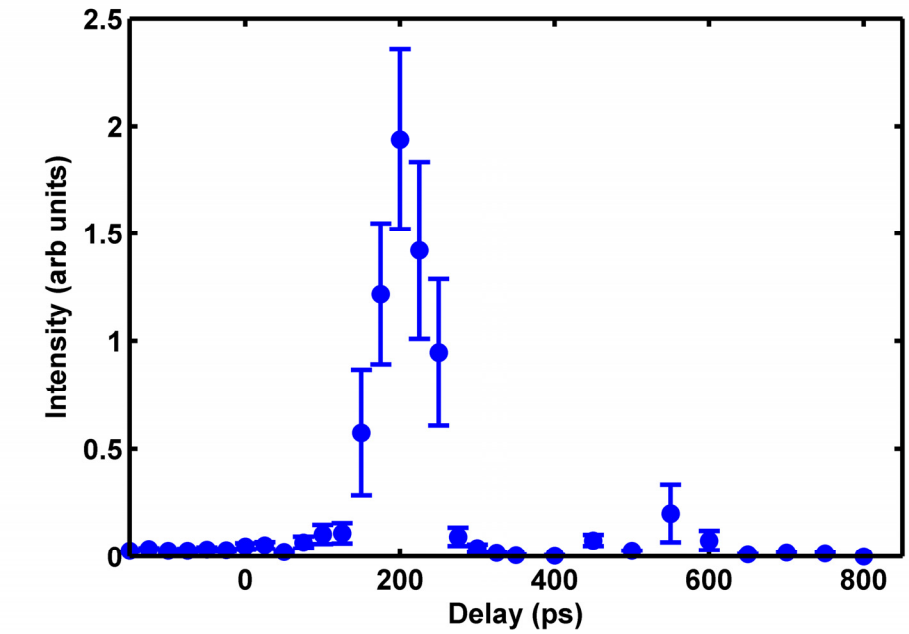

Figure 6.6 - Measured λ=10.9 nm laser intensity as a function of delay between the pre pulse and short pulse.

Strong soft x-ray lasing was observed to take place over a relatively narrow range of excitation delays centered at 200 ps. Lasing is observed to cease when the delay is increased to 400 ps. However, further increase of the delay results in weak lasing around 550 ps. This late laser pulse was predicted by the simulations. It occurs when Co-like ions recombine into Ni-like ions, indicating the plasma is slightly over-ionized at the time of peak laser gain.

Figure 6.7a shows a series of on-axis single-shot spectra and their corresponding vertical integrations for plasmas of different lengths between L = 1.8 and 5 mm. The total pump energy on target was fixed at 3.4 J. For a target length of 1.8 mm the 10.9 nm laser line is very weak and has an intensity similar to that of other plasma lines.

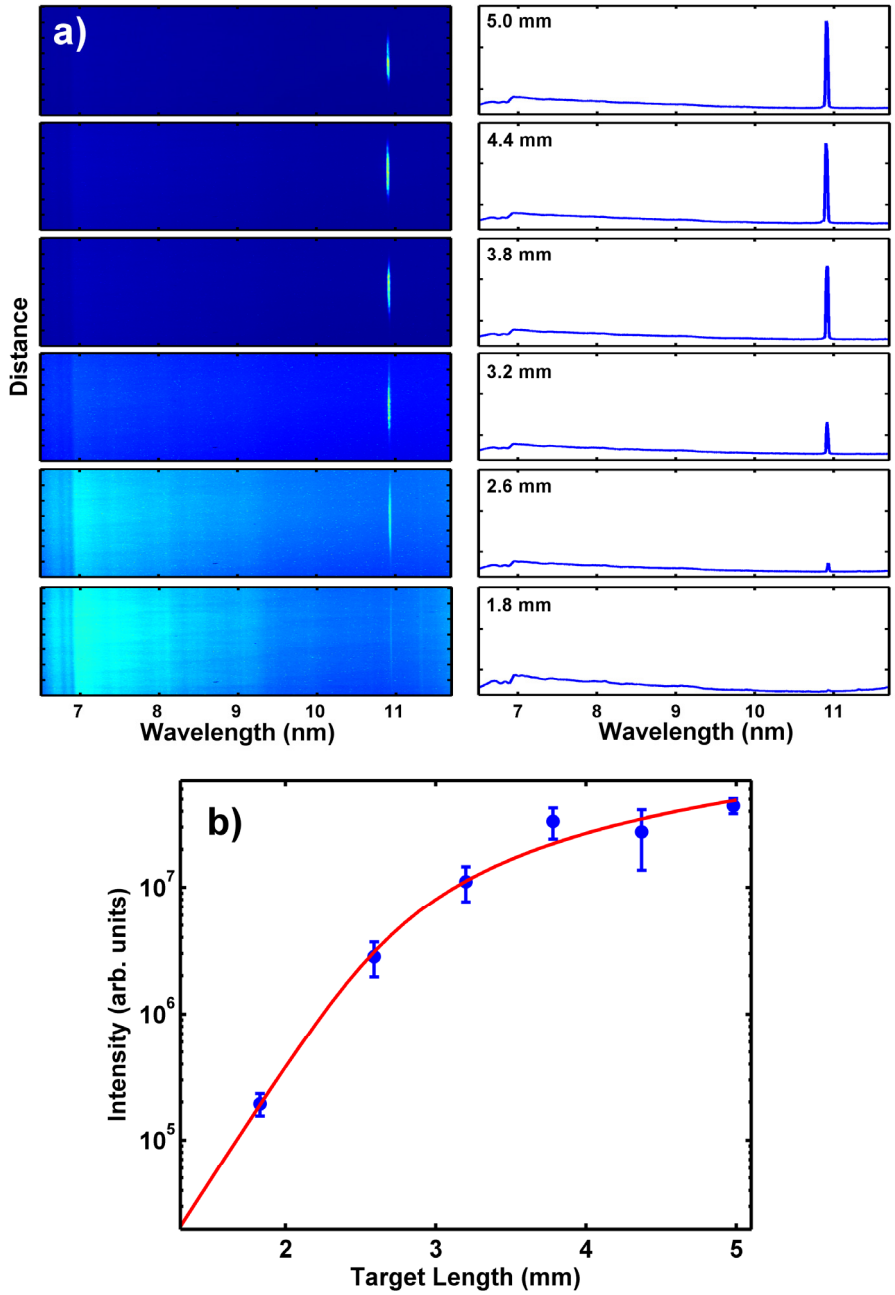

Figure 6.7 - a) On axis single-shot spectra from the Te plasma for increasing plasma column lengths from 1.8 to 5 mm. Strong lasing is observed at 10.9 nm. b) Measured laser line intensity as a function of plasma column length. Each data point is an average of eight laser shots and error bars correspond to one standard deviation.

The soft x-ray laser intensity rapidly grows with target length to dominate the entire spectra, eventually reaching saturation. From these spectra it was determined that for the 5 mm target the soft x-ray laser beam divergence in the direction parallel to the target is 8.5 ± 1 mrad. The measured soft x-ray laser intensity as a function of target length is shown in Figure 6.7b. The line is a fit of the data with an equation by Tallents et al. [28] that takes into account gain saturation. The fit shows a small signal gain of $g_0 = 45.3$ cm^{-1} and an integrated gain length product of 14.1 at 5 mm. At about 3 mm, the intensity starts to show signs of saturation.

Results of the variation of the soft x-ray laser pulse energy at a laser repetition rate of 1 Hz are shown in Figure 6.8.

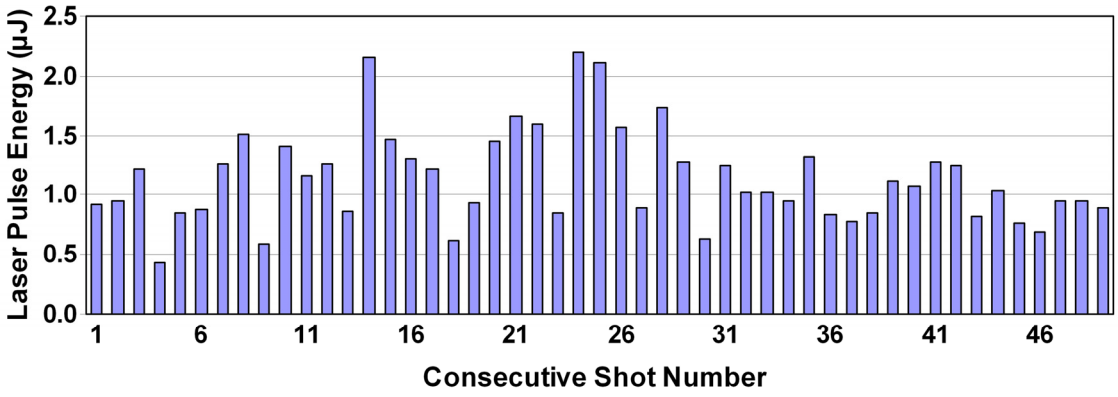

Figure 6.8 - Sequence of λ = 10.9 nm laser shots acquired at 1 Hz repetition rate achieving an average power of ~1 μW

This data was obtained pumping a 6 mm wide Te target with 4.2 J of total laser pump energy on target. The target was continually moved at a speed of 200 microns per second to renew the surface irradiated by each shot. The soft x-ray laser average power obtained was ~1 microwatt. The shot to shot energy variation is characterized by a standard deviation of 36%. This large variation can be explained by the brittle nature of the tellurium target, which often fractures locally near the edges when irradiated with the

high energy pulses used in this experiment, affecting the subsequent laser shot. In comparison, in a similar experiment conducted with a Ag target that does not fracture we measured a $\lambda = 13.9$ nm output pulse laser energy variation characterized by 8% standard deviation. An increase in the speed at which the Te target is moved should decrease the shot to shot fluctuation in soft x-ray laser pulse energy. The energy of the most intense laser pulses was estimated to be ~2 μJ from the CCD counts taking into account the attenuation of the filters, the grating efficiency, and the quantum efficiency of the detector. Assuming a laser pulse duration of 4 – 5 ps and a near-field laser spot of ~15 μm diameter, both resulting from the 3-D post processor ray trace simulation, the laser beam intensity is estimated to reach $\sim 2.5\times10^{11}$ Wcm^{-2}. This exceeds the $0.6\text{-}1.4\times10^{10}$ W/cm^2 computed saturation intensity of this line for the plasma conditions of the experiment.

6.3.4 Conclusions

In summary we have extended gain-saturated table-top soft x-ray lasers down to 10.9 nm by transient excitation of a nickel-like Te plasma. This is the shortest wavelength gain-saturated table-top laser reported to date. With an average power of ~ 1 μW and pulse energies of up to 2 μJ this laser will enable applications of table-top lasers at shorter wavelengths.

6.3.5 Acknowledgements

We thank Eric Gullikson for measuring the transmission of the aluminum and zirconium filters. This work was supported by the NSF ERC for Extreme Ultraviolet

Science and Technology NSF Award Number EEC-0310717 and by the Chemical Sciences, Geosciences and Biosciences Division, Office of Basic Energy Sciences, Office of Science, U.S. Department of Energy. M.B. acknowledges support from DOE CSGF Grant No. DE-FG02-97ER25308.

6.4 References

1. F. Brizuela, S. Carbajo, A. Sakdinawat, D. Alessi, D. H. Martz, Y. Wang, B. Luther, K. A. Goldberg, I. Mochi, D. T. Attwood, B. La Fontaine, J. J. Rocca, and C. S. Menoni, "Extreme ultraviolet laser-based table-top aerial image metrology of lithographic masks," Opt. Express **18**, 14467-14473 (2010).
2. J. J. Rocca, Y. Wang, M. A. Larotonda, B. M. Luther, M. Berrill, and D. Alessi, "Saturated 13.2 nm high repetition rate laser in Nickel-like Cd," Optics Letters **30**, 2581-2583 (2005).
3. Y. Wang, M. A. Larotonda, B. M. Luther, D. Alessi, M. Berrill, V. N. Shlyaptsev, and J. J. Rocca, "Demonstration of saturated high repetition rate tabletop soft x-ray lasers at wavelength down to 13.9 nm," Physical Review A **72**, 053807 (2005).
4. H. T. Kim, I. W. Choi, N. Hafz, J. H. Sung, T. J. Yu, K. H. Hong, T. M. Jeong, Y. C. Noh, D. K. Ko, K. A. Janulewicz, J. Tümmler, P. V. Nickles, W. Sandner, and J. Lee, "Demonstration of a saturated Ni-like Ag x-ray laser pumped by a single profiled laser pulse from a 10-Hz Ti:sapphire laser system," Physical Review A **77**, 023807 (2008).
5. D. Alessi, D. H. Martz, Y. Wang, M. Berrill, B. M. Luther, and J. J. Rocca, "Gain-saturated 10.9 nm tabletop laser operating at 1 Hz repetition rate," Optics Letters **35**, 414-416 (2010).
6. D. Zimmer, B. Zielbauer, M. Pittman, O. Guilbaud, J. Habib, S. Kazamias, D. Ros, V. Bagnoud, and T. Kuehl, "Optimization of a tabletop high-repetition-rate

soft x-ray laser pumped in double-pulse single-beam grazing incidence," Opt. Lett. **35**, 450-452 (2010).

7. A. Klisnick, O. Guilbaud, D. Ros, K. Cassou, S. Kazamias, G. Jamelot, J. C. Lagron, D. Joyeux, D. Phalippou, Y. Lechantre, M. Edwards, P. Mistry, and G. J. Tallents, "Experimental study of the temporal coherence and spectral profile of the 13.9nm transient X-ray laser," Journal of Quantitative Spectroscopy and Radiative Transfer **99**, 370-380 (2006).

8. Y. Liu, Y. Wang, M. A. Larotonda, B. M. Luther, J. J. Rocca, and D. T. Attwood, "Spatial coherence measurements of a 13.2 nm transient nickel-like cadmium soft x-ray laser pumped at grazing incidence," Optics Express **14**, 12872-12879 (2006).

9. R. F. Smith, J. Dunn, J. R. Hunter, J. Nilsen, S. Hubert, S. Jacquemot, C. Remond, R. Marmoret, M. Fajardo, P. Zeitoun, L. Vanbostal, C. L. S. Lewis, M. F. Ravet, and F. Delmotte, "Longitudinal coherence measurements of a transient collisional x-ray laser," Opt. Lett. **28**, 2261-2263 (2003).

10. M. Tanaka, M. Nishikino, T. Kawachi, N. Hasegawa, M. Kado, M. Kishimoto, K. Nagashima, and Y. Kato, "X-ray laser beam with diffraction-limited divergence generated with two gain media," Opt. Lett. **28**, 1680-1682 (2003).

11. P. Zeitoun, G. Faivre, S. Sebban, T. Mocek, A. Hallou, M. Fajardo, D. Aubert, P. Balcou, F. Burgy, D. Douillet, S. Kazamias, G. de Lacheze-Murel, T. Lefrou, S. le Pape, P. Mercere, H. Merdji, A. S. Morlens, J. P. Rousseau, and C. Valentin, "A high-intensity highly coherent soft X-ray femtosecond laser seeded by a high harmonic beam," Nature **431**, 426-429 (2004).

12. T. Mocek, S. Sebban, G. Maynard, P. Zeitoun, G. Faivre, A. Hallou, M. Fajardo, S. Kazamias, B. Cros, D. Aubert, L. de, egrave, G. ze-Murel, J. P. Rousseau, and J. Dubau, "Absolute Time-Resolved X-Ray Laser Gain Measurement," Physical Review Letters **95**, 173902 (2005).

13. Y. Wang, E. Granados, M. A. Larotonda, M. Berrill, B. M. Luther, D. Patel, C. S. Menoni, and J. J. Rocca, "High-Brightness Injection-Seeded Soft-X-Ray-Laser Amplifier Using a Solid Target," Physical Review Letters **97**, 123901 (2006).

14. F. Pedaci, Y. Wang, M. Berrill, B. Luther, E. Granados, and J. J. Rocca, "Highly coherent injection-seeded 13.2 nm tabletop soft x-ray laser," Opt. Lett. **33**, 491-493 (2008).

15. Y. Wang, E. Granados, F. Pedaci, D. Alessi, B. Luther, M. Berrill, and J. J. Rocca, "Phase-coherent, injection-seeded, table-top soft-X-ray lasers at 18.9 nm and 13.9 nm," Nature Photonics **2**, 94-98 (2008).

16. Y. Wang, M. Berrill, F. Pedaci, M. M. Shakya, S. Gilbertson, Z. Chang, E. Granados, B. M. Luther, M. A. Larotonda, and J. J. Rocca, "Measurement of 1-ps soft-x-ray laser pulses from an injection-seeded plasma amplifier," Physical Review A **79**, 023810 (2009).

17. B. R. Benware, C. D. Macchietto, C. H. Moreno, and J. J. Rocca, "Demonstration of a High Average Power Tabletop Soft X-Ray Laser," Physical Review Letters **81**, 5804 (1998).

18. S. Sebban, R. Haroutunian, P. Balcou, G. Grillon, A. Rousse, S. Kazamias, T. Marin, J. P. Rousseau, L. Notebaert, M. Pittman, J. P. Chambaret, A. Antonetti, D. Hulin, D. Ros, A. Klisnick, A. Carillon, Jaegl, eacute, P., G. Jamelot, and J. F.

Wyart, "Saturated Amplification of a Collisionally Pumped Optical-Field-Ionization Soft X-Ray Laser at 41.8 nm," Physical Review Letters **86**, 3004 (2001).

19. D. Alessi, B. Luther, Y. Wang, M. Larotonda, M. Berrill, and J. Rocca, "High repetition rate operation of saturated tabletop soft x-ray lasers in transitions of neon-like ions near 30 nm," Opt. Express **13**, 2093-2098 (2005).

20. B. M. Luther, Y. Wang, M. A. Larotonda, D. Alessi, M. Berrill, M. C. Marconi, J. J. Rocca, and V. N. Shlyaptsev, "Saturated high-repetition-rate 18.9-nm tabletop laser in nickellike molybdenum," Optics Letters **30**, 165-167 (2005).

21. K. Cassou, S. Kazamias, D. Ros, F. Plé, G. Jamelot, A. Klisnick, O. Lundh, F. Lindau, A. Persson, C.-G. Wahlström, S. d. Rossi, D. Joyeux, B. Zielbauer, D. Ursescu, and T. Kühl, "Optimization toward a high-average-brightness soft-x-ray laser pumped at grazing incidence," Optics Letters **32**(2007).

22. M. C. Chou, P. H. Lin, C. A. Lin, J. Y. Lin, J. Wang, and S. Y. Chen, "Dramatic Enhancement of Optical-Field-Ionization Collisional-Excitation X-Ray Lasing by an Optically Preformed Plasma Waveguide," Physical Review Letters **99**, 063904 (2007).

23. S. Kazamias, K. Cassou, D. Ros, Pl, eacute, F., G. Jamelot, A. Klisnick, O. Lundh, F. Lindau, A. Persson, Wahlstr, ouml, C. G. m, S. de Rossi, D. Joyeux, B. Zielbauer, D. Ursescu, uuml, and T. hl, "Characterization of a transient collisional Ni-like molybdenum soft-x-ray laser pumped in grazing incidence," Physical Review A **77**, 033812 (2008).

24. G. Vaschenko, C. Brewer, F. Brizuela, Y. Wang, M. A. Larotonda, B. M. Luther, M. C. Marconi, J. J. Rocca, C. S. Menoni, E. H. Anderson, W. Chao, B. D. Harteneck, J. A. Liddle, Y. Liu, and D. T. Attwood, "Sub-38 nm resolution tabletop microscopy with 13 nm wavelength laser light," Opt. Lett. **31**, 1214-1216 (2006).

25. H. Daido, S. Ninomiya, T. Imani, R. Kodama, M. Takagi, Y. Kato, K. Murai, J. Zhang, Y. You, and Y. Gu, "Nickellike soft-x-ray lasing at the wavelengths between 14 and 7.9 nm," Optics Letters **21**, 958-960 (1996).

26. R. Keenan, J. Dunn, P. K. Patel, D. F. Price, R. F. Smith, and V. N. Shlyaptsev, "High-Repetition-Rate Grazing-Incidence Pumped X-Ray Laser Operating at 18.9 nm," Physical Review Letters **94**, 103901 (2005).

27. D. H. Martz, H. T. Nguyen, D. Patel, J. A. Britten, D. Alessi, E. Krous, Y. Wang, M. A. Larotonda, J. George, B. Knollenberg, B. M. Luther, J. J. Rocca, and C. S. Menoni, "Large area high efficiency broad bandwidth 800 nm dielectric gratings for high energy laser pulse compression," Optics Express **17**, 23809-23816 (2009).

28. G. J. Tallents, Y. Abou-Ali, M. Edwards, R. E. King, G. J. Pert, S. J. Pestehe, F. Strati, R. Keenan, C. L. S. Lewis, S. Topping, O. Guilbaud, A. Klisnick, D. Ros, R. Clarke, D. Neely, and M. Notley, "Saturated and Short Pulse Duration X-Ray Lasers," in *X-Ray Lasers 2002: 8th International Conference on X-ray Lasers*, (AIP Conference Proceedings 2002), 291.

CHAPTER 7

SUMMARY

Extreme Ultraviolet (EUV) lasers are evolving into intense sources of coherent short wavelength light for applications such as nano-scale imaging, dense plasma diagnostics, studies of surfaces and materials, studies of the chemistry of catalytic processes and unique metrology and processing tools for industry. The development of the driver laser technologies enables the advancement of EUV lasers into practical sources for such applications.

The work in this dissertation resulted in the development of a high energy Ti:Sapphire laser system designed to drive compact EUV lasers that produced high average power at short wavelengths for applications. The design, construction and implementation of a Nd:Glass zig-zag slab amplifier was shown along with results characterizing successful operation. The amplifiers produce 18 J 1.053 μm laser pulses of 15 ns duration. Frequency doubling of two arms produced ~ 20 J of 527 nm radiation which was directed into a 60 mm Ti:sapphire crystal. The amplification of 800 nm laser pulses up to 7.5 J at 2.5 Hz repetition rate was achieved. Efficient picosecond pulse compression with 80% efficiency was achieved using new multi-layer dielectric diffraction gratings that were developed as part of this work. Further work is needed to increase the damage threshold for operation with pulse widths below 1 picosecond.

The Ti:Sapphire laser system was used to pump several table-top EUV lasers. Increased average power operation of a 13.9 nm Ni-like Ag laser generating 20 μW was demonstrated. Injection seeding of the 13.9 nm EUV amplifier was achieved and a comparison to ASE operation was shown indicating improved beam divergence and a near Gaussian far-field profile. Saturated table-top operation of a 10.9 nm Ni-like Te EUV laser is shown extending saturated table-top operation to shorter wavelengths.

In summary, advancements were made for the table-top generation of EUV lasers. A high energy Ti:Sapphire system enabled by a Nd:Glass zig-zag slab pump laser and all new efficient MLD diffraction gratings for 800 nm pulses was demonstrated. The Ti:Sapphire laser was used to improve table-top EUV laser operation producing higher average powers and shorter wavelengths. Future work will utilize the successful table-top system for further improvement of EUV laser generation and demonstration of new applications.

Appendix A

The following type of analys is used to calculate pressure drops and flow is common place in fluid mechanics and fluid engineering. Although I used reference A.1 as a guide, there are many books that cover these types of solutions.

Cooling of Slab

Flow Rate

An assumed flow rate based on the ability to remove 1250 W of power while keeping a temperature difference of 0.1 °C across the 14 cm dimension of the slab.

$V := 3000$ gm/s or mL/s or cm^3/s Mass/Volumetric flow rate

$\frac{V}{1000} = 3$ L/s

$V \cdot 0.015 = 45$ Gal/min

Reynolds Number

For energy extraction to be efficient, a transient to turbulant water flow is needed to maximize heat transfer. To determine this, the Reynolds number must be known.

$\mu := 0.00764$ gm/cm*s μ is the dynamic (absolute) viscosty of water

$w := 0.25$ cm width of channel

$l_p := 36$ cm length of channel

$p_w := 2 \cdot (l_p + w)$ p_w is the wetted perimeter of the rectangular cross-section

The Reynolds number for a rectangular cross-section using water as a coolent is:

$$Re(m_{flow}) := 4 \cdot \frac{\frac{m_{flow}}{2}}{\mu \cdot p_w}$$ <--m_{flow}/2 is used because there are two sides of the slab

$Re(3000) = 10832.28$

Change in pressure across slab channels

For a turbulant flow, Reynolds number > 2* 10^4

$f := 0.316 \cdot Re(3000)^{-0.25}$ friction factor

$f = 0.031$

$L := 14$ cm height of channel

$A_c := l_p \cdot w$ cross-sectional area of channel

$D := 4 \cdot \frac{A_c}{p_w}$ hydraulic diameter

$u := 4 \cdot \frac{\frac{V}{2}}{p_w \cdot D}$ fluid flow velocity in channel

$u = 166.667$ cm/s

$\rho := 1$ gm/cm^3 density of water

$\Delta p := f \cdot \left(\frac{L}{D}\right) \cdot \frac{\rho \cdot u^2}{20}$ change in pressure across channel

$\Delta p = 1212.937$ Pa

$PSI := 6894.75729$ Pa

$PD_{Slab} := \frac{\Delta p}{PSI}$ conversion to PSI

$PD_{Slab} = 0.176$ psi

Estimation of change in pressure due to entrance expansion, 90 degree turn and exit loss inside the amplifier

$PD_{ex}(K, v) := K \cdot \frac{v^2}{20PSI}$ pressure drop for a generic smooth bend, coefficient (K) selection based on shape of channel

$PD_{ex}(1.1, u) = 0.222$ psi 90 degree sharp turn at entrance

$PD_{ex}(1.4, u) = 0.282$ psi entrance expansion loss
Figure A.1

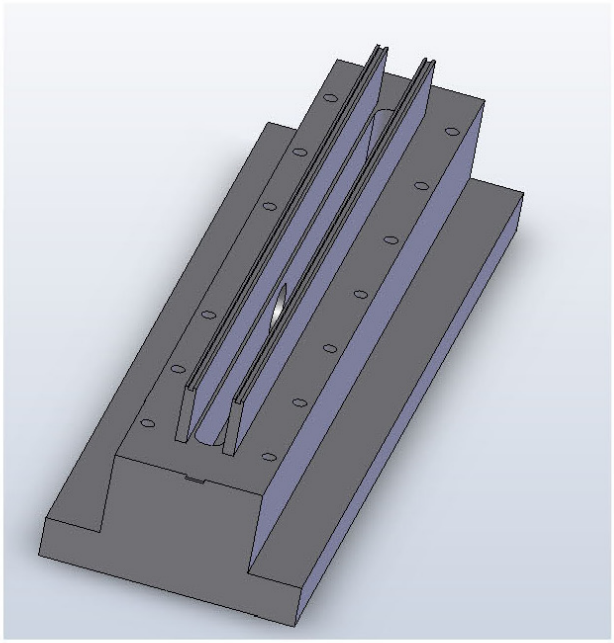

Figure A.1 - Entrance to slab channels with expansion loss

$PD_{ex}(0.5, u) = 0.101$ psi exit loss
Figure A.2

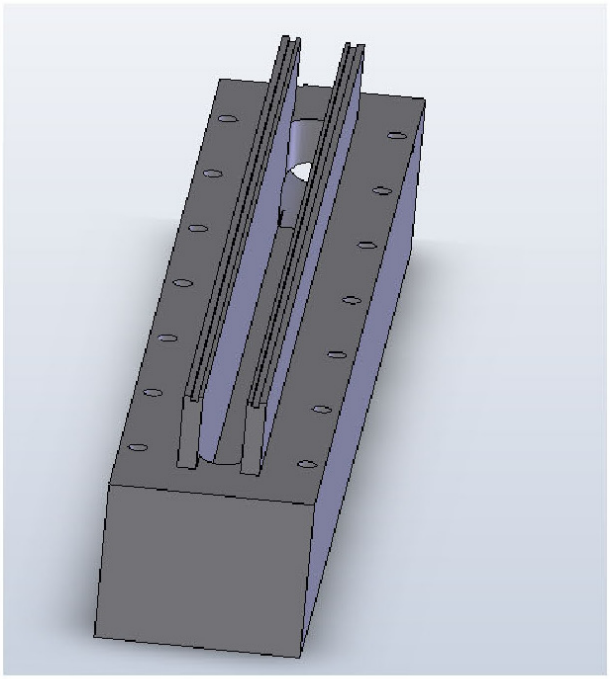

Figure A.2 - Exit from slab channels with loss

$u_{splitter} := \frac{V}{\pi \cdot 1.032^2}$ fluid flow velocity through splitter at exit

$u_{splitter} = 896.627$ cm/s

$PD_{ex}(0.19, u_{splitter}) = 1.108$ psi pressure drop across splitter at exit
Figure A.3

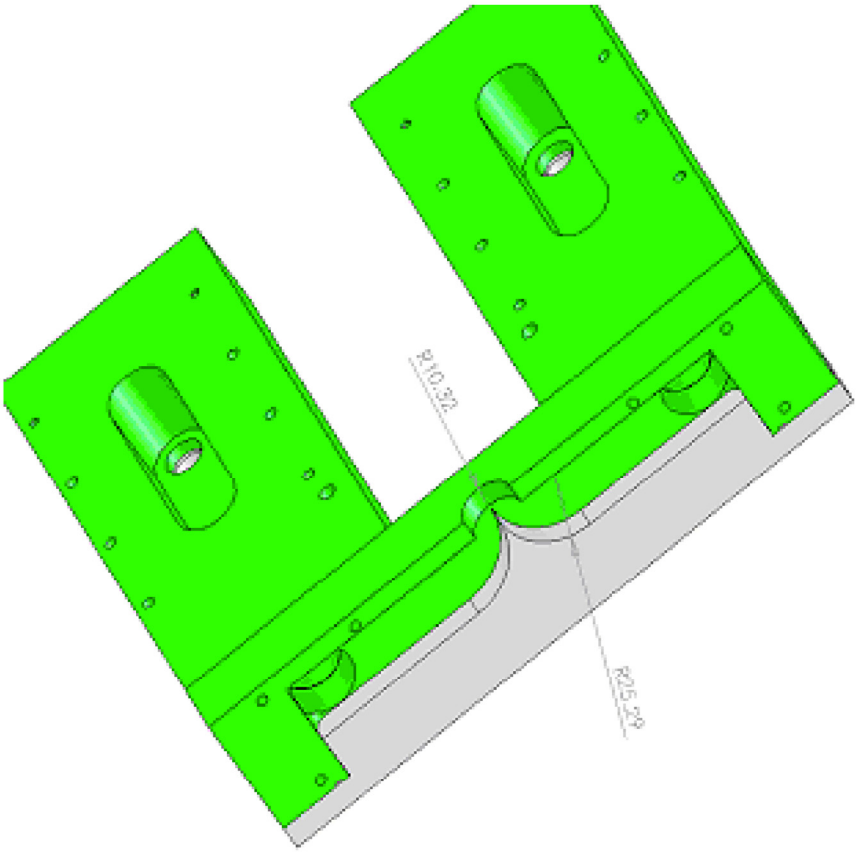

Figure A.3 - Smooth bend splitter at exit of slab

$PD_{total\_slab} := PD_{ex}(1.4, u) + PD_{Slab} + PD_{ex}(1.1, u) + PD_{ex}(0.5, u) + PD_{ex}(0.19, u_{splitter})$

$PD_{total\_slab} = 1.888$ psi

Lamp Cooling (In series after the Slab)

Reynolds Number

$r_{in} := \frac{2.1}{2}$ cm — radius of lamp

$r_{out} := \frac{2.9}{2}$ cm — radius of tube

$p_{tube} := 2 \cdot \pi \left(r_{in} + r_{out} \right)$ — the wetted perimeter of the tube with the lamp inside

$Re\left(m_{flow}\right) := 4 \cdot \frac{\frac{m_{flow}}{4}}{\mu \cdot p_{tube}}$ — we use $m_{flow}/4$ because there are four lamps in parallel

$Re(V) = 24998.159$

Change in pressure across lamp flow tubes

For a Reynolds number > 2* 10^4 in a turbulant flow:

$f := 0.316 \cdot Re(V)^{-0.25}$ — friction factor

$f = 0.025$

$L_{tube} := 41$ cm — length of tube

$A_{tube} := \pi \left(r_{out}^{\ 2} - r_{in}^{\ 2} \right)$ — cross-sectional area of lamp and flow tube

$D_{tube} := 4 \cdot \frac{A_{tube}}{p_{tube}}$ — hydraulic diameter

$u_{tube} := 4 \cdot \frac{\frac{V}{4}}{p_{tube} \cdot D_{tube}}$ — fluid flow velocity

$u_{tube} = 238.732$ cm/s

$\Delta p_{tube} := f \cdot \left(\frac{L_{tube}}{D_{tube}} \right) \cdot \frac{\rho \cdot u_{tube}^{\ 2}}{20}$ — change in pressure across flow tube

$\Delta p_{tube} = 3670.259$ Pa

$$PD_{Lamps} := \frac{\Delta p_{tube}}{1000 \cdot 6.89475729}$$ conversion to PSI

$PD_{Lamps} = 0.532$ psi

Estimation of change in pressure due to entrance expansion and smooth bends at the entrances and exits

$$PD_{ex}(K, v) := K \cdot \frac{v^2}{20PSI}$$ pressure drop for a generic smooth bend, coefficient (K) selection based on shape of channel

$$u_{sb} := \frac{\frac{V}{2}}{\pi \cdot 1.032^2}$$ fluid flow velocity through smooth bends at entrance and exit

$u_{sb} = 448.314$ cm/s

$PD_{ex}(0.19, u_{sb}) = 0.277$ psi smooth bend drop at entrance and exit Figure A.4

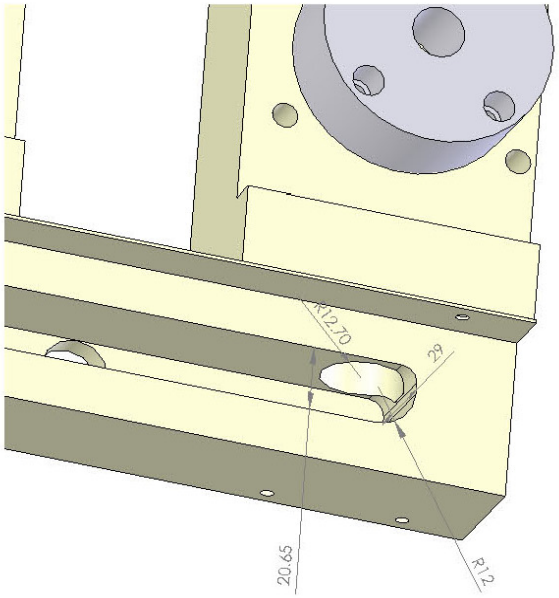

Figure A.4 - Smooth bend at the exit of the lamp flow tubes

$PD_{ex}(1.4, u_{tube}) = 0.579$ psi entrance expansion drop

$PD_{total\_lamp} := PD_{ex}(0.19, u_{sb}) + PD_{ex}(1.4, u_{tube}) + PD_{Lamps} + PD_{ex}(0.19, u_{sb})$

$PD_{total\_lamp} = 1.665$ psi

Change in pressure due to external system

Change in pressure through 1 inch ID hose

$D_{eng} := 1$ in. inner diameter of hose

$D_{tubes} := D_{eng} \cdot 2.54$ conversion to cm

$D_{tubes} = 2.54$ cm

$A_{tubes} := \pi \left(\frac{D_{tubes}}{2} \right)^2$ cross-sectional area of hose

$A_{tubes} = 5.067$ cm^2

$u_{tubes} := \frac{V}{A_{tubes}}$ fluid flow velocity through 1 in. inner diameter tubes

$u_{tubes} = 592.058$ cm/s

$Re_{tubes} := \frac{\rho \cdot u_{tubes} \cdot D_{tubes}}{\mu}$ Reynolds number for hose

$Re_{tubes} = 196835.894$

For a Reynolds number > $2^* 10^4$ in a turbulant flow:

$f := 0.184 \cdot Re_{tubes}^{-0.25}$ friction factor

$f = 0.009$

$$\Delta p_{tubes}(L_{tubes}) := 2f \cdot \left(\frac{L_{tubes}}{D_{tubes}}\right) \cdot \frac{\rho \cdot u_{tubes}^{2}}{20}$$

pressure drop across hose dependent on length

(Multiplying "f" by 2 to be safe)

$$PD_{tubes}(x) := \frac{\Delta p_{tubes}(x)}{PSI}$$

conversion to PSI/m

$PD_{tubes}(100) = 1.749$ psi/m

Change in pressure through the turns

For a r/d ratio of 4 (Optimum) for a 90^0 smooth bend:

$K_b := 0.16$ loss coefficient

$$\Delta p_{turns} := K_b \cdot \frac{u_{tubes}^{2}}{20}$$

change in pressure across turn

$$PD_{turns} := \frac{\Delta p_{turns}}{PSI}$$

conversion to PSI

$PD_{turns} = 0.407$ psi

$PD_{heat\_exchanger} := 4$ psi from manufacturer at 3 l/s flow rate

$PD_{external\_system} := PD_{tubes}(500) + PD_{heat\_exchanger} + 4 \cdot PD_{turns}$

$PD_{external\_system} = 14.369$ psi

Total Pressure Drop Through System

$PD_{total} := PD_{total\_slab} + PD_{total\_lamp} + PD_{external\_system}$

$PD_{total} = 17.922$ psi

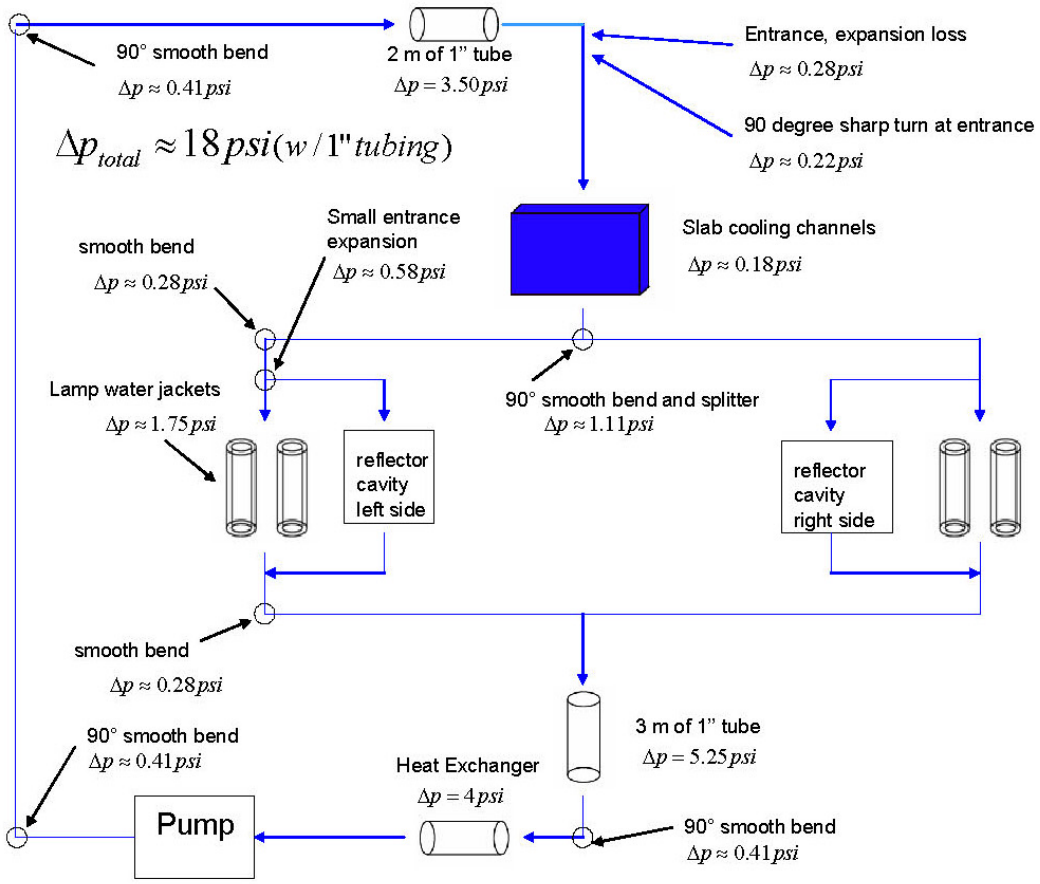

Figure A.5 - Schematic of water flow through the amplifier and cooling system. All significant pressure drops are indicated.

References

[A.1] David Pnueli, *Fluid Mechanics* (Cambridge, New York, Cambridge University Press, 1992)